JOINT INSTITUTE FOR AERONAUTICS AND ACOUSTICS

National Aeronautics and Space Administration

Ames Research Center

JIAA TR - 87

Stanford University

AN EXPERIMENTAL STUDY OF AN ADAPTIVE-WALL WIND TUNNEL

BY

Zeki Celik and Leonard Roberts

Stanford University
Department of Aeronautics and Astronautics
Stanford, CA 94305

AUGUST 1988

Abstract

A series of adaptive-wall ventilated wind tunnel experiments was carried out to demonstrate the feasibility of using the side-wall pressure distribution as the flow variable for the assessment of compatibility with free-air conditions. Iterative and one-step convergence methods were applied using the streamwise velocity component, the side-wall pressure distribution and the normal velocity component in order to investigate their relative merits. The advantage of using the side-wall pressure as the flow variable is to reduce the data-taking time which is one of the major contributors to the total testing time. In ventilated adaptive-wall wind tunnel testing, side-wall pressure measurements require simple instrumentation as opposed to the Laser Doppler Velocimetry used to measure the velocity components.

In ventilated adaptive-wall tunnel testing, influence coefficients are required to determine the pressure corrections in the plenum compartments. An influence coefficient is defined as the relation between the change in the flow variable at a point at the control level and the change in the pressure in an active plenum compartment. In the present study, experiments were carried out to evaluate the influence coefficients from side-wall pressure distributions, and from streamwise and normal velocity distributions at two control levels. Velocity measurements were made using a two-component Laser Doppler Velocimeter (LDV) system.

Side-wall, top- and bottom-wall pressure distributions, velocity components and plenum pressures were measured systematically to evaluate the effects of Mach number; the presence of a nonlifting model; location of the plenum compartments and the control points; and suction and blowing on the influence coefficients. Linearity and superposition of the influence coefficients was investigated. Free stream

Mach number characteristics of the test section were explored. Influence coefficient matrices were formed for both suction and blowing.

A one-step convergence scheme was developed and applied theoretically and experimentally by using the influence coefficient matrices. The one-step scheme reduces the testing time by eliminating the intermediate experimental iterations. The success of the one-step scheme depends on the accuracy of the influence coefficients. It was shown that the number of iterations could be reduced to a minimum with the application of the one-step scheme. Results showed that the same unconfined conditions obtained with the streamwise and normal velocity components, could be achieved when the resultant velocity distribution from side-wall pressure measurements was used as the flow variable.

The present study was conducted in the NASA Ames 23 cm x 11 cm indraft wind tunnel with a ventilated adaptive-wall test section. Experiments were carried out at velocities from $M = 0.5$ to $M = 0.75$ and at angles of attack from $\alpha = 0.°$ to $\alpha = 4.°$.

ACKNOWLEDGEMENTS

This research was supported by NASA Grant NCC 2-77.

Contents

List of Tables

List of Figures

Nomenclature

a_0	speed of sound at standard atmospheric conditions
c	airfoil chord
c_0	calibration constant
$C_{i,j}$	an element of the influence coefficient matrix
C_p	pressure coefficient
f_D	Doppler frequency
f_{mix}	mixing frequency
f_s	signal frequency
f_{shift}	shift frequency
M	Mach number
N	number of control points
p	static pressure
P_t	total pressure
R	gas constant
Re	Reynolds Number
t_s	period of the signal
T	temperature in Kelvins
$u_{c,i}$	calculated disturbance velocity component
$u_{m,i}$	measured disturbance velocity component
u'	streamwise disturbance velocity component
u'_r	$= U_r - U_{ref}$
U	streamwise velocity component
U_r	resultant velocity

U_{ref} longitudinal freestream velocity

v normal disturbance velocity component

V velocity

x airfoil longitudinal axis, origin at $X/c = -0.25$

X longitudinal coordinate

Y normal coordinate

α angle of attack, degrees

δ fringe spacing

θ angle of intersecting beams

ν kinematic viscosity

ΔP change in the plenum pressure

ΔV change in the disturbance velocity

Subscripts

c calculated

i at i^{th} control point

j in j^{th} plenum compartment

k number of plenum compartments

l number of control points

m measured

n when suction and/or blowing applied

o initial, all valves closed

p predicted

t total

∞ freestream values

Chapter 1

Introduction

The testing of aerodynamic models in wind tunnels has been the primary means of obtaining information for the design of aircraft for almost a hundred years, beginning with the early attempts by the Wright Brothers in the 1890's. Despite this long and largely successful history, it has always been recognized that wind tunnel data must be analyzed and corrected before it can be applied to flight conditions. These corrections must take into account the influence of the wind tunnel walls and the model support devices which are not present in flight, in addition to the changes in viscous effects that result from the change in scale from tunnel conditions to flight conditions (the so-called Reynolds number effects).

In recent years, with the introduction of the fast computer, it is possible to determine the flow around simple configurations from purely theoretical considerations, particularly when the influence of Reynolds number is small. However, in most practical applications, aerodynamic design continues to depend on both computer-derived and wind-tunnel-derived information. For this reason, it is essential that accurate means of correcting for wall and model support effects be incorporated into wind tunnel test procedures. This is particularly true in the transonic regime where wall interference becomes more significant and the influence of viscous effects, through such phenomena as shock-boundary layer interaction, become more difficult to describe in a purely theoretical model.

Over the years, rational schemes have been developed and used to correct the wind tunnel data[1-7]. However these schemes are generally approximations, based on potential flow methods, external flow field estimations, wind tunnel idealization, etc. Although they represent valid mathematical solutions, they may not describe the flow in the wind tunnel in all its complexity. Inaccuracies in wall interference prediction arise from the following facts: i) the governing equations are nonlinear in transonic flow, ii) wall boundary conditions in the ventilated wind tunnels are complex and difficult to predict, iii) it may not be possible to model the wind tunnel geometry properly, and iv) the flow may deviate from the two-dimensional flow because of the boundary layer on the tunnel side-walls.

Since accurate corrections are almost impossible in the transonic regime, the wind tunnel flow should approach, as nearly as possible, the free flight conditions around the model. Conventional slotted and perforated tunnels are intended to achieve this goal, but unfortunately they are often inadequate, especially when models with high blockage ratios have to be tested.

1.1 The Adaptive-Wall Concept

The adaptive-wall wind tunnel concept is an alternative approach to eliminating the wall interference or to reducing it significantly by controlling the flow near the walls. The principle of the adaptive-wall technique can be explained easily by referring to the flow field around a model in the test section of a flexible-wall wind tunnel as illustrated in Figure 1.1a. If the streamlines above and below the model have their free air shape, unconfined flow conditions would exist in the test section. These free air conditions can be simulated in a wind tunnel if the flow conditions along the inner side of the wall are the same as those along the outer side for the fictitious external flow field. In principle, this argument is also valid for the ventilated-wall tunnels (Figure 1.1b).

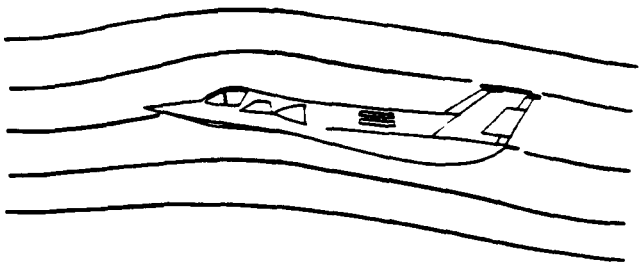

Model in free flight

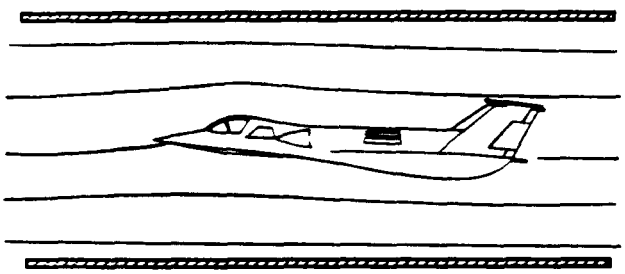

conventional

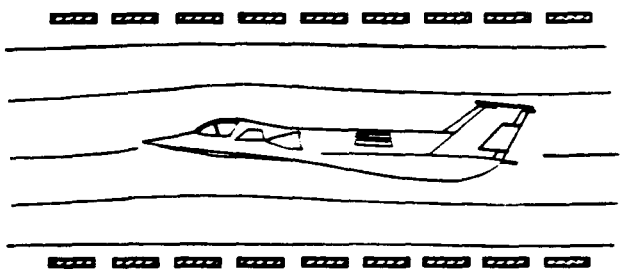

conventional

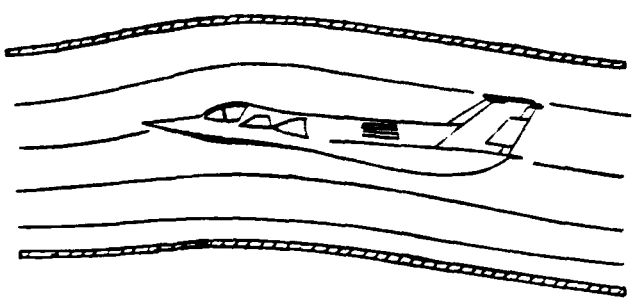

adapted

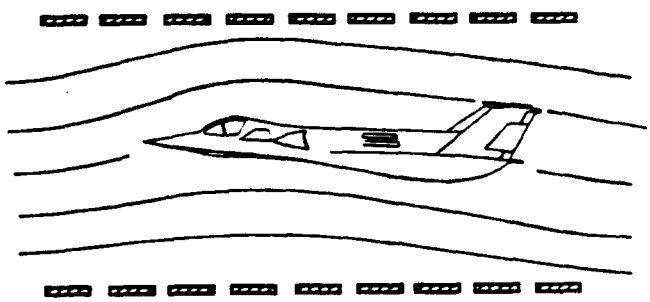

adapted

a) Model in flexible-wall wind tunnel

b) Model in ventilated-wall wind tunnel

Figure 1.1: A schematic to explain the principle of adaptive-wall concept in flexible and ventilated wall wind tunnels.

The adaptive-wall wind tunnel provides the means of modifying the boundary conditions at the tunnel walls so that the flow can conform to that which would exist in free flight. This requires that the flow within the tunnel be made consistent at the boundary with a fictitious (computed) flow outside the tunnel that satisfies uniform flow conditions at infinity. The tunnel wall conditions must be adapted until this consistency is achieved, hence the term 'adaptive-wall wind tunnel'.

In practice, the concept of the adaptive-wall wind tunnel requires an iterative process in which two flow variables are measured independently in the presence of an arbitrary model and flow configuration. At an interface, one flow variable is used to evaluate the functional relationships for the unconfined flow. The unconfined flow solution is compared with the second flow variable measured at the same interface. Once the effect of the wall interference is determined, local wall properties are adjusted to achieve the interference-free flow. New flow variables are then measured and checked with the unconfined flow solution. If they are not consistent with interference-free flow conditions, the procedure is repeated until the results agree within the range of the experimental error.

In general, an adaptive-wall wind tunnel scheme involves three major components: instrumentation for the measurement of flow variables, computing hardware and software, and a method of modifying the wall boundary conditions. In ventilated wind tunnels, adaptive-wall control can be produced by changing the local plenum pressure[8,9] or using walls with adjustable porosity[10]. Wall boundary conditions can be adjusted by changing the local wall contour in flexible-wall wind tunnels[11].

1.2 Survey of Previous Work

Since the introduction of the modern adaptive-wall concept, extensive research and development has been done on two-dimensional adaptive-wall wind tunnels and research on three-dimensional wind tunnels is now in progress. A comprehensive bibliography of the studies on adaptive-wall wind tunnels is given in Reference 12.

The first studies of adapting wind tunnel walls to reduce wind tunnel interference

were conducted in the 1940's[13]. Two-dimensional flexible-wall wind tunnels were used to solve the blockage problem at high speeds, the shape of the flexible walls being determined from the free air solution past the model. This method was limited to flows which could be solved analytically.

The modern adaptive-wall wind tunnel concept was introduced by Ferri and Baronti[14] and Sears[15] independently to solve the wall interference problem especially in transonic wind tunnels. Ferri and Baronti suggested a method to assess wall interference from two independently measured flow variables at the tunnel walls. They chose the static pressure and the flow angle as the flow variables. These parameters were used in performing free air calculations and the results were compared with the measured quantities. In their work, Ferri and Baronti discussed the validity of using linearized theory for transonic wall interference assessment and demonstrated its applicability by numerical computations.

In an independent work, Sears developed the concept of a control level removed from the walls[15]. In his method, two flow variables are measured at a control level. One of them is used as a boundary condition to compute the other flow variable in unconfined flow external to the chosen control level. The predicted value of the flow variable is compared with the measured value to assess the wall interference. An iterative procedure is applied to change the wall conditions until the measured and computed values agree, implying interference-free flow in the test section. In this method, the difficulty of modeling or calibrating the flow near the walls is avoided.

Application of a numerical simulation of the flow within the wind tunnel test section by Erickson and Nenni[16,17], showed that the adaptive-wall wind tunnel scheme can be iterated successfully and converges to unconfined flow conditions. In this simulation, it was assumed that the flow was incompressible and sufficient wall control was available to modify the tunnel wall boundary conditions.

In the experimental studies performed to show the applicability of Sears' method to two- and three-dimensional flows[8,18], several practical problems related to instrumentation, the nature of the wall modification, and convergence of the control logic were discussed in detail. Comparisons with data obtained in larger tunnels showed that active wall control reproduced the correct shock wave location and

eliminated or minimized the interference effects on aerodynamic characteristics.

In a theoretical study for the convergence of the adaptive-wall concept, Sears[19] pointed out the major factors influencing the accuracy of adaptive-wall control, such as the finite length of the test section and the finite number of control points and plenum compartments. Because of these factors, the interference-free relationships can be established only approximately. Sears showed that the iterative process can still converge to an imperfect approximation to the unconfined flow. However, interference can be substantially reduced as compared to that in conventional, nonadaptive test sections. For most practical purposes, in a real tunnel, interference-free flow about the model can be achieved in an adaptive-wall wind tunnel with imperfect control.

For flexible-wall tunnels, compatibility assessment methods based on wall deflection and pressure have been developed and implemented experimentally[11,20–23]. To streamline the flexible walls, Goodyear[11] applied criteria which matches static pressures in the test section at a wall with pressures computed for an imaginary inviscid flow field over the outside of the same wall. An iterative procedure is applied to change the walls from straight surfaces to streamlines. A very similar adaptive test section was designed and installed at NASA Langley for the cryogenic transonic tunnel[20]. Several other flexible-wall adaptive tunnels have been designed and put into operation for basic and advanced research. Ganzer[21] reported test results from a two-dimensional flexible wall tunnel which was developed with the intention of applying adaptive-wall techniques to a test section for three-dimensional model tests.

For subcritical, nonlifting flow, an analytical simulation of an adaptive-wall tunnel by Lo and Kraft[24] showed that it was possible to find the rate of convergence and establish criteria to achieve unconfined flow in a single adjustment regardless of the initial conditions. Their analysis was valid for two-dimensional flow fields. Dowell[25] formulated a one-step convergence method which was valid for two- and three-dimensional flows. However, his method was subject to the assumption of linearity.

Adaptive-wall experiments conducted at Arnold Engineering Development Center (AEDC) were aimed at finding out the most suitable wall configuration for an adaptive-wall section with particular application to three-dimensional flow[10]. The results of the experiments, carried out with different ventilated wall configurations with adjustable porosity, showed that wall interference was reduced significantly although no completely unconfined flow condition was achieved.

At Ames Research Center, a two-level one-component compatibility assessment was developed by Davis[26]. The method is valid for two- and three-dimensional flows and was developed to exploit the capabilities of Laser Doppler Velocimetry and especially for use with a minicomputer-equipped facility. In this method, only one flow variable is measured at two control levels. Values of the flow variable at the lower control level provide the boundary condition to solve the unconfined flow field at the upper control level. This calculation gives a prediction of the same flow variable at the upper control level which is compared with the measured value to determine the effect of the wall interference. Davis presented numerical simulations of two- and three-dimensional flows along with data from a two-dimensional pilot tunnel. The normal velocity component was measured with a one-component LDV system and Davis' two-level compatibility assessment method was implemented through the use of influence coefficients to accurately determine the local plenum pressure corrections for rapid convergence to interference-free flow[9].

A new adaptive-wall test section was designed and installed at Ames Research Center for a 2x2-foot tunnel on the basis of the experience from the small pilot tunnel experiments. It uses a state-of-the art LDV system with a very fast computer controlled traverse system. Wall control was provided by suction and blowing through the slotted walls by a number of sliding valves which were operated automatically[27].

Development of adaptive-wall test sections for three-dimensional testing has been under way for the last decade and is still in the early, demonstration stage[28–31]. At the University of Southampton, a two-dimensional flexible-wall test section was used for three-dimensional testing[22]. First results showed that the model blockage can be eliminated by streamlining the walls. However, a substantial amount of wall

interference remained. It was reported that research was in progress to develop a suitable algorithm for the wall interference assessment.

For the purpose of a very accurate representation of three-dimensional wall shape, the test section developed at Deutsche Forschungs und Versuchsanstalt für Luft und Raumfahrt (DFVLR) consists of a cylindrical rubber tube that can be deformed by 64 jacks. A one-step method based on the assumption of superposition of pressure disturbances, was developed as a calculation procedure to determine the adapted wall configuration[21].

A three-dimensional test section with eight flexible walls was developed at Technical University of Berlin[21,30]. They form an octagonal cross section and all the walls are subject to a two-dimensional deformation. Problems associated with the algorithm for the calculation of three-dimensional exterior flow field and the control system for wall settings were discussed by Ganzer[30]. Test results with full adaptation of the walls demonstrated the feasibility of the adaptive-wall technique for three-dimensional testing.

At Ames Research Center, a two-dimensional test section was modified to permit cross-stream control for three-dimensional testing[29]. The experiments demonstrated the feasibility of local wall control in a ventilated three-dimensional test section. Although in all the experiments wall interference was reduced, interference could not be completely eliminated. It was concluded that the effects of the wall adjustments on the flow could not be accurately predicted using influence coefficients; in addition, insufficient suction and blowing to produce the required velocity changes was provided.

Application of the adaptive-wall concept to the testing of propulsive lift vehicles has been theoretically investigated by Sears[32]. In a numerical demonstration using panel methods, it was shown that high lift configurations can be tested in an adaptive-wall wind tunnel of the V/STOL type, correcting for gross errors in initial conditions and arriving at approximate unconfined flow conditions. Recently, limited experimental results were reported from a V/STOL tunnel at Arizona University[33]. Results showed that the iterative procedure successfully reduced discrepancies at the control level after about six to eight iterations.

1.3 Motivation of the Present Work

Some of the major problems in the design and operation of ventilated adaptive-wall wind tunnels are the complex instrumentation and the excessive total testing time. These problems are associated with the type of variable to be measured, the data-taking time, and the number of iterations required for convergence.

Assessment of wall interference and proposed correction schemes for adaptive wind tunnels require measurement of two flow variables at control levels at or near the walls of the test section. Any two conveniently measured variables can be used in the adaptive-wall process. In ventilated test sections, the flow variables can be measured using intrusive tools such as probes[8], and/or nonintrusive tools such as Laser Doppler Velocimetry[9,35,36] (LDV) or side-wall static pressure tappings[34–36].

Because of the wide use of slotted-wall test sections at Ames Research Center, adaptive-wall test sections with slotted-walls and local plenum control have been developed. Since the side-walls are not porous, the windows can be used for optical measurement techniques. At Ames Research Center, LDV is currently used to measure velocity components as the flow variables in the compatibility assessment. Although it is a nonintrusive and accurate method, collection of velocity data takes a long time and the LDV system has to be moved along the control levels to get the velocity distribution. It is a complex system and requires special instrumentation. Precise optical alignment and proper seeding of the flow are necessary to ensure accurate data.

If ventilated adaptive-wall wind tunnels are to be used for production testing purposes, adaptive-wall techniques will have to be justified both economically and technically[37]. Basically, the adaptive-wall technique is an iterative process and total testing time must be reduced for production testing purposes. This provides much of the motivation for the present work.

1.4 Present Work

The primary purpose of the present research was to provide solutions to the above-mentioned problems by establishing fast schemes with simple instrumentation. In order to simplify the instrumentation and to reduce the data taking time, the side-wall pressure distribution was proposed as the flow variable[34,35]. One of the major goals of the present experiments was to validate the use of the side-wall pressure distribution in the assessment of wall interference. It is a nonintrusive technique, like Laser Doppler Velocimetry, but it is limited to two-dimensional testing.

As one alternative to reduce the testing time, a one-step convergence scheme was developed and implemented theoretically and experimentally. In adaptive-wall experiments, each iteration requires the measurement of flow variables and application of pressure corrections to the plenum compartments. The main purpose of the one-step scheme is to eliminate intermediate experimental iterations by performing them on the computer, using the information from influence coefficient matrices, instead of taking the measurements repeatedly.

Influence coefficients are required to determine the correction to the flow in the test section. During actual testing, once the wall interference is determined, the amount of suction and/or blowing which would be applied in the plenum chambers is determined using influence coefficients. In the present study, influence coefficients were obtained in three alternative ways, from side-wall pressure distribution, streamwise velocity measurements, and normal velocity measurements. In the iterative and the one-step methods, influence coefficients were employed for a systematic estimation of the pressure corrections. One aspect of the present research was to determine the practical limitations and the effectiveness of the influence coefficients at different Mach numbers and model incidences.

One of the purposes of this study was to investigate the relative merits of the various convergence schemes with different flow variables. Therefore, the iterative and the one-step method were implemented with normal and streamwise velocity components measured using a two-component LDV system and with resultant velocity distribution calculated from side-wall pressure measurements. Emphasis was given

to the convergence schemes applied with a two-level compatibility assessment[26] which requires the measurement of one flow variable at two control levels unlike the one-level method[15] in which two flow variables have to be measured at one control level.

In this study, linearized equations were used to calculate the unconfined flow at the control levels. The linearized compressible potential flow equations are applicable to supercritical flows past the model, provided that shock waves are not strong and do not reach the wind tunnel walls. Therefore, the linearized flow equations can be used up to very high subsonic Mach numbers. However, if the flow near the walls is nonlinear, the transonic small disturbance equation is the appropriate choice to solve the unconfined flow. In this case, the functional relationships can not be obtained analytically. In order to investigate the accuracy of the unconfined solution for supercritical cases, the transonic small disturbance equation was solved using finite difference methods and compared with the unconfined solution obtained from the linear equations.

In Chapters 2 , 3, and 4, theoretical and experimental aspects of the present study are explained in detail. Results of the experiments for the evaluation of the influence coefficients and the adaptive-wall experiments for the application of the various convergence schemes are given in Chapter 5. Results from convergence schemes are compared in Chapter 6. Chapter 7 is devoted to the conclusions and the recommendations for future work.

Chapter 2

Discussion of the Convergence Schemes

2.1 Convergence Schemes

In adaptive-wall experiments, local wall properties are systematically adjusted to achieve unconfined flow by measuring two flow variables and evaluating the functional relationships for unconfined flow. The iterative process can be entirely experimental or it can be carried out computationally by using the one-step convergence scheme[24,25,35]. The primary purpose of this study was to apply a two-level compatibility assessment with the iterative and one-step convergence schemes and determine the relative merits of these two methods.

2.1.1 Iterative Convergence Scheme

In the iterative method with the two-level compatibility assessment[9,26] one flow variable is measured at two control levels. A control level is the chosen interface in the test section between the tunnel wall and the model, along which the flow variables are measured and the compatibility to the free air conditions is assessed. The flowchart of the algorithm used for the iterative method is illustrated in Figure 2.1. Disturbance velocity components were chosen as the flow variables to explain the

steps. After setting the test section Mach number and model angle of attack for desired testing conditions, initial settings of the pressures in the plenum compartments are optional. If they are known approximately prior to the experiments, usually from experience, it would possibly help to reduce the number of iterations. However, for a different model and Mach number, the logical approach is to start with all suction and blowing valves in a closed position. This strategy was chosen for the present experiments.

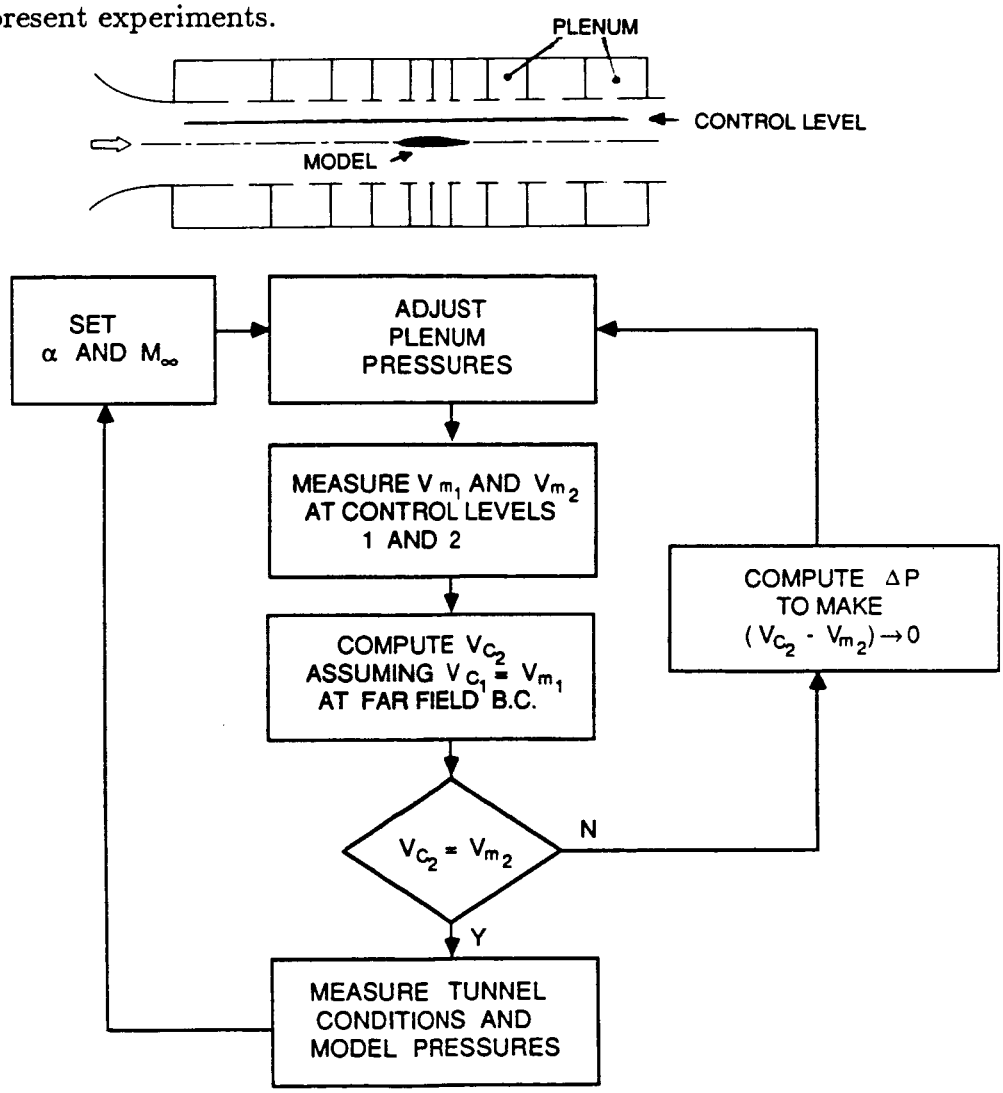

Figure 2.1: The flowchart of an algorithm for the iterative method with the two-level compatibility assessment

The next step in the algorithm is to measure the velocity components at the control levels. The measured velocity component at the first level, v_{m_1}, is used as a boundary condition to evaluate the functional relationships along with the far field boundary conditions to determine the unconfined flow solution, v_{c_2}, at the second level. The effect of wall interference is determined by comparing the measured velocity component with the unconfined solution at the second level. If the measured and the calculated velocities fail to agree, then local plenum pressures have to be adjusted to eliminate this error and to achieve the interference free flow. Required plenum pressure corrections are calculated according to the velocity differences at the control points. Since the velocity component measured at the first level is not at its interference-free condition initially, the unconfined solution is only an estimation, and the pressure corrections will not eliminate the wall interference in one step. Instead this operation leads to an iterative process, eventually converging to the unconfined flow conditions[16,17,19,24]. After the application of the pressure corrections in the plenum compartments, new values of the velocity components are measured. If they are not consistent with the interference-free flow conditions, the process described above is repeated until the matching of the velocity distribution agrees within the range of experimental error. Once this step is reached, measured aerodynamic properties and tunnel conditions will be practically free of wind tunnel wall interference effects.

2.1.2 One-Step Convergence Scheme

The one-step convergence scheme was proposed as an alternative to eliminate the wall interference in a single iteration, or to cut down the number of iterations to a minimum. The one-step scheme developed and implemented in the present study is similar to that proposed by Dowell[25], using the influence coefficients to determine the new distributions of the flow variables at the control levels after adjusting the control variables. However, the present scheme is not subject to the assumption of linearity and simulates the experimental iterative steps numerically rather than trying to compute the required pressure corrections in one calculation. As explained in Chapter 5, the elements of the influence coefficient matrices may change during

iterations depending on whether suction or blowing is applied. Other one-step methods[24,25] do not have this feature which is necessary in practical applications if influence coefficients differ for suction and blowing. The flowchart of the one-step convergence scheme is shown in Figure 2.2, where subscripts 'm' and 'p' stand for measured and predicted quantities, respectively. The unconfined flow solution is denoted with subscript 'c'. Although the one-step scheme will be explained for the two-level compatibility assessment, it can be easily modified for the one-level method.

After the initial steps, which are exactly the same as the experimental iterative scheme described in the previous section, measured velocity components on the control levels are initialized as the predicted values. Similary, the unconfined velocity distribution at the second level is calculated and plenum pressure changes required to eliminate the wall interference are found using the influence coefficients. In the present method, the pressure changes are assumed to be applied to the plena and new velocity distributions at the control levels are predicted using the influence coefficients instead of repeating the measurements. These steps are repeated on the computer until the predicted velocities, which are the counterparts of the measured velocities in the experiments, agree with the calculated values within the prescribed error margin. Once this step is reached, the cumulative pressure change for each plenum compartment, which is the sum of pressure changes assumed to be applied at each step, is calculated. In the actual experiment, these net pressure changes are then applied to the active plenum compartments.

As may be seen from the algorithm, the success of the one-step convergence scheme depends on how accurately the velocity distributions are predicted at the control levels for given pressure changes. If the number of iterations during the experiment were to be reduced to one, the influence coefficients would need to be precisely determined. If the influence coefficients are not sufficiently accurate, this method may not create a one-step convergence. Even then, the number of iterations will be reduced considerably compared to the purely experimental iterative method.

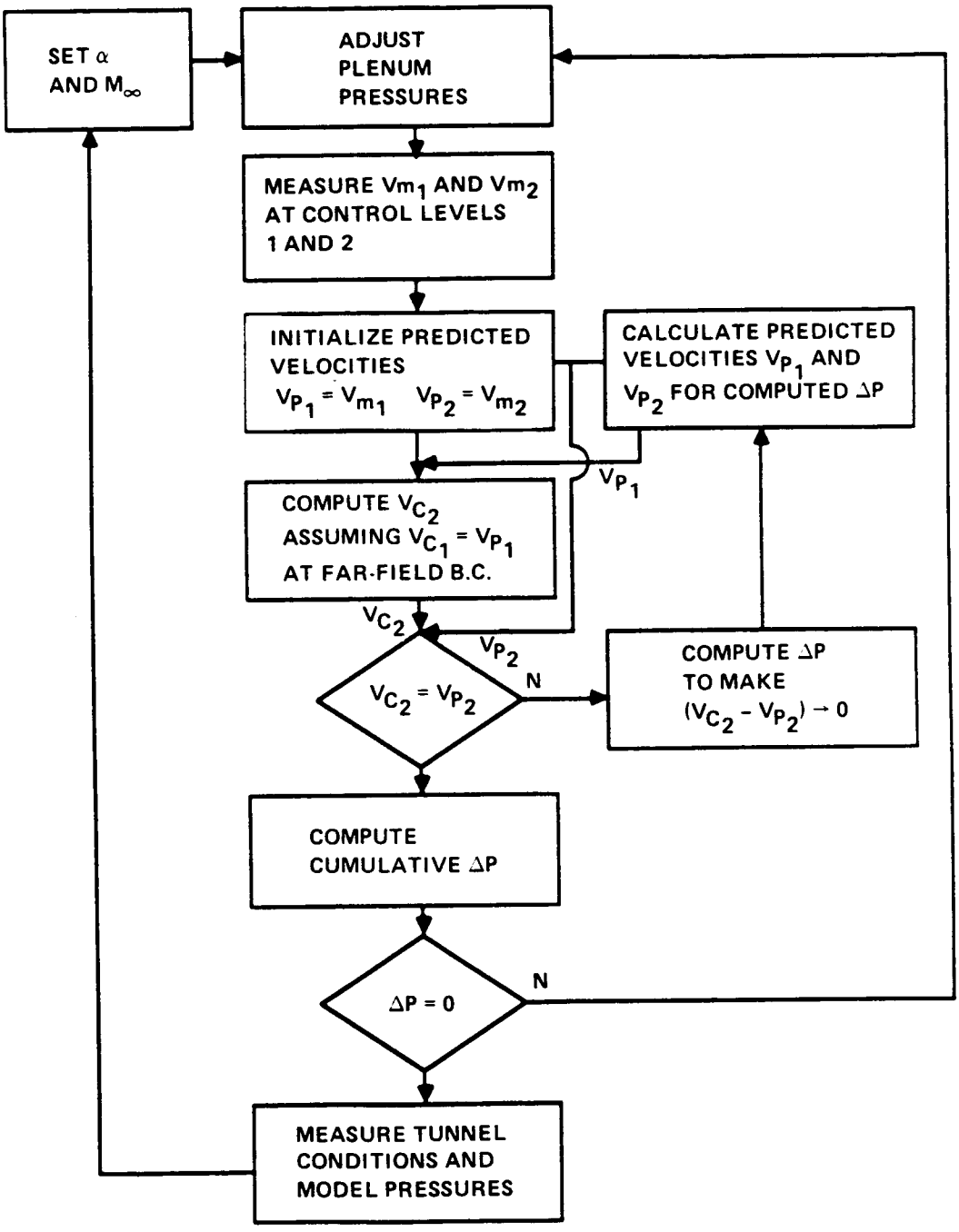

Figure 2.2: The flowchart of an algorithm for the one-step method with the two-level compatibility assessment.

In practical applications, the number of control points is usually larger than the number of plenum compartments and this constitutes an overdetermined system of equations. In the present study, plenum pressure corrections were found in the least squares sense[38] for both convergence methods.

2.2 Influence Coefficients

The use of influence coefficients, especially in the application of the one-step convergence method, is the crucial part in the present adaptive-wall experiments. Influence coefficients are required to determine the corrections to the flow in the test section. For the present ventilated wind tunnel, adaptive-wall control was produced by using the localized plenum pressure control. Once the wall interference is determined, the amount of suction and/or blowing through the plenum compartments to correct this error requires some knowledge of the influence coefficients. Since convergence to unconfined flow is an iterative process, the number of iterations depends on the accuracy of the influence coefficients as well as the degree of interference.

An influence coefficient is defined as the change in velocity at a control point for a unit change of pressure in the active plenum compartment. If ΔV_i is the velocity change produced at control point 'i' , and ΔP_j is the pressure change in the active plenum 'j', then the slope of ΔV_i vs. ΔP_j gives the influence coefficient C_{ij} at that point.

The velocity change produced at any control point due to the pressure changes in more than one plenum was assumed to be equivalent to the sum of velocity changes produced at that point by the same pressure changes in each plenum if applied separately[9]. As a consequence of the assumption of linear superposition, it was possible to form influence coefficient matrices from the following equation:

$$\Delta V_i = \sum_{j=1}^{j=k} C_{ij} \Delta P_j, \qquad i = 1, ..., l \tag{1}$$

where k and l are the number of plenum compartments and control points respectively. Each element of the influence coefficient matrix is defined by $C_{ij} = \Delta V_i / \Delta P_j$.

Equation 1 can be written explicitly as follows;

$$\begin{pmatrix} \Delta V_1 \\ \vdots \\ \Delta V_i \\ \vdots \\ \Delta V_l \end{pmatrix} = \begin{pmatrix} \frac{\Delta V_1}{\Delta P_1} \cdots \frac{\Delta V_1}{\Delta P_j} \cdots \frac{\Delta V_1}{\Delta P_k} \\ \vdots \\ \frac{\Delta V_i}{\Delta P_1} \cdots \frac{\Delta V_i}{\Delta P_j} \cdots \frac{\Delta V_i}{\Delta P_k} \\ \vdots \\ \frac{\Delta V_l}{\Delta P_1} \cdots \frac{\Delta V_l}{\Delta P_j} \cdots \frac{\Delta V_l}{\Delta P_k} \end{pmatrix} \begin{pmatrix} \Delta P_1 \\ \vdots \\ \Delta P_j \\ \vdots \\ \Delta P_k \end{pmatrix} \tag{2}$$

In Equation 1, ΔV_i is the total change in the velocity due to the the pressure changes in the active plenum compartments. In the definition of C_{ij}, ΔV_i is the change in the velocity at a control point due to the pressure change in one plenum compartment.

For the construction of the influence coefficient matrix, the velocity change at a control point was obtained using the following algorithm. The pressure in each plenum compartment was varied systematically and the desired velocity component was measured at each point on the control levels 1 and 2 which are illustrated in Figure 2.3. For each plenum compartment, initial velocity distributions were taken with all the control valves in closed positions. In the subsequent runs, suction or blowing was applied in the active plenum compartment at five different valve settings while the control valves for the rest of the plenum compartments were kept closed. This procedure was repeated for each plenum compartment.

The velocity change at a control point due to the pressure change in a plenum compartment was obtained using the following equation:

$$\Delta V_i = (U_i - U_{ref})_{(n)} - (U_i - U_{ref})_{(o)} \tag{3}$$

where i is the i^{th} control point and U_{ref} is the freestream velocity used as a reference value. U_i is the velocity calculated from side-wall pressure distribution or the streamwise velocity component measured with the LDV system. In Equation 3, 'n' represents the case when suction or blowing is applied in the active plenum compartment, and 'o' refers to the case when all valves are in the closed position.

For the normal velocity component, the reference velocity is assumed to be negligible upstream, since the normal disturbance velocity component goes to zero

far away from the model. Thus, the change in the normal velocity at a control point can be written as

$$\Delta V_i = (v_i)_{(n)} - (v_i)_{(o)} \tag{4}$$

The pressure change in a plenum compartment is simply taken as

$$\Delta P_j = (P_j)_{(n)} - (P_j)_{(o)} \tag{5}$$

where j is the j^{th} plenum compartment.

Since the plenum compartments were arranged symmetrically with respect to the centerline of the test section, they could be grouped in pairs. In this work, unless otherwise stated, plenum compartment j refers to both top and bottom plenum compartments located symmetrically at the j^{th} location (See Figure 2.3). During the experiments carried out to determine the influence coefficients, suction or blowing was applied symmetrically through top and bottom plenum compartment j.

A series of experiments was carried out to evaluate the influence coefficients from the side-wall pressure distribution, streamwise velocity distribution, and normal velocity distribution[34,35]. For each plenum compartment and control point, influence coefficients were evaluated for suction and blowing at different Mach numbers with and without the model. In the case of the side-wall pressure distribution, influence coefficient matrices were formed by the data taken without the model, while those for the streamwise and the normal velocity components were constructed from the data taken in the presence of a nonlifting model. The effects of model, Mach number, location of control points, suction and blowing on the influence coefficients were evaluated. Linearity and the validity of superposition of the influence coefficients were investigated. Experimental results and the evaluation of the influence coefficients are discussed in detail in Chapter 5.

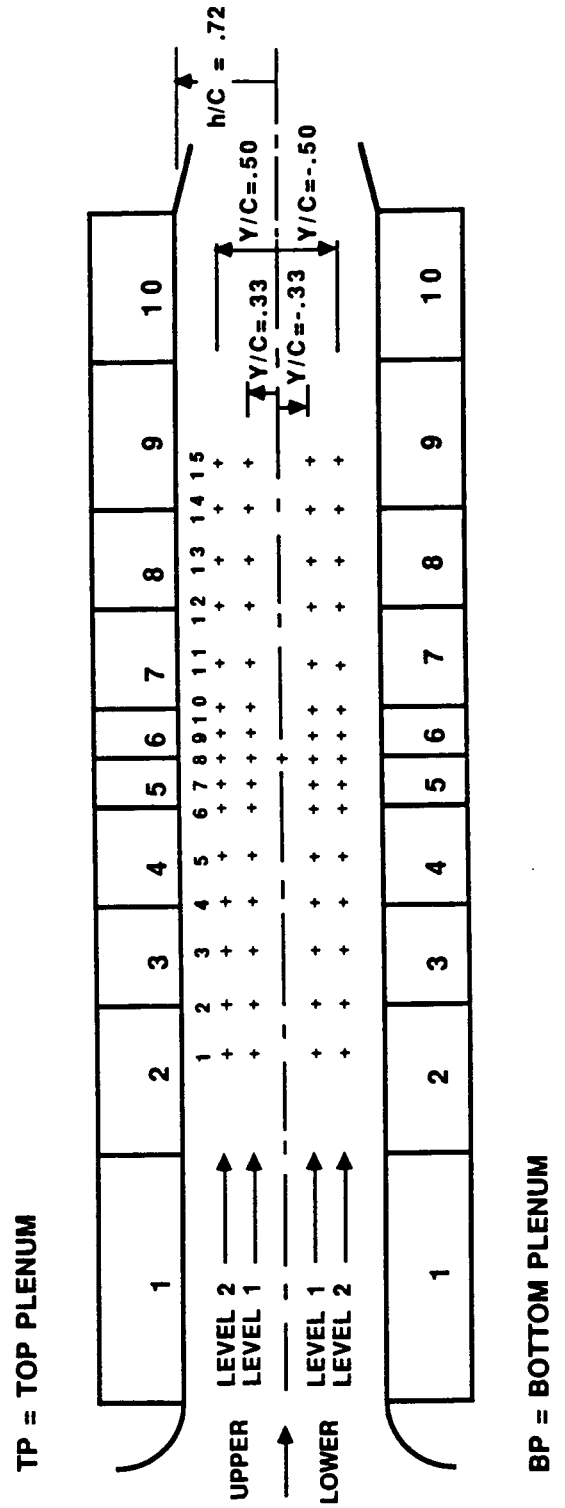

Figure 2.3: Test section arrangement for the adaptive-wall tunnel experiments.

Chapter 3

Unconfined Flow Analysis

Calculation of the unconfined flow is the principle theoretical aspect of the adaptive-wall concept. A suitable functional relationship is evaluated to find the unconfined flow field external to the chosen control level.

In the present experiments, control levels were far enough away from the model and top and bottom wall boundary layers so that the regions of complicated flow patterns and viscous effects such as separated flow regions, shock-boundary layer interaction, were avoided. The undisturbed freestream velocity was always subsonic and the disturbances at the control levels were assumed to be sufficiently small that the small disturbance equations would be a valid approximation. Throughout this study, linearized compressible potential flow equations were used to solve the unconfined flow field. To employ the more complex nonlinear transonic small disturbance equations on line, a powerful dedicated computer would have been required.

3.1 Linear Solution

The governing partial differential equation for two-dimensional linear subsonic flow is the Prandtl-Glauert equation which can be expressed as:

$$\beta^2 \phi_{xx} + \phi_{yy} = 0 \tag{6}$$

where

$$\beta = \sqrt{1 - {M_\infty}^2}$$

Equation 6 was solved in two different ways in accordance with the type of compatibility assessment used in the adaptive-wall experiments.

For the one-level two-component assessment method, the solution of the unconfined flow field is related to the solution of Equation 6 for a half space using Cauchy's Integral Equation[39] (Figure 3.1). The unconfined flow solution for the normal velocity component at $y = \pm h$, for the boundary conditions given in terms of the streamwise disturbance velocity, along with the far-field condition that the streamwise disturbance velocity vanishes, is given as[7,15]:

$$v(x, \pm h) = \pm \frac{\beta}{\pi} \oint_{-\infty}^{+\infty} \frac{u_m(\xi, \pm h) d\xi}{\xi - x} \tag{7}$$

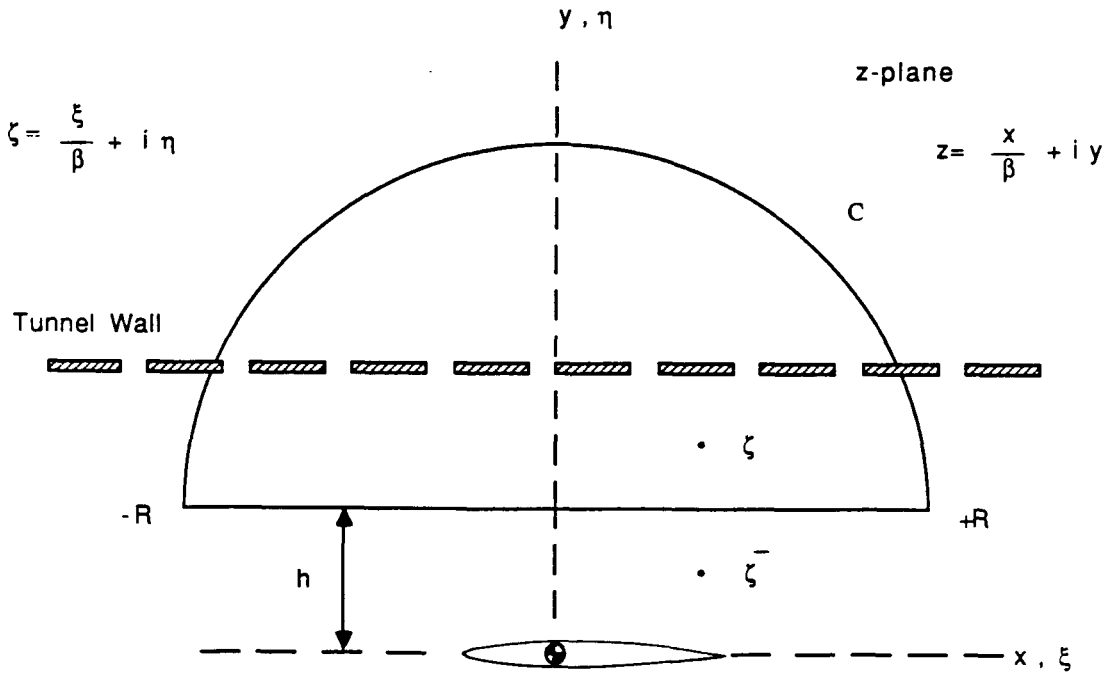

Figure 3.1: Computational domain used for the calculation of unconfined flow using Cauchy's Integral Equation.

If the boundary conditions are given in terms of the normal disturbance velocity, then the unconfined flow solution for the streamwise disturbance velocity component is:

$$u(x, \pm h) = \mp \frac{1}{\pi\beta} \oint_{-\infty}^{+\infty} \frac{v_m(\xi, \pm h) d\xi}{\xi - x} \tag{8}$$

Equations 7 and 8 must be evaluated in the sense of the Cauchy principal value. For the present applications, the singularity in each of these equations was removed using a method suggested in Reference 40 and the integral was evaluated by using spline fit[41] values of the measured velocities, v_m or u_m. The derivation for the removal of the singularity is given in Appendix A.

For the two-level one-component assessment method, a solution to the Prandtl-Glauert equation for a half plane using the normal velocity component was suggested by Davis[26]. By differentiating Equation 6 with respect to x, the following differential equation for the streamwise velocity component can be obtained:

$$\beta^2 u_{xx} + u_{yy} = 0 \tag{9}$$

The following boundary conditions are imposed to solve the unconfined flow field in the region shown in Figure 3.2:

$u = u_m(x)$ at $y = h_1$ and $-\infty < x < +\infty$

$u \to 0$ as $r = \sqrt{x^2 + y^2} \to \infty$

Solution to this boundary value problem can be found using Poisson's Integral Formula for a half plane[39] along with the Prandtl-Glauert correction. For the streamwise disturbance velocity component, it can be written as:

$$u(x, y) = \frac{\beta(y - h_1)}{\pi} \int_{-\infty}^{+\infty} \frac{u_m(\xi, h_1) d\xi}{(x - \xi)^2 + \beta^2 (y - h_1)^2} \tag{10}$$

and at the upper control level, $y = h_2$, it is simply as follows:

$$u(x, h_2) = \frac{\beta\, h}{\pi} \int_{-\infty}^{+\infty} \frac{u_m(\xi, h_1) d\xi}{(x - \xi)^2 + \beta^2\, h^2} \tag{11}$$

where $h = h_2 - h_1$. The same solution is also valid for the lower region. Since the boundary conditions are imposed at the control levels independently in each region,

region, the flow field is decoupled with the requirement that the measurements must be made along the boundaries far enough away from the model. This is necessary to insure that the contributions from both regions are small. It is noted that the integral in Equations 10 and 11 is nonsingular for the two-level compatibility method compared to the one-level assessment method. It can be evaluated using a simple numerical integration scheme.

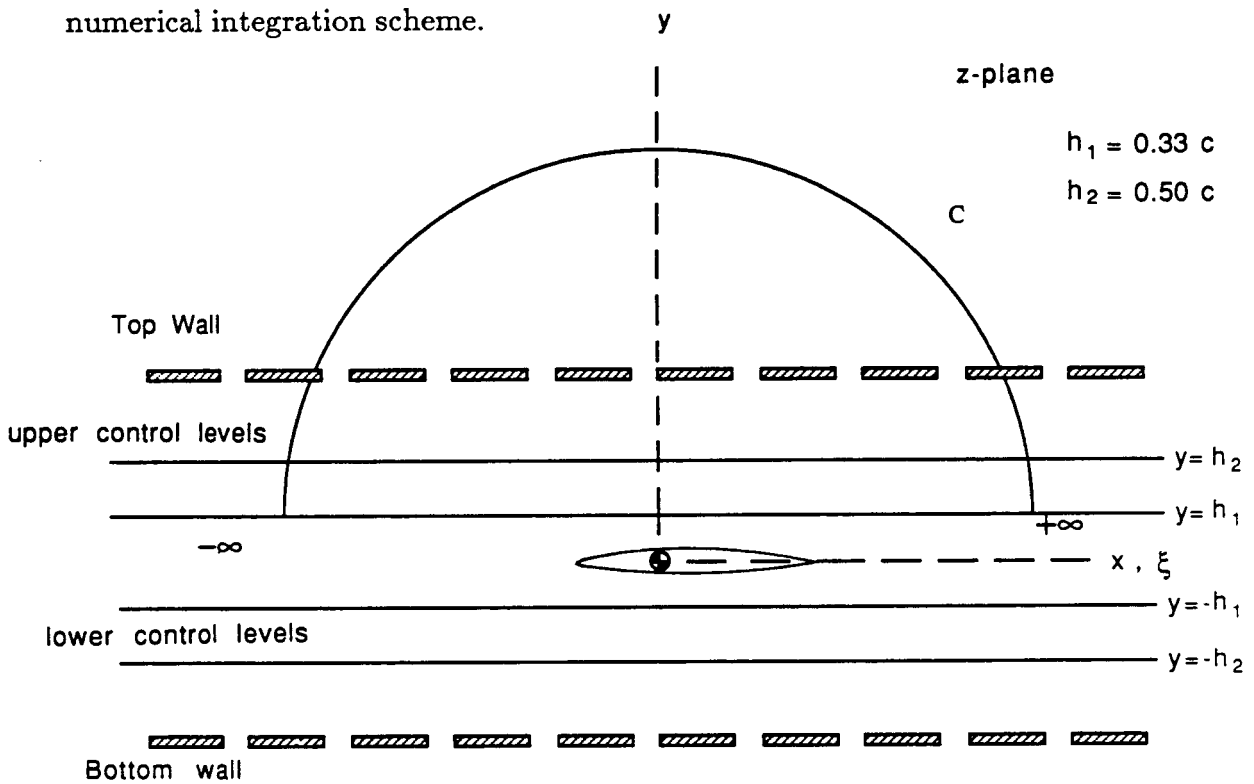

Figure 3.2: Computational domain used for the calculation of unconfined flow for two-level assessment method.

3.2 Nonlinear Solution

It is appropriate to use the transonic small disturbance equation when the flow is supercritical at the control surfaces. However, during the experiments, the computing power of the dedicated computer was not sufficient to employ it on line. Later, the solutions obtained from the linear equations were compared with the

solutions from the nonlinear equation to determine the accuracy of the method for the present Mach number range.

The governing equation for the small disturbances in the transonic flow field is given as[4]:

$$(1 - M_\infty^2 - (\gamma + 1)M_\infty^2 \frac{\phi_x}{U_\infty})\phi_{xx} + \phi_{yy} = 0 \qquad (12)$$

where $\phi_x = u$ and $\phi_y = v$ are the streamwise and the normal disturbance velocity components respectively.

Boundary conditions for the streamwise velocity component are imposed as follows:

$\phi_x = u \to 0$ as x *and* $y \to \infty$

$\phi_x = u_m(x)$ at $y = \pm h_1$ and for $-\infty < x < +\infty$

Equation 12 was solved numerically using the Murman-Cole method with Gauss-Seidel line relaxation in the computational plane shown in Figures 3.3a and b. The derivation is given in Appendix B.

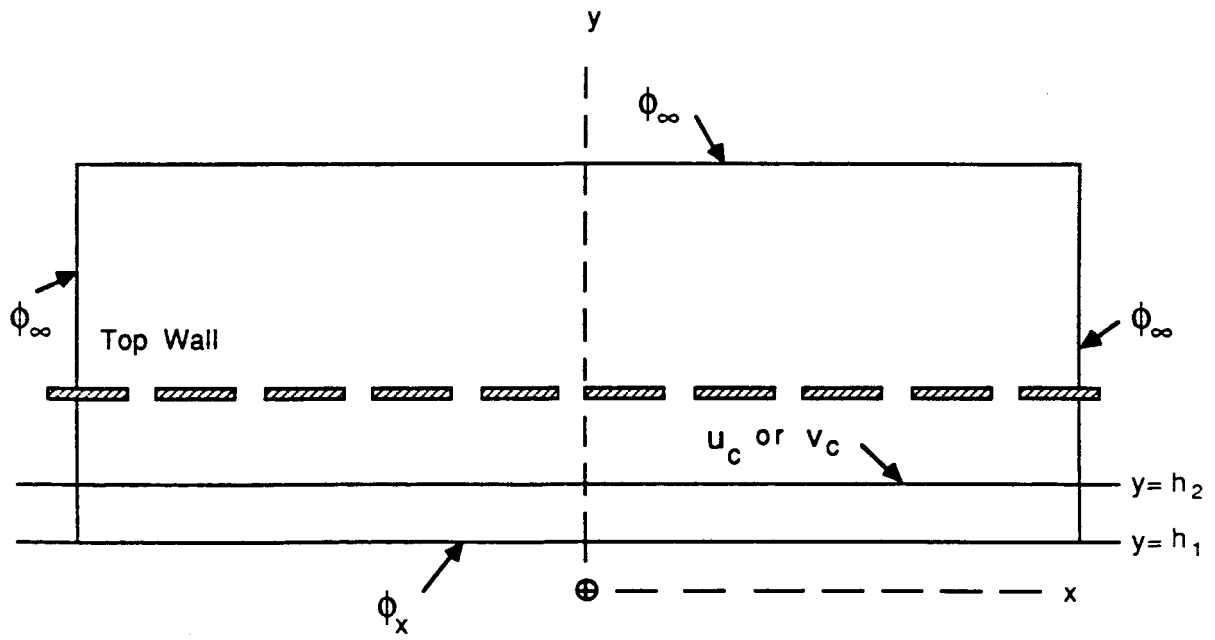

Figure 3.3a: Physical domain with boundary conditions for the transonic small disturbance equation.

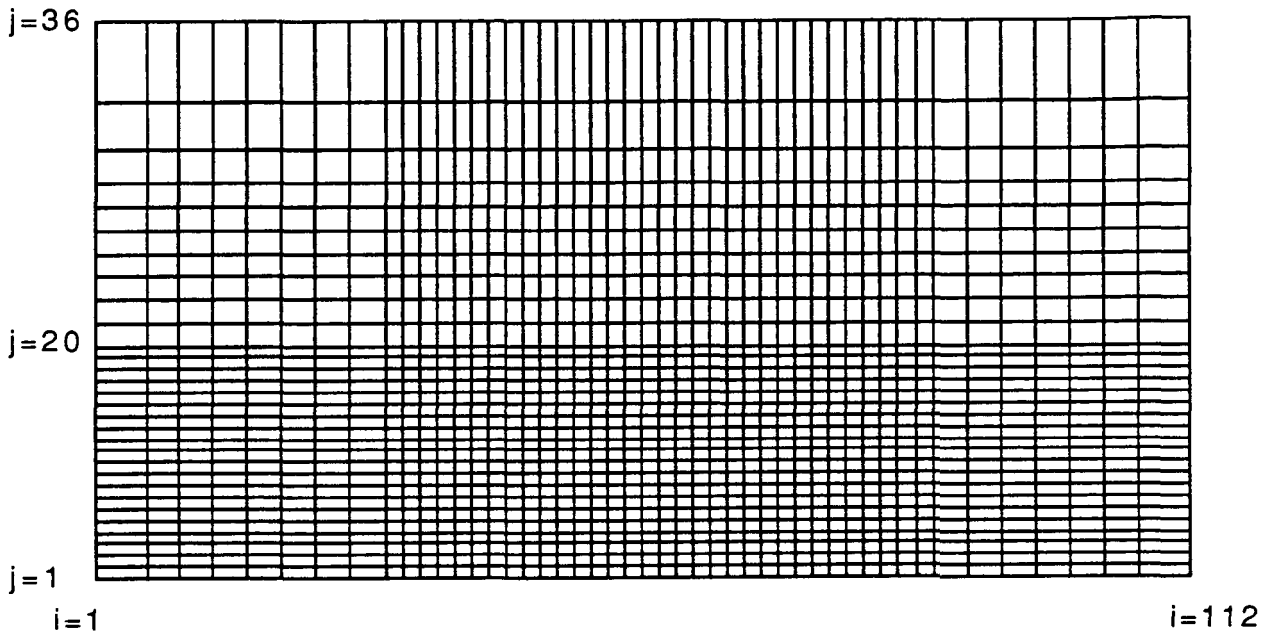

Figure 3.3b: Computational mesh for the calculation of unconfined flow using transonic small disturbance equation.

3.3 Discussion

As previously stated, one of the purposes of this study was to use the resultant velocity determined from the side-wall pressure distribution as the flow variable. Since the flow angle was not measured in the present experiments, the calculated resultant velocity distribution could not be resolved into its streamwise and normal components. The velocity measurements taken with the LDV system showed that the magnitude of the resultant velocity was comparable to the streamwise component. For the resultant velocity distribution from side-wall pressure measurements, unconfined flow calculations had to be carried out approximately by

assuming that the streamwise velocity component is large compared to the normal disturbance velocity component. In order to find the error introduced with this assumption and the feasibility of this approach in the adaptive-wall concept, the iterative steps of the schemes with the streamwise velocity distribution were reconstructed computationally implementing the resultant velocity distribution in the unconfined flow calculations. In this case, resultant velocity distributions were calculated from streamwise and normal velocity components which were measured with the LDV system. Results and discussion of this assumption are given in Chapter 5.

Since the flow is symmetrical with respect to the centerline of the test section at zero angle of attack, only the upper half of the computational plane was used to solve the unconfined flow field. In the case of a lifting airfoil, unconfined flow calculations were performed separately for the upper and the lower computational planes. It was assumed that the upper and lower flow fields were decoupled for small model incidences.

Chapter 4

Experimental Apparatus and Data Acquisition

4.1 Experimental Setup

4.1.1 Wind Tunnel

Experiments were conducted in the ventilated adaptive-wall wind tunnel at Ames Research Center. It is a continuous flow, indraft wind tunnel equipped with a flexible downstream throat to control the test section Mach number, and an auxiliary system to provide suction and blowing of air through the plenum chambers. The adaptive-wall test section with slotted walls is of rectangular cross section, 25 cm. x 11 cm. and is 61 cm. long. The tunnel is operated at atmospheric pressure. The upper and lower walls each have 10 longitudinal slots with a total open area ratio of 12-percent. The test section has separate top and bottom plenums and each was divided into 10 plenum compartments by transverse inserts. The transverse plates can be removed and inserted easily, so that number of plenum chambers can be varied in increments of 2.54 cm. A schematic of the wind tunnel along with a typical connection of a plenum compartment to the auxiliary system is illustrated in Figure 4.1.

The tunnel is operated with the throat choked to assure a steady flow in the test

section and to minimize the noise propagated from the control gate valve. Throat height is changed by using an electric motor whose speed is controlled by a drive unit. A digital voltmeter is used to monitor the throat height.

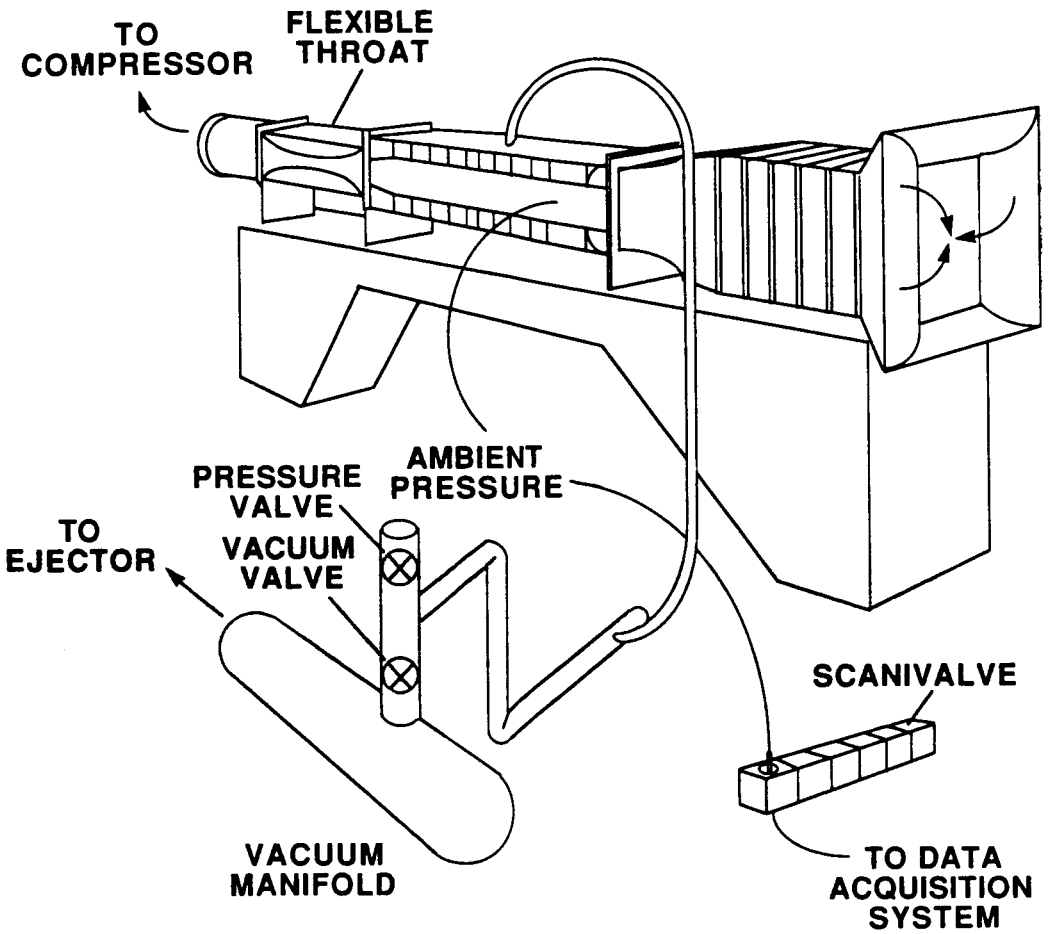

Figure 4.1: Schematic of the 25 cm x 11 cm NASA Ames indraft wind tunnel.

Each plenum compartment was connected to an auxiliary air system which provided suction and/or blowing when required (Figure 4.1). Blowing in a plenum compartment was obtained by opening the corresponding pressure valve to atmospheric pressure. An ejector which provided 16 inches of Hg. vacuum pressure (gage) at the maximum setting, was used for suction. It was connected to a vacuum manifold to which all the plenum compartments were connected. During the experiments the vacuum and pressure control valves were operated manually.

4.1.2 Model

For the experiments, a 7.62-cm.-chord NACA 0012 airfoil without boundary layer trips was used. It had a 25 cm.-span and was instrumented with 16 pressure tappings on the upper surface and 9 tappings the lower surface. The blockage ratio of the model in the test section was 8.3 % and it was expected to create significant wall interference effects at high speeds. The aspect ratio of the model, tunnel width/model chord, was 3.28 and tunnel height/model chord ratio was 1.44. This airfoil section was chosen because of the large body of experimental data and numerical solutions that exist for its aerodynamic characteristics, especially at transonic speeds. It is used for helicopter rotors and has been selected as one of the standards by AGARD to be used as an experimental data base for the validation of advanced Computational Fluid Dynamics codes. Figure 4.2 shows the airfoil section with orifice locations.

4.2 Instrumentation

Figure 4.3 shows the block diagram for the instrumentation used in the adaptive-wall experiments. A pitot tube and thermocouple unit were mounted upstream of the test section to measure the total pressure and ambient temperature.

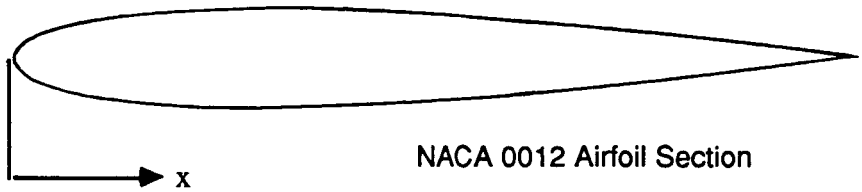

Upper surface	Lower Surface
X/C	X/C
0.025	0.050
0.050	0.100
0.100	0.200
0.150	0.300
0.200	0.400
0.250	0.500
0.300	0.600
0.350	0.700
0.400	0.850
0.450	
0.500	
0.550	
0.600	
0.700	
0.800	
0.900	

Figure 4.2: Pressure orifice locations of NACA 0012 airfoil model.

4.2.1 Instrumentation for the Pressure Measurements

Plenum, model and control level pressure distributions were measured using Scanivalves. Calibration pressure was supplied by a vacuum pump and measured with a separate unit. A Paroscientific pressure computer was used to measure ambient pressure. Throat, test section and plenum pressures were also monitored on the manometer board during the experiments. Side-wall static pressure distributions at the control levels were measured with a number of pressure tappings located on

one of the side-walls. A six-unit Scanivalve system was used to measure the stagnation pressure, top and bottom plenum pressures, top wall pressure distribution, downstream throat pressure and side wall pressure distribution.

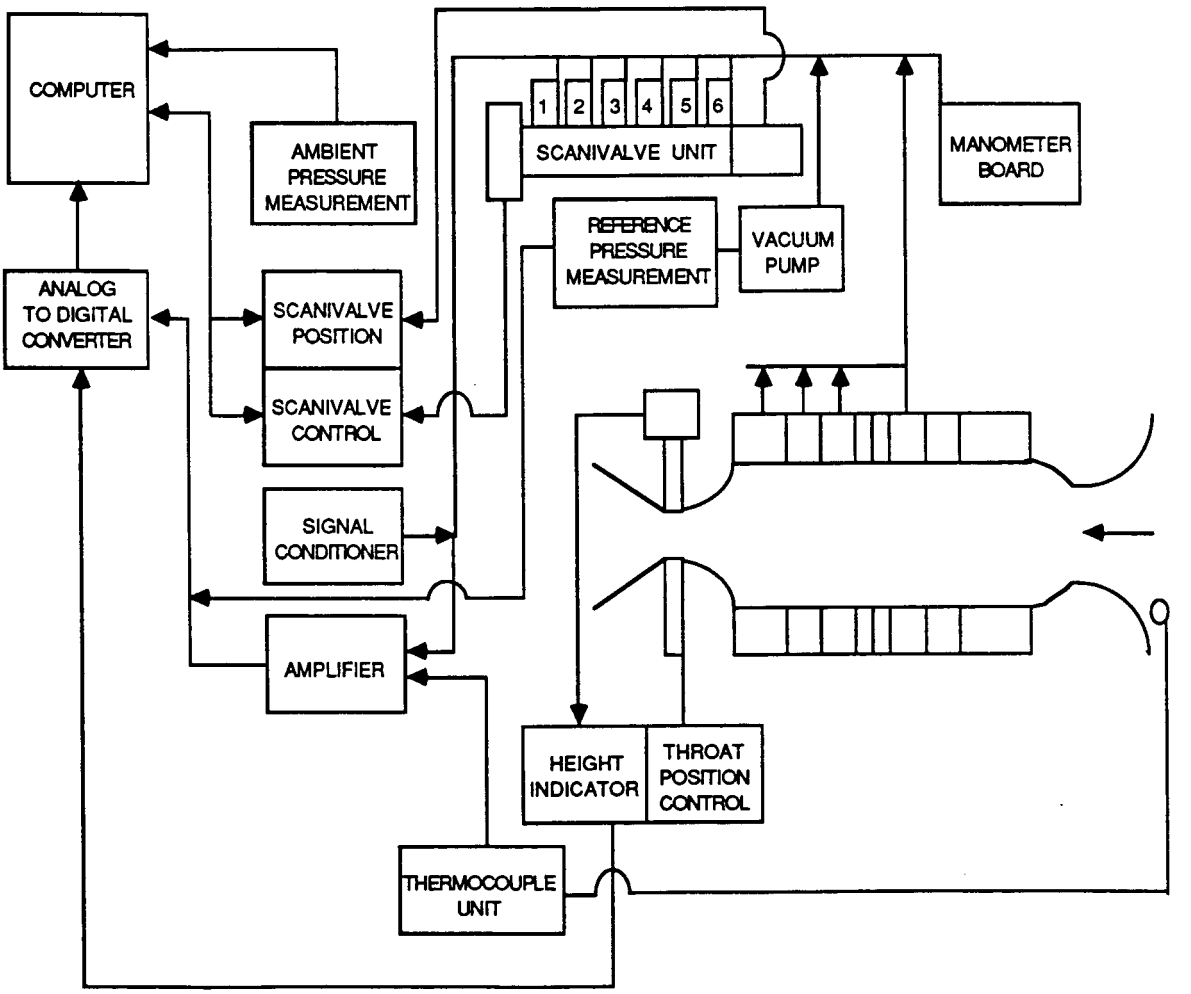

Figure 4.3: Adaptive-wall wind tunnel instrumentation.

Each Scanivalve unit had 24 ports which were connected to the pressure tappings. The side-walls were made of plexiglass and one of them was instrumented with seven rows of pressure orifices along the test section with a total of 141 pressure tappings. They were located symmetrically above and below the centerline. In order to best resolve the flow field, the pressure tappings were closely spaced near the region where the model was located (Figure 4.4).

Calibration of the Scanivalves

The transducers in the Scanivalve system were of the differential type with a range of ± 5 psig. In order to calibrate them, a calibration pressure generated by an electric vacuum pump was applied in one port of each Scanivalve unit. Another port was tapped to the atmosphere. The atmospheric and calibration pressures were each measured by alternate methods. These two known pressures and the values given for them by each transducer allowed the Scanivalves to be calibrated.

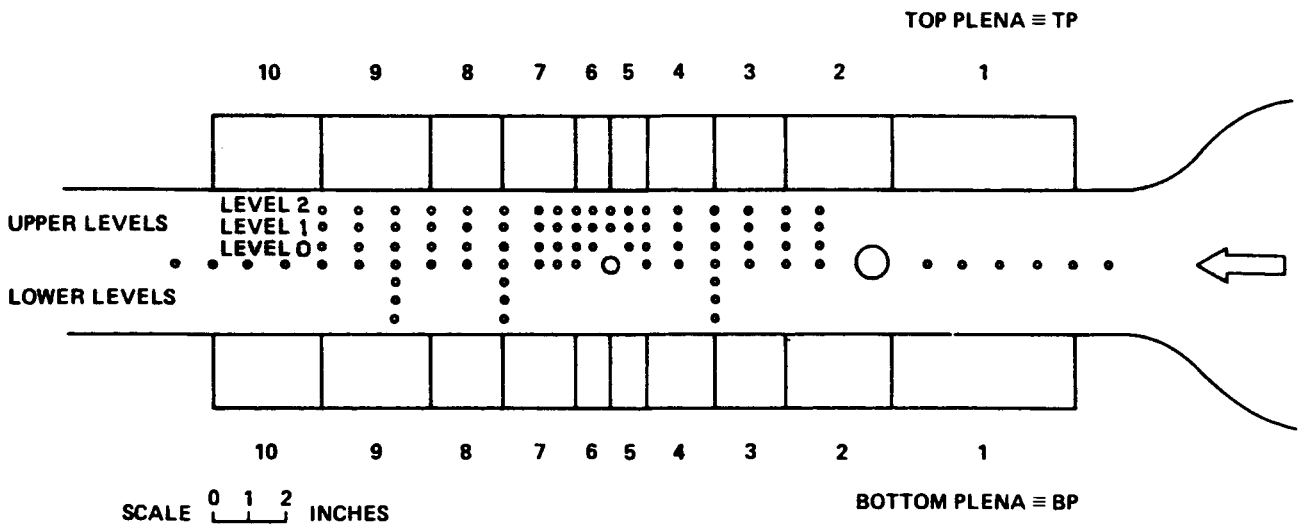

Figure 4.4: Adaptive-wall wind tunnel test section arrangement for the side-wall pressure measurements.

4.2.2 Laser Doppler Velocimeter

Velocity measurements at the control points were taken with a two-component Laser Doppler Velocimeter system. A schematic of the LDV system is given in Figure 4.5.

A 5W Argon-Ion laser (Spectra-Physics Model 64) was used in the forward-scatter LDV system. The laser is configured with an end cavity multiline reflector which allows it to operate in the multiline mode. In this operating mode, the resultant beam is comprised of all wavelengths which are inherent to the Argon-Ion unit. An external collimater is not required since the resultant beam exits the laser in a fairly well collimated state. A broadband polarization rotator mounted at the exit of the laser is used to rotate the polarization vector from the vertical to the horizontal plane before the color separator unit which comprises of a pair of Brewster angle prisms. The polarization of the beam should be in the plane formed by the beam and the normal to the prism surface to obtain the maximum transmittance[42]. Two higher power color lines, green (514.5 nm) and blue (488 nm), are guided by means of turning mirrors to the Bragg cells. Before the Bragg cell, the green beam is passed through a half-wave plate to rotate the plane of polarization 90° so that all the optical components for the green line will lay within the same plane to avoid the unwanted rotations of the polarization vector. Each color line is split into two equal-intensity, slightly diverging beams while they are passed through the Bragg cells. A Bragg cell is an acousto-optical device which induces a 40 MHz modulation in one of the beams in each pair. For each color, the two diverging beams are then made parallel by passage through an alignment prism. The prism should lay in the same plane with the Bragg cell to insure that the parallel beams will not be skewed. Small corrections are made possible using a polarizing beam-splitter cube while filtering out the unwanted polarization. Turning mirrors are used to guide the resulting beams through the translation stages. By means of a lens, the beams are crossed at the desired point in the test section. Prior to the lens, all four beams must be parallel and symmetrical to the axis of the lens to focus to a common point.

The receiving optics is an off-axis, forward-scatter configuration which gives flexibility to the system. It can be adjusted for different requirements; if maximum

signal strength is required, angular deviation from the axis of symmetry should be kept to a minimum. Angular deviation can be kept as large as possible, depending on the physical limitations, if focusing on the smallest part of the probe volume is of interest. The first lens in the receiving optics collects the scattered light and the second lens makes the collected beam parallel. A parallel beam is required by the polarization beam splitter and the line filters for maximum efficiency. While the green lines pass straight through the beam splitter, blue lines are deflected upward. The line filters eliminate any cross-talk caused by impure polarization. Each line filter is followed by a lens which focuses the light onto a pinhole aperture of the corresponding photomultiplier tube (PMT). The PMT's convert the light energy to electrical signals which are passed on to the signal processors. Preamplifiers are located in the PMT housing to increase the signal amplitude before driving relatively long cables. The preamplifier is kept close to the photodetector in order to increase the signal level before additional electronic noise affects the signals. An additional amplifier is also used to increase the signal strength prior to the high pass filter. A sine-wave generator provides the mixing frequency before the passive diode mixer, after which the output is fed to the signal processors. The signal processors used in the experiments were of the counter type (Microdyne 2000 series) which have good resolution and noise handling characteristics. These units employ circuitry with bandwidths in excess of 1 GHz which has been applied under single particle, multiparticle and multivelocity conditions. In addition to the basic 5/8 (or 10/16) signal validation criteria and oversize particle rejection, a sophisticated multilevel sequence validation has been added. This allows the experimenter to select the criteria which will yield best data for a given signal-to-noise ratio, signal level, seeding level, doppler frequency and fluctuation, indicative of the test situation.

Calibration of the Laser Doppler Velocimeter System

At the probe volume, the fringe spacing, δ, is determined using the following formula[42];

$$\delta = \frac{\lambda}{2sin(\frac{\theta}{2})} \tag{13}$$

where λ is the wavelength and θ is the angle of the intersecting beams.

Knowing the fringe spacing and the time required for a given number of crossings, particle velocity can be determined. In practice, this method may not give accurate results because of small misalignments of the optics. It is best to calibrate the system by measuring the scattered light from an object moving at a known velocity. A rotating disk is usually the most convenient tool for this purpose.

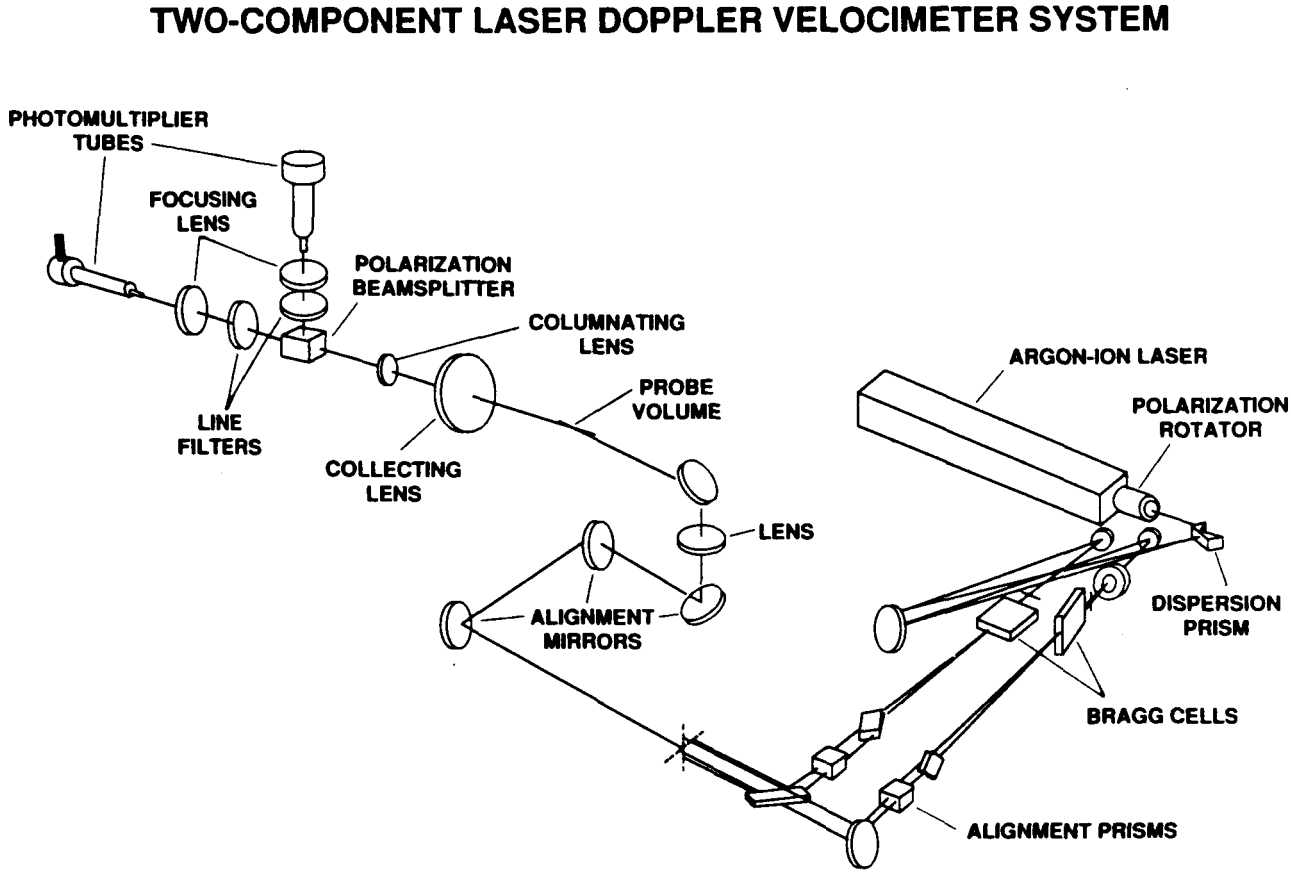

Figure 4.5: Schematic of the Laser Doppler Velocimeter system.

Seeding Requirements

Seeding of the flow is an inconvenient necessity of the LDV technique. The LDV actually measures the velocity of the small particles which are assumed to move with the flow. Size of the particles and the concentration distribution are important factors which may adversely affect the results. For most gas flows, particle sizes on the order of 1 μm are often accepted as adequate[42]. Smaller particles will contribute to the background noise although they may not be detectable by the instrument while larger particles may not adequately track the flow.

In the present study in an attempt to reduce the data taking time, the flow was seeded with 0.5-micron-diameter polystyrene spheres diluted with denatured alcohol . Analysis and the experimental results[44] have shown that these particles respond to the motion of aerodynamic test flows with excellent accuracy. This seeding technique also avoids deposition of the seed material on the test section windows as is the case for oil-based seed.

4.3 Data Acquisition

The number of control points was variable in the application of the convergence schemes with the maximum number being 15 control points at each control level. A minicomputer dedicated for the adaptive-wall wind tunnel experiments was used for the data acquisition and real-time data analysis. Pressure, velocity and temperature measuring devices were interfaced with the analog-to-digital converter of the computer. A traversing system, whose driving motors were controlled by a programmable control unit interfaced with the computer, was used to move the probe volume to the desired location for the LDV measurements.

4.3.1 Velocity Calculations from Pressure Measurements

Assuming isentropic flow, the Mach number, M can be calculated from the stagnation pressure, P_t, and the static pressure, P, measured at the control point:

$$M = \left[((\frac{P_t}{P})^{\frac{\gamma-1}{\gamma}} - 1)(\frac{2}{\gamma - 1})) \right]^{\frac{1}{2}} \tag{14}$$

Then, the velocity is given by:

$$V = Ma \tag{15}$$

where

$$a = \sqrt{\gamma RT} \tag{16}$$

where $\gamma = 1.4$ and T is obtained from the total temperature, T_t, using the following formula:

$$T = \frac{T_t}{1 + \frac{\gamma-1}{2} M^2} \tag{17}$$

4.3.2 Velocity Calculations from LDV Measurements

The Macrodyne signal processor used in the experiments utilizes a 1 GHz counter. The number of counts for the passage of 8 cycles is sent to the digital I/O in the form of a 10-bit mantissa and 4-bit exponent. The signal frequency, f_s, is determined from the following equation [43]:

$$f_s = \frac{1}{t_s} = \frac{2^{5-exponent} 1000}{mantissa} \tag{18}$$

where f_s is obtained in MHz and t_s is the period of the signal when 8 cycles are measured. Exponent and mantissa are set on the signal processor for the desired signal conditions.

Since the signal frequency, f_s, is a linear combination of the Doppler frequency, f_D, the shift frequency, f_{shift}, and the mixing frequency, f_{mix}, the Doppler frequency can be obtained from:

$$f_D = f_s - f_{shift} + f_{mix} \tag{19}$$

Once the Doppler frequency of a particle is known, its velocity can be determined from:

$$V = c_0 f_D \tag{20}$$

where c_0 is the constant which is determined based on the fringe spacing or direct calibration.

4.3.3 Reynolds Number and Model Pressure Coefficient

Test section Reynold Number based on the airfoil chord length is calculated from:

$$Re = \frac{V_\infty c}{\nu} \tag{21}$$

where V_∞ and c are the freestream velocity and the model chord length respectively. ν denotes the kinematic viscosity.

Model pressure coefficients are calculated from the measured pressure distribution on the model surface from:

$$Cp = \frac{p - p_\infty}{\frac{1}{2}\rho_\infty V_\infty^2} \tag{22}$$

or by using compressible flow equations, Equation 22 is arranged as:

$$Cp = \frac{2}{\gamma M_\infty^2}\left[(\frac{p}{p_t})(1 + \frac{\gamma - 1}{2}M_\infty^2)^{\frac{\gamma}{\gamma-1}} - 1\right] \tag{23}$$

where p/p_t and M_∞ are obtained from measurements.

4.4 Error Analysis

4.4.1 Error Analysis in the Measurements

Pressure Measurements

An average of 200 samples in a period of 5 microseconds was taken as the mean value in the pressure measurements. Precision of the A/D converter is given as ± 1

count in the full range of 16383 counts at maximum. Repeatibility of the pressure measurements were accurate up to the last digit in counts which corresponds to a relative error in a range from 0.1 % to 0.05 %.

Velocity Measurements

For velocity measurements, 1000 samples were taken by the LDV system in each velocity direction (x and y) at every measurement location. The coincidence of the data from the two channels was confirmed within the controlling software. In the data reduction, statistical mean and standard deviation based on 1000 samples were computed first. A histogram was formed plotting the frequency versus the number of samples at each frequency to determine if the data is conforming to the normal distribution as a real time performance check. Standard deviation was of the order of 1.0 m/s at lower Mach numbers ($M \sim 0.5$). At higher Mach numbers ($M \sim 0.7$), it increased slightly, but it stayed less than 2.0 m/s. The average velocity at each location was calculated based on the number of samples that fell into a region bounded by a value of the two-thirds of the maximum value on the histogram. This procedure was used to improve the data quality by removing any bias error. In the experiments, the number of samples used in the velocity calculations with this method varied between 700 and 950. Mean velocity based on 1000 samples usually agreed with the velocity calculated from the new procedure of the order of ~ 0.5 m/s at lower Mach numbers. At higher Mach numbers, this value increased, possibly because of condensation effects. It should be noted that the standard deviation values given here were based on 1000 samples. Therefore, it was concluded that the new procedure gave better estimates. Repeatibility of the velocity measurements varied between ± 0.3 m/s and ± 0.6 m/s on average.

4.4.2 Error Analysis for the Convergence

In the present experiments, the root-mean-square (rms) error criteria was used as a measure for the convergence to the interference-free flow conditions in the applications of the adaptive-wall schemes. The rms error in terms of streamwise

velocity was defined as;

$$rms = \sqrt{\frac{1}{l}\sum_{i=1}^{l}(u_{m,i} - u_{c,i})^2} \tag{24}$$

where $u_{m,i} = U_{m,i} - U_{ref}$ and $u_{c,i}$ is the calculated disturbance velocity component at i^{th} control point. 'l' denotes the number of control points. The rms error was similarly defined for the normal velocity and the resultant velocity from the side-wall pressure.

4.4.3 Effect of the Side-Wall Boundary Layers

Side-wall pressure measurements were used to compute the corresponding resultant velocity distributions at the control levels. The presence of the side-wall boundary layers was found to have negligible effect on the velocity calculations during the test section calibration. The maximum variation in the Mach number measured upstream and downstream of the test section was ± 0.002 at $M = 0.84$ and ± 0.001 or less at lower Mach numbers. These values translate to a variation of ± 0.5 m/s or less in the velocity calculations in the Mach number range of the present experiments. At $M = 0.7$, velocity measurements taken by the LDV system at the far-field control points upstream and downstream of the model showed a deviation of ~ 1.0 m/s which was found to be in agreement with the side-wall pressure measurements.

Since the present slotted adaptive-wall tunnel has a different test section arrangement (plenum compartments, suction and blowing), previous studies on the boundary layer growth and its effects on the wind tunnel walls in conventional slotted-wall wind tunnels, were not used. However, as explained in the previous paragraph, calibration data did not show any unusual flow behavior in the test section.

4.5 Calibration of the Wind Tunnel

The relationship between the test section Mach number and the flexible throat height was established by calibration. The test section Mach number was set approximately using this calibration, however, precise Mach number adjustments were made in accordance with the pressure measurements.

The calibration of the test section was carried out at different Mach numbers without the model and with all the plenum valves closed. Centerline Mach number distributions along the test section were obtained from pressure measurements on the side-wall. In Figure 4.6, the distributions are shown for $M = 0.3$ to $M = 1.0$. Flow develops smoothly in the convergent nozzle at the entrance of the test section. Downstream, the cross-sectional area of the test section grows slightly to accommodate the boundary layer growth. However, at $M = 0.98$, this viscous effect dominates and the flow chokes before the downstream throat.

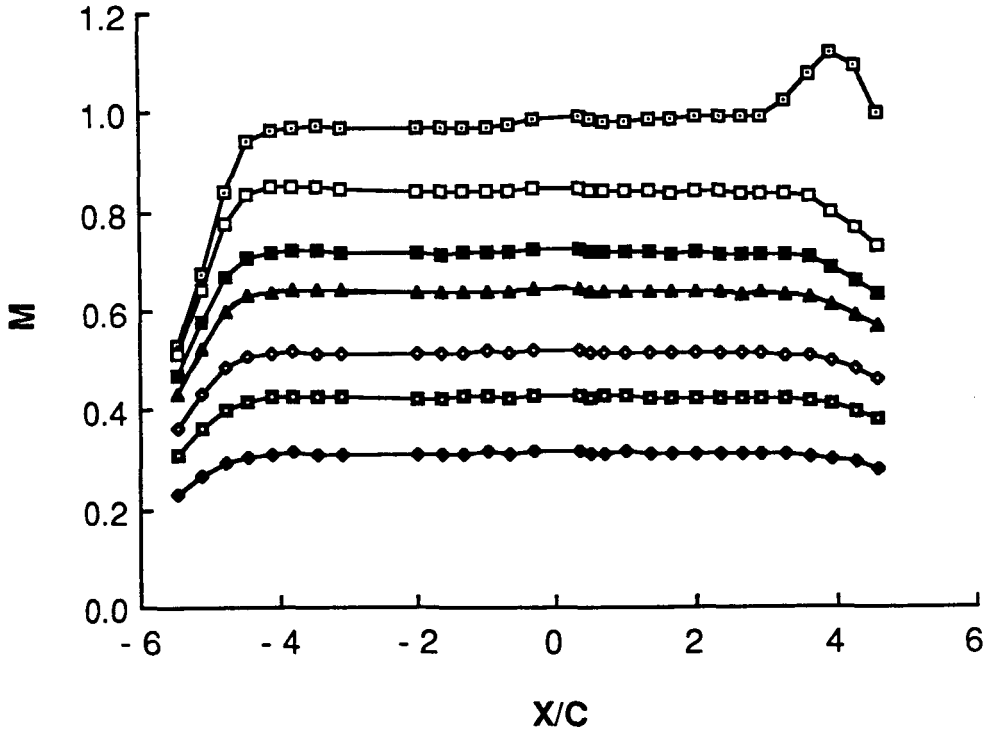

Figure 4.6: Centerline Mach number distribution.

The test section Mach number distribution in the axial direction was determined between $X/C = -3.0$ and $X/C = 3.0$. Up to $M = 0.85$, the standard deviation from the mean is less than or equal to ± 0.003 and it is a reasonably accurate reference value. Figure 4.7 shows the test section Mach number distribution along the axial direction. Variation of the Mach number distribution in the vertical direction was also investigated at various locations upstream and downstream of the model location. Typical distributions obtained at two different x-locations are shown in Figure 4.8.

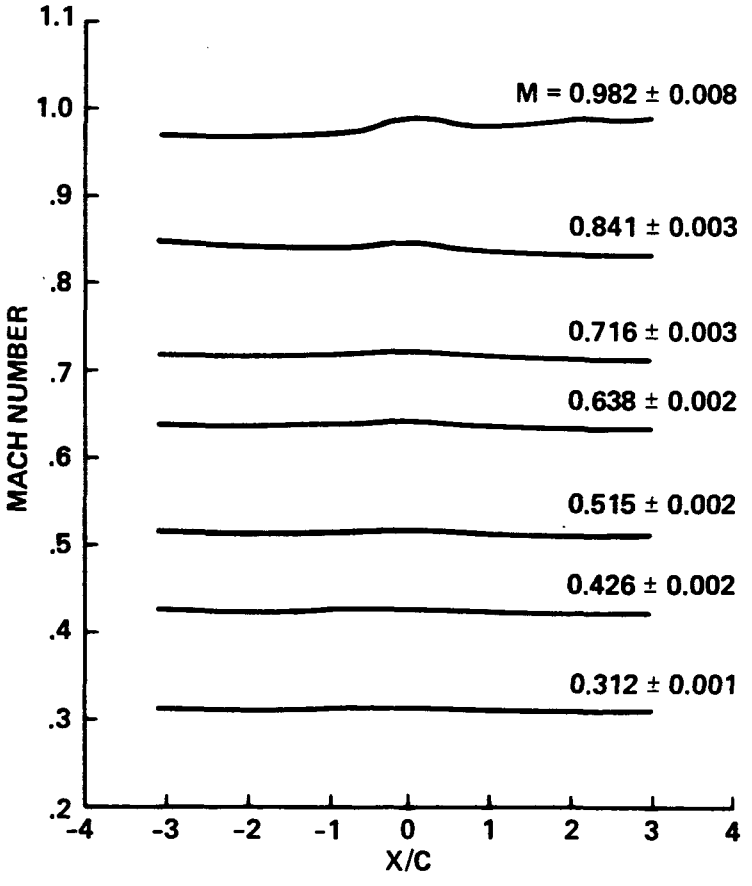

Figure 4.7: Test section Mach number distribution in axial direction.

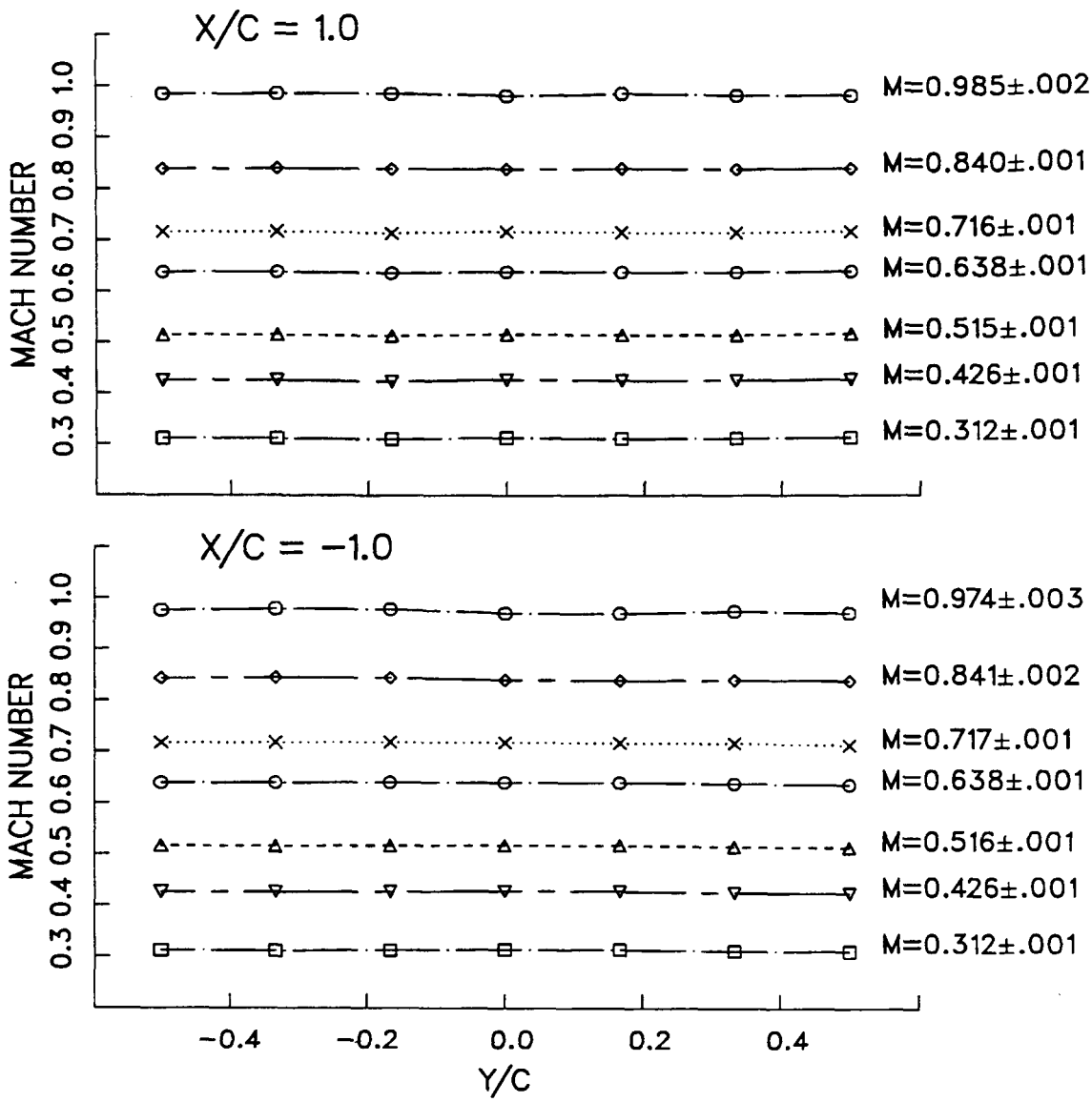

Figure 4.8: Test section Mach number distribution in vertical direction.

The streamwise gradients in the Mach number distribution can easily be eliminated by proper blowing or suction. As shown, a reasonably good distribution was obtained up to $M = 1.0$ in the empty test section. At freestream Mach numbers above 0.98, the shock moved forward into the test section and operation of the downstream throat became ineffective. Further tests done with the model in place showed that a maximum Mach number of 0.75 could be reached with the throat choked. Higher throat openings did not produce any change once this maximum

value was reached.

If the entrance length is not long enough, it is always hard to determine the test section Mach number in the presence of the model. In order to overcome this difficulty, the pressure in the plenum compartment 1 was chosen as the reference to determine the freestream properties. The plenum calibration procedure is considered as a standard method of defining the test section Mach number by relating the plenum pressure to an average test section centerline Mach number. The relationship between the test section Mach number and the Mach number corresponding to the state in the first plenum was determined. Because of the size and the location of this compartment, it was thought to be a reasonable choice to determine the freestream velocity and Mach number for the adaptive-wall experiments. In the presence of the model, velocity measurements taken upstream of the model were compared with this reference for calibration. In Figure 4.9, freestream velocity and Mach number calibration curves are given for the reference plenum compartments.

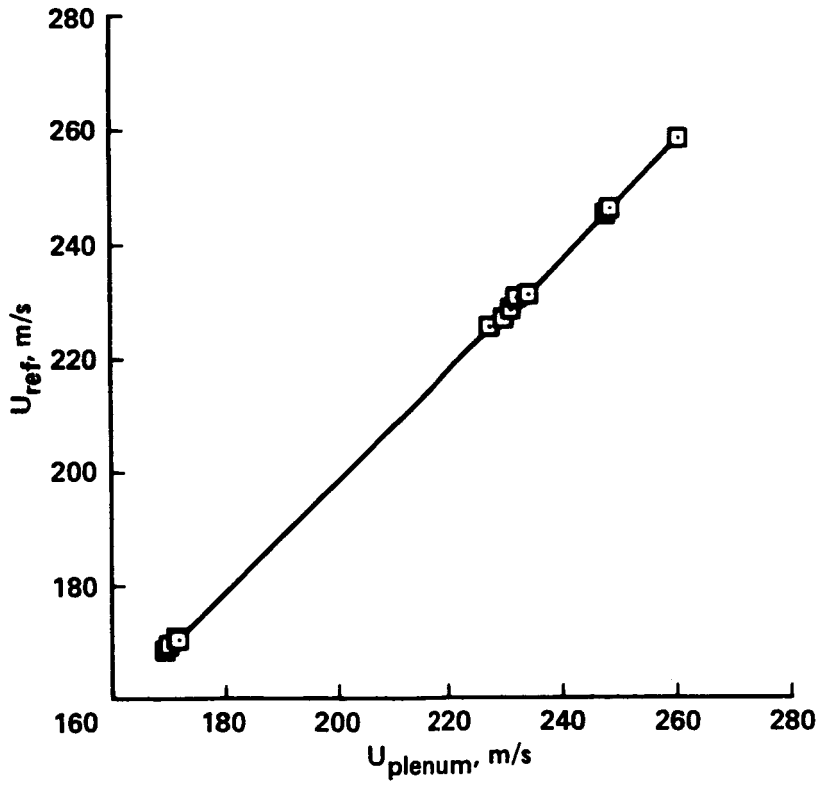

Figure 4.9: Calibration curve for freestream velocity.

Chapter 5

Experiments

Adaptive-wall experiments were carried out in two phases. First, influence coefficients were evaluated systematically for different flow variables and Mach numbers. In the present study, evaluation of the influence coefficients for application to the convergence schemes is very crucial to accurately determine the plenum pressure corrections.

In the application of the convergence schemes, emphasis was given to those using the streamwise velocity component and the resultant velocity from side-wall pressure measurements. Experimental studies with the normal disturbance velocity component were completed in a similar test section[9].

In these experiments, the minimum spacing for the plenum compartments was over the model, a region where the velocity gradients are high. Eight out of ten plenum compartments were used. The first plenum compartment was chosen as the reference plenum for the freestream values and the last plenum compartment was shown to be ineffective for control of the flow.

Velocity measurements were taken at the centerline of the test section along the streamwise direction. When the LDV system was used, the side-wall with the static pressure tappings was replaced by a clear side-wall. The number of control points and their locations were the same as those used in the side-wall pressure measurements. Measurement of the velocity components at the control points by the LDV system consumed most of the available time.

5.1 Evaluation of the Influence Coefficients

Experiments for the evaluation of the influence coefficients were carried out in two parts. In the first part, the static pressure distributions at the control levels were measured by a number of pressure tappings located on one of the side-walls. The maximum number of control points at each level was 18 although the influence coefficients were evaluated at 15 points. In the second part, using the LDV system, streamwise and normal velocity components were measured at 8 points at each control level to determine the influence coefficients. Because of time limitations, the number of control points was kept at the minimum. Velocities at the intermediate points were calculated by cubic spline interpolation. To determine the effects of model and Mach number, measurements were taken with and without the model and at different Mach numbers. Model angle of attack was kept nominally at zero degree. The test conditions are summarized in Table 1.

Side-wall pressure measurements without model			
M	**0.5**	**0.7**	**0.8**
Test Condition	Plenums from 1 to 10; Plenums 4 and 6 comb. Top and bottom pl. 6	Plenums 4 and 6, Plenums 4 and 6 combined	Plenums 4 and 6, Plenums 4 and 6 combined
Side-wall pressure measurements with model, α=0 deg			
M	**0.5**	**0.685**	**0.75**
Test Condition	Plenums 4 and 6, Plenums 4 and 6 combined	Plenums 4 and 6, Plenums 4 and 6 comb. Top and bottom pl. 6	Plenums 4 and 6, Plenums 4 and 6 combined
LDV measurements without model			
M	**0.5**	**0.7**	
Test Condition	Plenums from 2 to 9; Plenums 4 and 6 combined	Plenums 4,6,8; Plenums 4 and 6 combined	
LDV measurements with model, α=0 deg			
M	**0.5**	**0.7**	
Test Condition	Plenums from 2 to 9; Plenums 4 and 6 combined	Plenums 4,6,8; Plenums 4 and 6 combined	

Table 1: Test conditions in the experiments for the evaluation of the influence coefficients.

5.1.1 Effect of Suction and Blowing

Resultant velocity distributions at the control levels were calculated from side-wall pressure distributions using compressible flow relations (Chapter 4). Streamwise and normal velocity components were measured using the LDV system described in the previous chapter. Experiments showed that the disturbance velocity distribution at the control levels could be altered significantly by varying the local plenum pressures.

In Figure 5.1a , the change in the normal velocity distribution at level 2 is shown when different suction and blowing pressures were applied in plenum 4 at $M = 0.5$ without the model. In the presence of the nonlifting model, the normal velocity distribution at level 2 is altered by suction and blowing in plenum 7 as presented in Figure 5.1b. For the normal velocity component, the maximum changes were produced at control points immediately below the active plenum compartment. Suction and blowing produce velocity components toward and away from the wall, respectively.

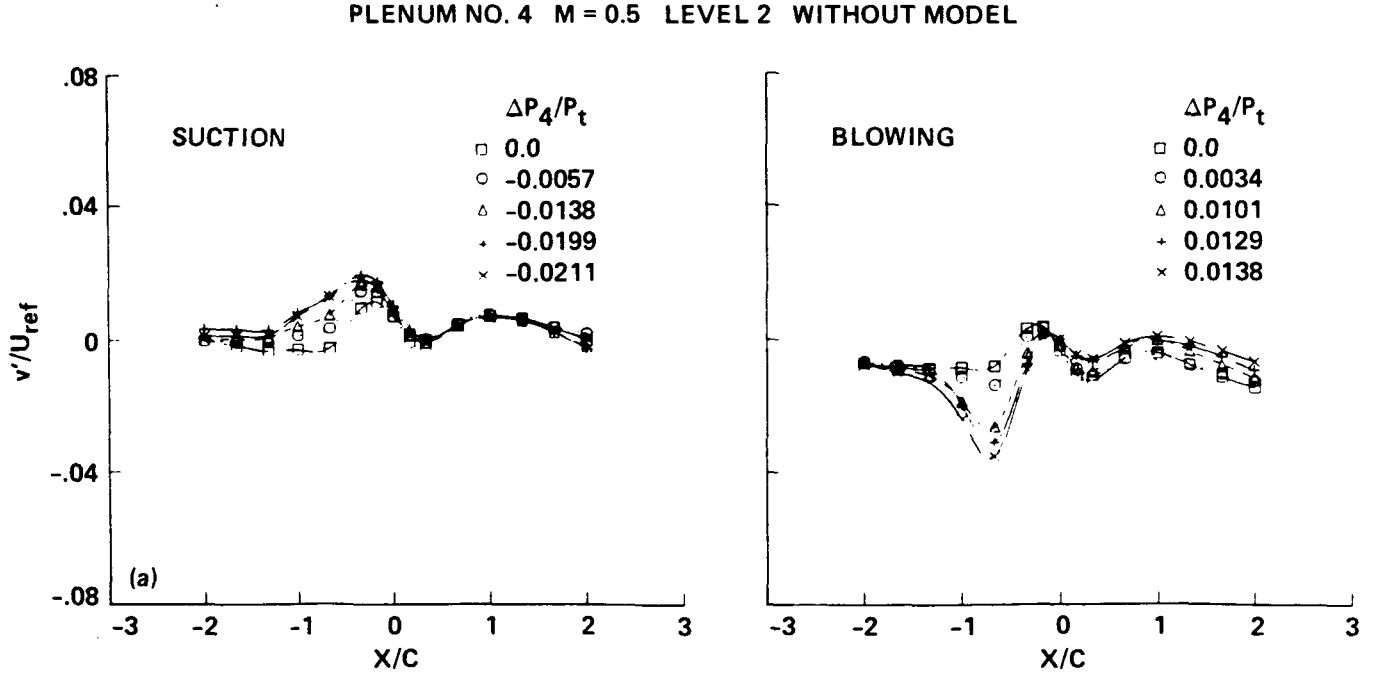

Figure 5.1a: Variation of the normal disturbance velocity distribution with suction and blowing.

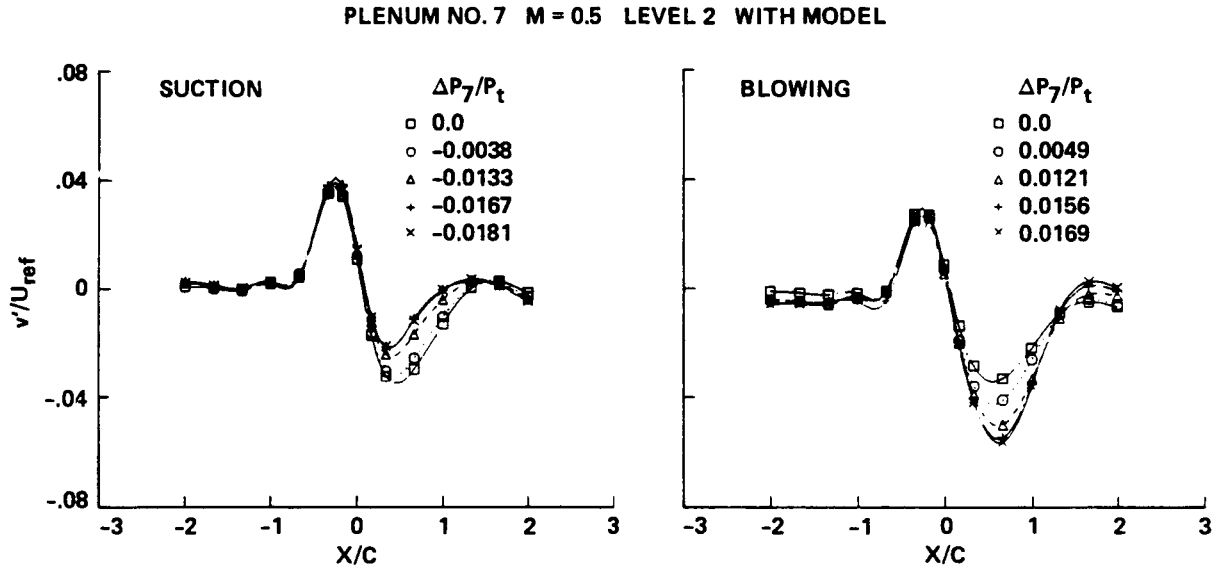

Figure 5.1b: Variation of the normal disturbance velocity distribution with suction and blowing.

Compared to the normal velocity component, a completely different velocity distribution was observed for resultant and streamwise velocities. As illustrated in Figure 5.2a, the effect of plenum 4 on the streamwise disturbance velocity at points upstream of that plenum is negligible compared to downstream points. In Figure 5.2b, the disturbance in resultant velocity distribution at level 2 shows the same behavior at a different Mach number when suction and blowing are applied in plenum 4. The same trend is observed for plenum 6 in the presence of a model and at a different Mach number as shown in Figure 5.2c. The effect of suction is to produce a negative disturbance velocity while blowing produces a positive disturbance. Figure 5.3 illustrates the behavior of the influence coefficients for the resultant velocity at various control points along levels 1 and 2 for plenum 4 at $M = 0.5$.

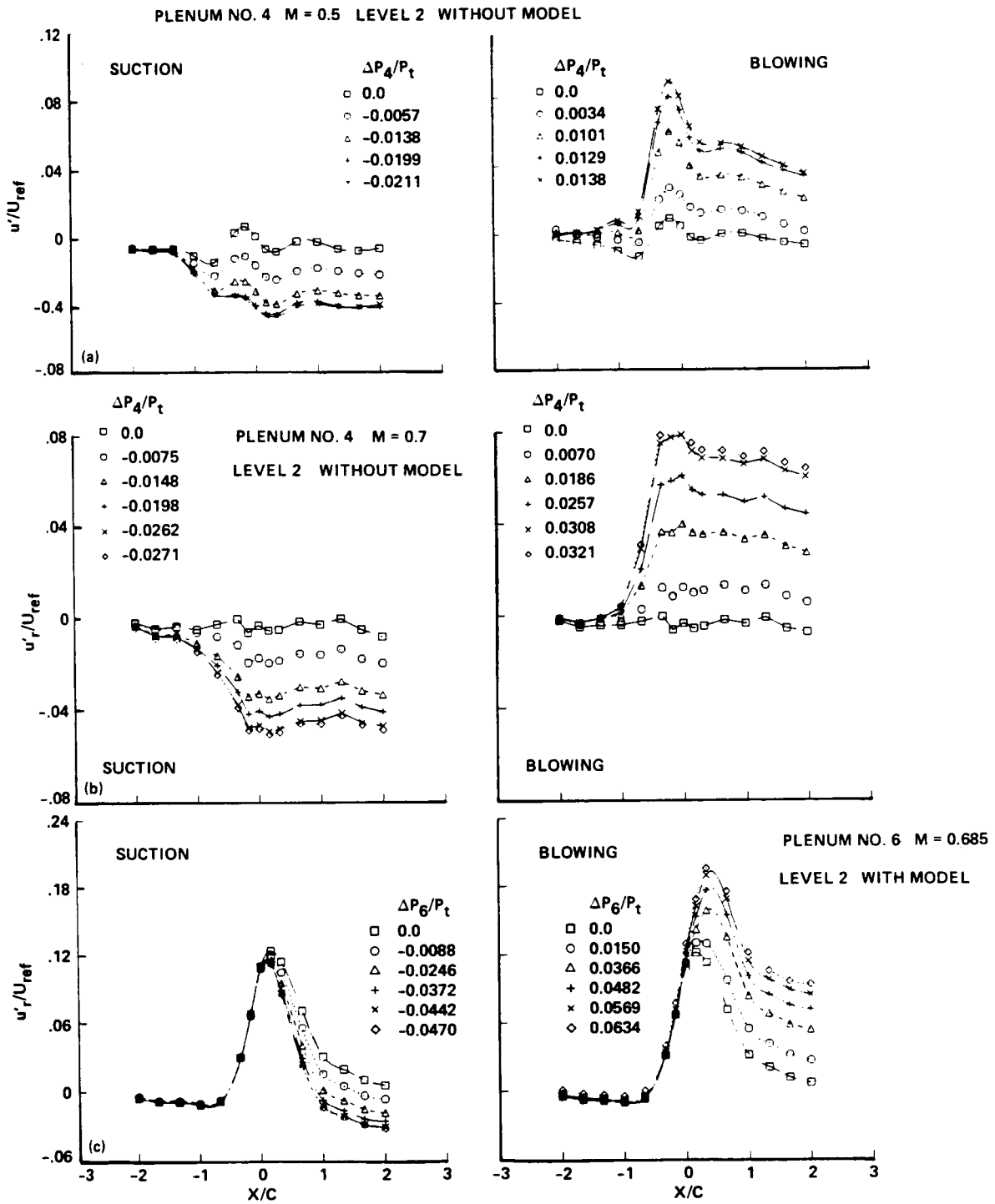

Figure 5.2: Variation of the streamwise and resultant velocity distributions with suction and blowing.

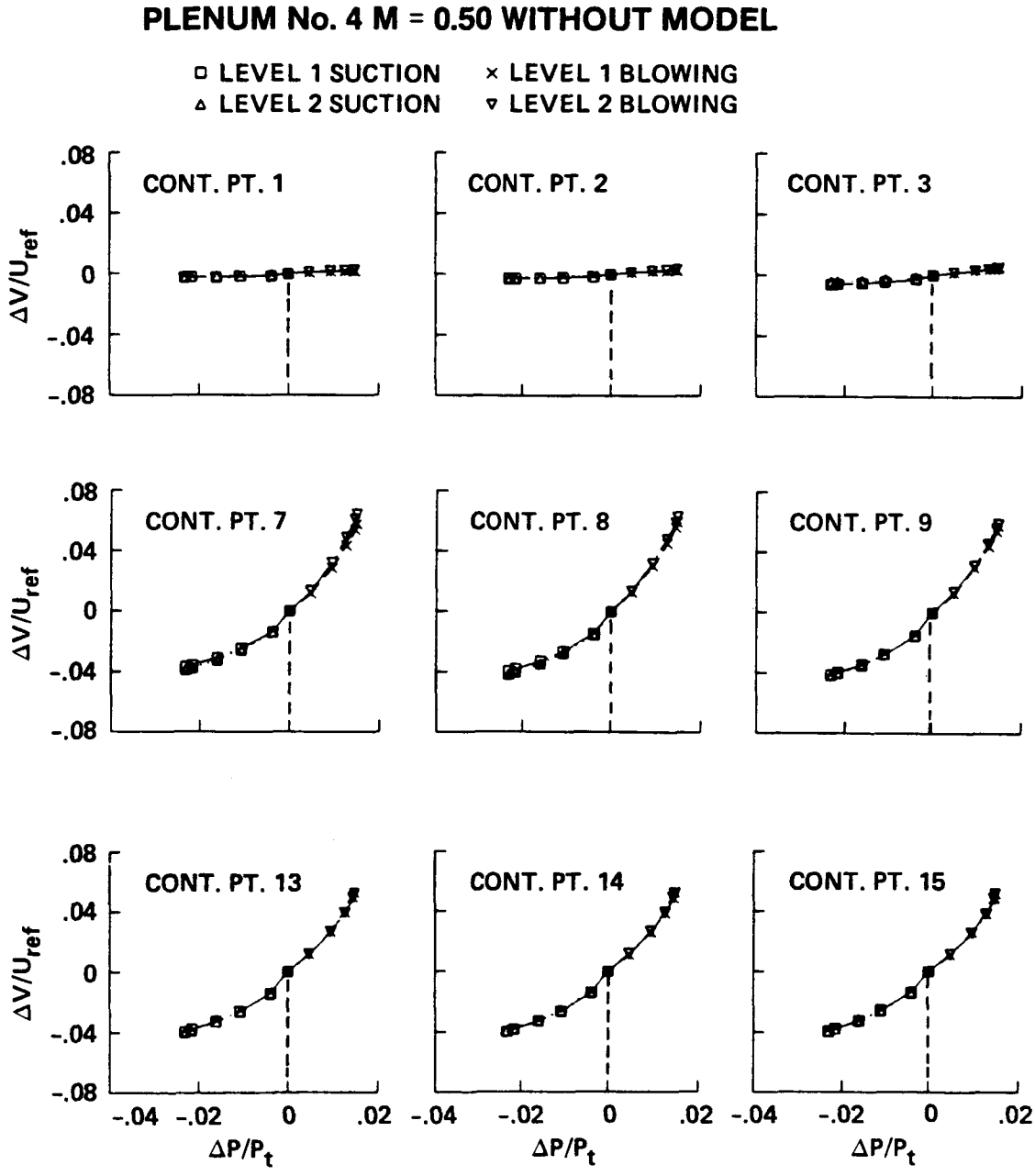

Figure 5.3: Influence coefficients at various control points for resultant velocity.

5.1.2 Effect of Mach Number

In general, the dependence of the influence coefficients upon the Mach number and presence of the model is as expected. The effects of Mach number and model on the influence coefficients are crucial for practical applications. The degree of dependence and the limitations should be carefully explored.

The effect of Mach number on an influence coefficient at control point 12 when suction and blowing is applied into plenum 4, is illustrated in Figure 5.4a. Velocities were calculated from side-wall pressure distributions which were measured in the presence of the nonlifting model at different Mach numbers. For blowing, the influence coefficients change very little with Mach number. However, differences are observed in the suction case. The effect of plenum 4 is negligible at upstream control points for the Mach number range of interest.

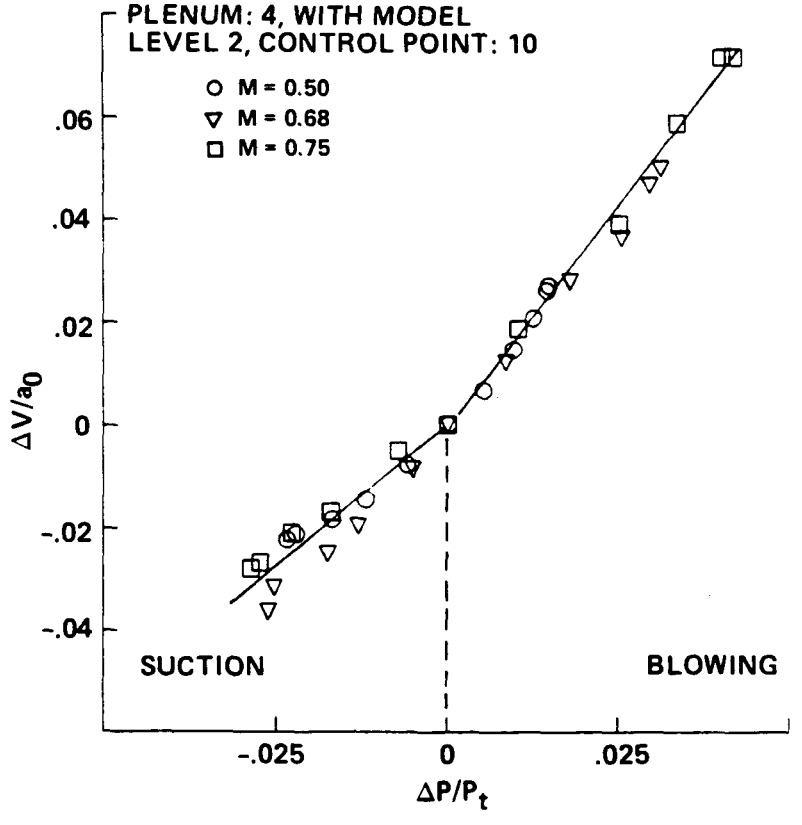

Figure 5.4a: Effect of Mach number on the influence coefficients evaluated from side-wall pressure distribution.

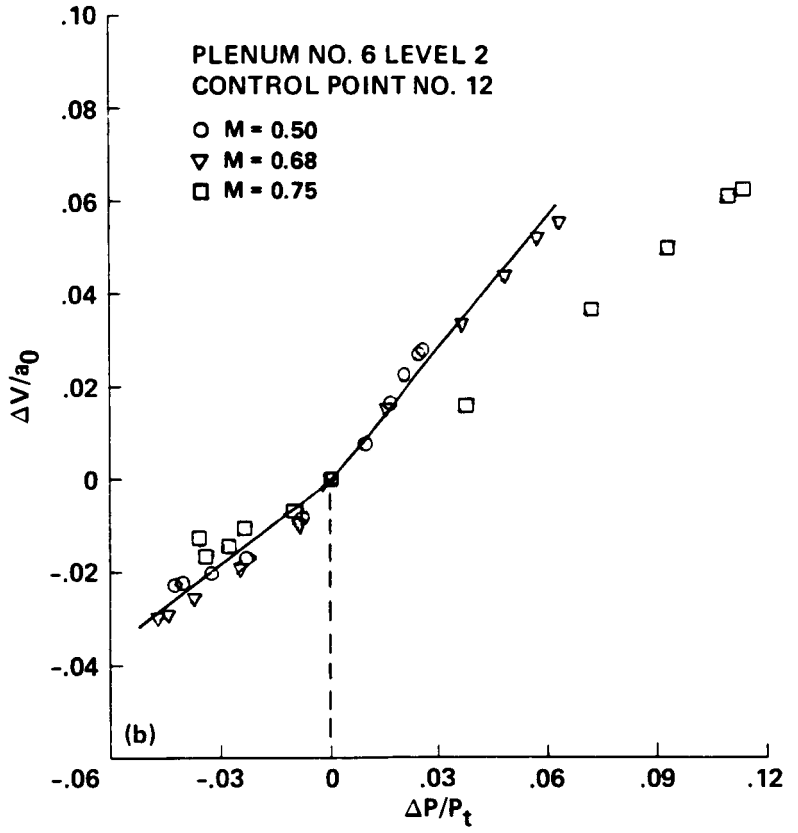

Figure 5.4b: Effect of Mach number on the influence coefficients evaluated from side-wall pressure distribution.

Figure 5.4b illustrates the effect of Mach number at control point 12 for plenum 6 with the model present. At $M = 0.75$, the influence coefficient shows a clear departure from the others in the blowing case. The location of plenum 6, which is directly above the model, suggests that blowing may contribute to a shock wave interaction which causes this discrepancy. In Figure 5.4a, this anomaly was not observed for plenum 4, which is located upstream of the model.

Figure 5.5a shows the influence coefficients with the model present evaluated from the normal velocity distribution at control point 5 which is right below plenum 4. Figure 5.5b shows influence coefficients for the streamwise component without the model created by about the same blowing and suction. The effect of Mach number is negligible for both velocity components.

The differences at some points on the same curve are of the order of 1 m/s which is about the accuracy of the LDV measurements. Velocity measurements with LDV are very sensitive to alignment errors and non-uniformities in the plexiglass sidewalls.

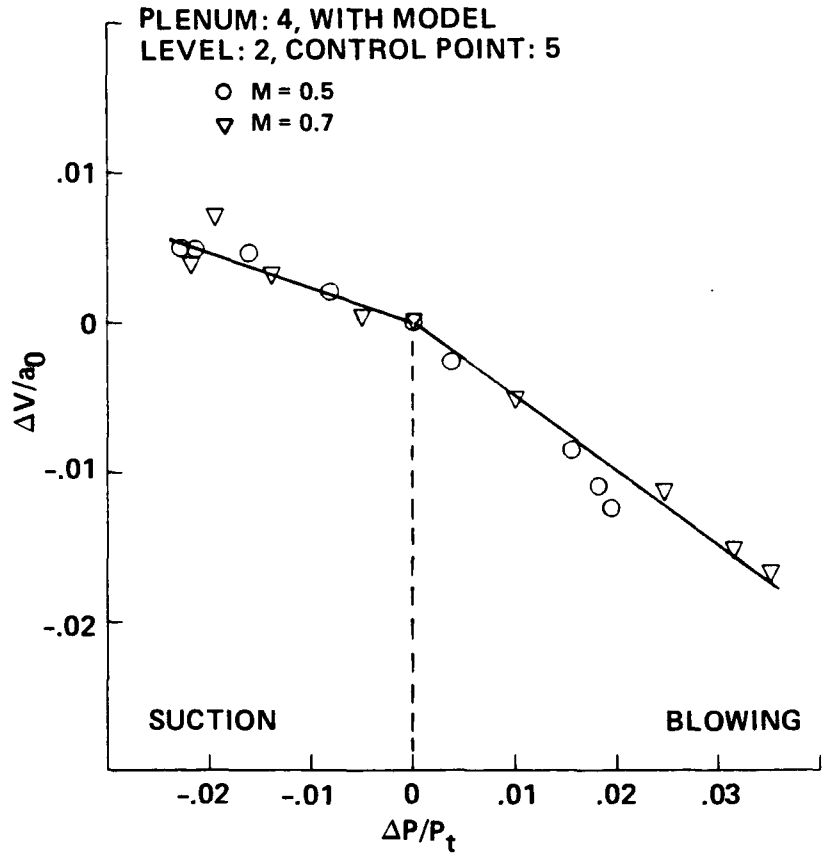

Figure 5.5a: Effect of Mach number on the influence coefficients evaluated from normal velocity distribution.

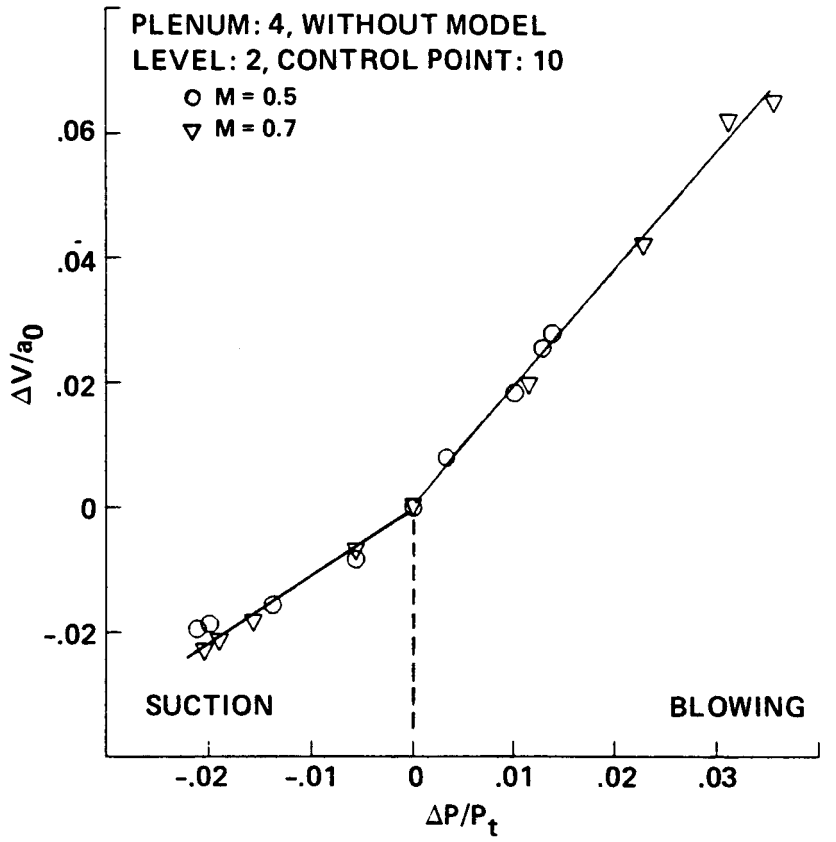

Figure 5.5b: Effect of Mach number on the influence coefficients evaluated from streamwise velocity distribution.

5.1.3 Effect of Model

Another important aspect for the influence coefficients which should be explored carefully, is the effect of the model. If they are dependent on the type of model to be tested, the tedious and costly determination of the influence coefficients has to repeated for different models. The same argument is also valid for the Mach number effects.

Effects of the presence of a nonlifting model are presented showing the resultant velocity component at different Mach numbers in Figure 5.6. The effect of the model is negligible although slight differences are observed for suction. Piecewise linear approximation for suction and blowing agrees with the data. Since all the experiments were conducted at zero angle of attack, the effect of a lifting model

remains unknown. But, it is expected that influence coefficient matrices obtained at zero angle of attack would give a fairly good estimate for the pressure corrections at small angles of incidence.

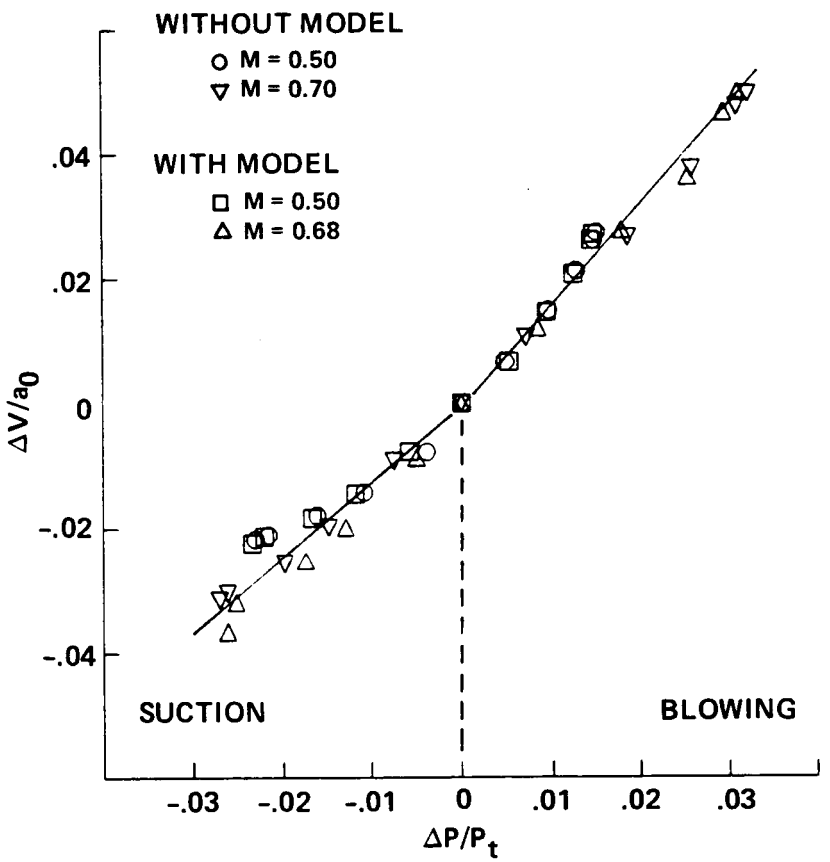

Figure 5.6: Effect of a nonlifting model on influence coefficients evaluated from side-wall pressure distribution.

5.1.4 Superposition

The velocity change produced at any control point due to the pressure changes in more than one plenum was assumed to be equivalent to the sum of the velocity changes produced at that point by the same pressure changes in each plenum, if applied separately. A check of this assumption of superposition is given in Figure 5.7. In this case, blowing is applied to plenum 4 and 6, first separately and then together. The velocity distribution for the combined plena, which was calculated from side-wall pressure measurements, is compared to the superposed result. There is reasonable agreement although there are differences greater than 1 m/s at some points. These differences are attributed to the slight differences in freestream conditions and interpolation errors.

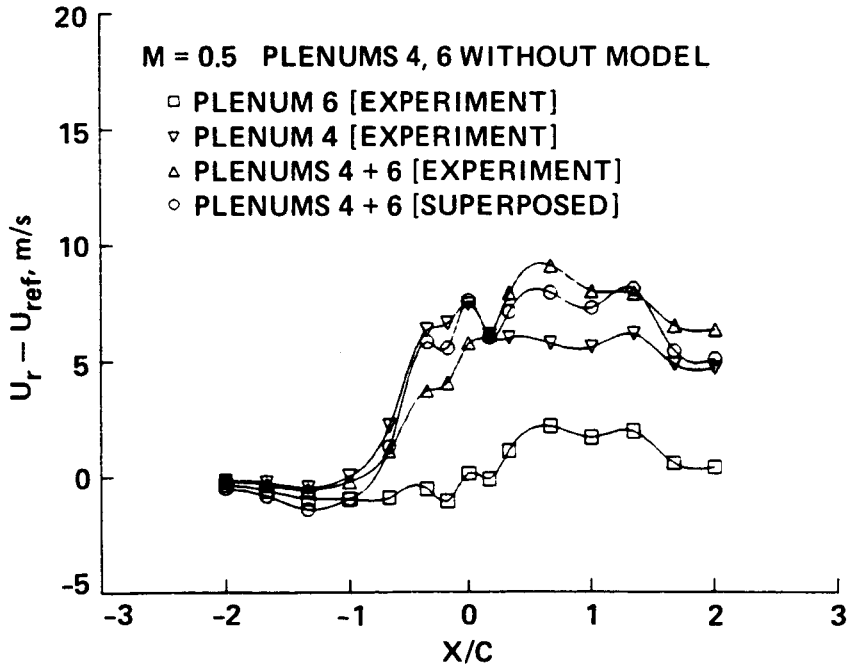

Figure 5.7: Superposition check for two plenum compartments for resultant velocity.

In Figure 5.8a , another superposition check using resultant velocity is presented. In this case, top and bottom plenum 6 are treated separately. Suction and blowing were first applied into the top plenum compartment. The same procedure was repeated for the bottom plenum while the others were kept closed. Influence coefficients at control point 12 were calculated for each case and superposed to compare with those obtained when top and bottom plenum 6 were controlled together.

Additional tests were performed to investigate the superposition in the presence of the model and at a higher Mach number. Influence coefficients at two control points upstream and downstream of plenum 6 were measured and superposed using the same procedure outlined in the previous paragraph. Figures 5.8a and 5.8b illustrate that superposition for resultant velocity at a downstream control point is within the limits of the experimental error. Similar results were obtained at the upstream points as shown in Figure 5.8c.

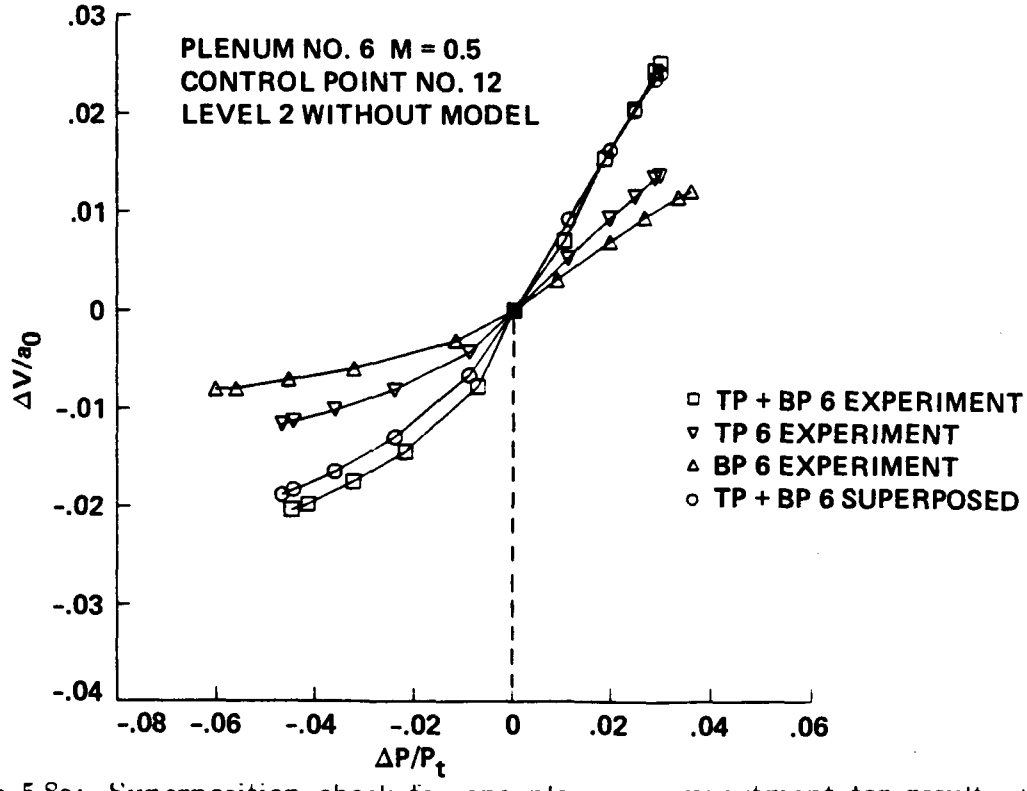

Figure 5.8a: Superposition check for one plenum compartment for resultant velocity at M=0.5.

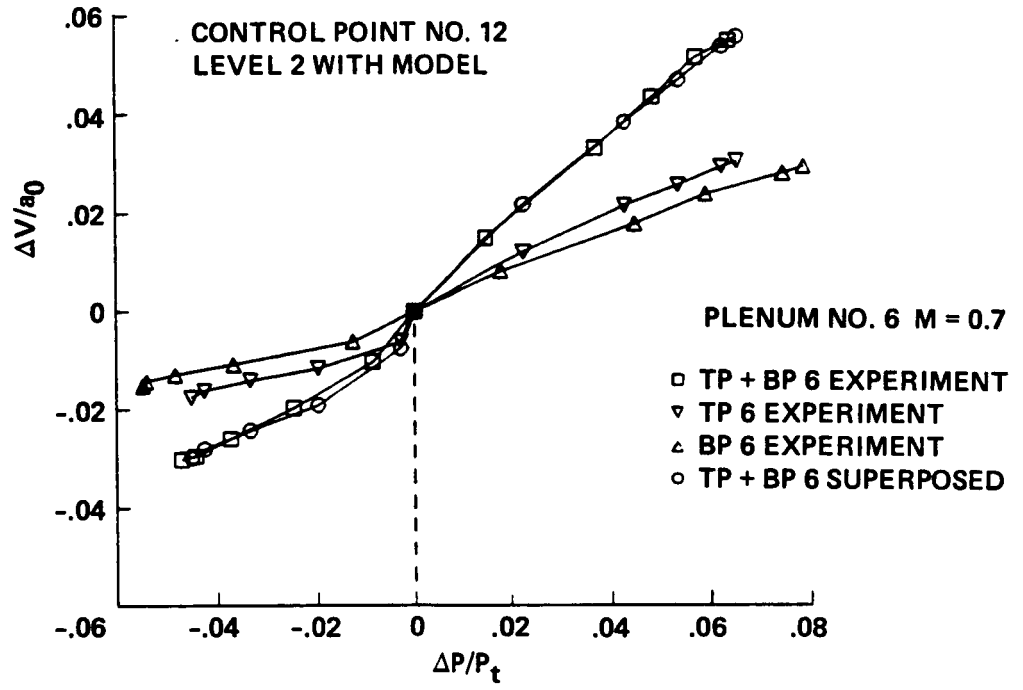

Figure 5.8b: Superposition check for one plenum compartment for resultant velocity at M=0.7.

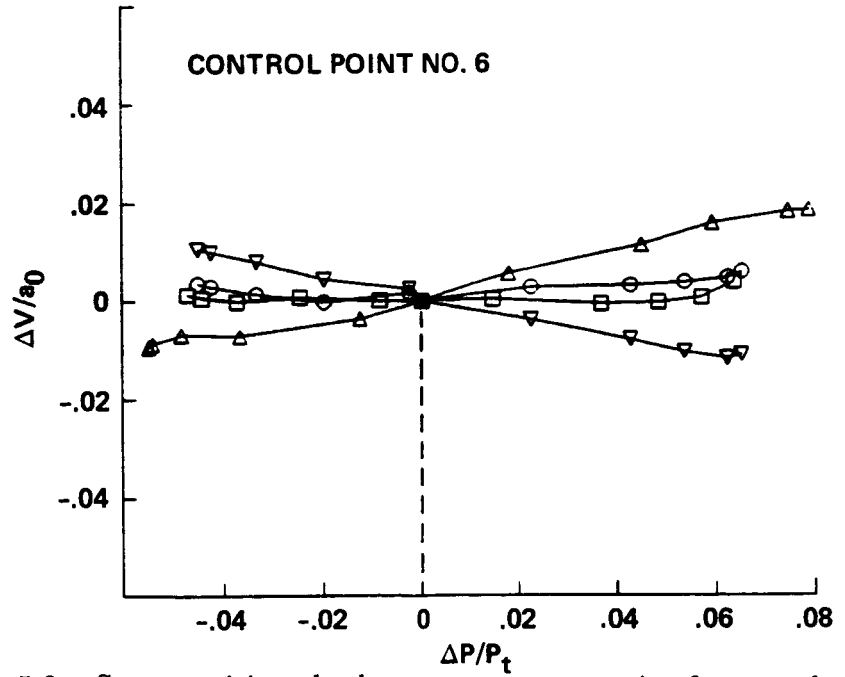

Figure 5.8c: Superposition check at an upstream point for one plenum compartment at M=0.7.

5.1.5 Linearity

Over the Mach number range of interest, the influence coefficients are well approximated as linear for blowing at high Mach numbers. For suction, nonlinearity is clearly observed at low Mach numbers (Figures 5.5b, 5.6 and 5.8a). As the Mach number increases, the linear approximation gets better for both suction and blowing (Figures 5.5a, 5.5b, and 5.6). In the present study, elements of the influence coefficient matrices were approximated as piecewise linear for both suction and blowing. Since suction and blowing created different effects, two separate sets of influence coefficients were used in the construction of the influence coefficient matrices. In the present study, the effects of the nonlinear coefficients were not investigated theoretically or experimentally since the linear approximation was found satisfactory for practical applications (See Section 5.2).

5.1.6 Summary

In the application of the convergence schemes, influence coefficient matrices were formed using the equations given in Chapter 2. Influence coefficients were approximated as piecewise linear in the present Mach number range. Complete sets of influence coefficient matrices were formed without the model and at $M = 0.5$ from the side-wall pressure measurements. In the case of LDV measurements, each set of matrices was constructed from influence coefficients obtained in the presence of the nonlifting model and at $M = 0.5$. The best linear fit was found for both suction and blowing at each control point.

The influence coefficients obtained from side-wall pressure distribution are comparable with those from streamwise velocity measurements using LDV. This suggests the possibility of using the same strategy for the unconfined flow calculations. Influence coefficient matrices determined for each flow variable are given in Appendix C.

5.2 Application of the Convergence Schemes

Adaptive-wall experiments were performed at Mach numbers ranging from 0.5 to 0.75 and at angles of attack of $0°, 2°$, and $4°$. A brief summary of the test conditions is given in Table 2.

The tunnel running time available for iterations was limited by the ejector which could operate continuously for only about 40 minutes at the maximum setting. At the end of each cycle, the wind tunnel was shut down so that the storage tank which drives the ejector, could be pressurized. The existing auxiliary system provided insufficient suction and blowing of air for complete control of the flow at high Mach numbers.

Experiments with the LDV system were conducted at freestream Mach numbers up to $M = 0.7$; data quality at higher speeds was affected by condensation effects.

In adaptive-wall experiments with the ventilated-wall tunnel, the test section Mach number varies when suction and blowing are applied in the plenum compartments. During the experimental iterative process, after each iteration, the test section Mach number was adjusted back approximately to its initial value. In the one-step method, a first-order correction, deduced from calibration tests, was applied to simulate this change in the test section Mach number.

In this section, results obtained using the one- and two-level compatibility assessment methods with the iterative and the one-step convergence schemes will be presented in three parts. In the first part, typical results are given to establish the feasibility and the validity of the concept using the resultant velocity distribution as a flow variable, as well as to show the applicability of the one-step method with the approximate influence coefficients in a supercritical lifting case. Secondly, the results obtained in a subcritical nonlifting case are presented to compare the one-level and two-level compatibility assessments along with the comparison of the iterative and the one-step methods using the streamwise and the resultant velocity distributions. In the last section, typical results are given to show the applicability and the effectiveness of the influence coefficients in subcritical and supercritical cases at various Mach numbers and model angles of attack.

As mentioned in Chapter 1, the finite number of plenum compartments is one of the major factors influencing the accuracy of adaptive-wall control. In the present study, a maximum eight out of ten plenum compartments were used with the exceptions being the first and the last pairs. Pressure measured at a location close to the middle section in each plenum compartment was assumed to be the plenum pressure in that compartment. In some of the examples, pressure distributions in the top and the bottom plenum compartments are presented for comparison before and after the corrections are applied. In all the applications, there was initially no suction and blowing applied in the plena. After the final iteration, the status of the pressure control is illustrated for each compartment to indicate whether suction or blowing was applied. The size of the plenum compartments is drawn to scale, so that the influence regions can be easily seen. Since any pressure change in one plenum compartment induces changes in the others, pressure changes in plenum compartments 1 and 10 are due to the corrections applied in the rest of them.

Applications with side-wall pressure measurements				
M	**0.5**	**0.55**	**0.6**	**0.65**
α deg	0, 2, 4	0	0, 4	0, 2
Scheme	ite.; one-step	iterative	ite.; one-step	ite.; one-step
M	**0.7**	**0.72**	**0.74**	**0.75**
α deg	0, 2, 4	0	0, 2	0
Scheme	ite.; one-step	ite.; one-step	iterative	iterative

Applications with LDV			
M	**0.5**	**0.65**	**0.70**
α deg	0, 2	2	0, 2
Scheme	ite.; one-step	ite.; one-step	ite.; one-step
Flow Variable	normal and streamwise vel.	streamwise velocity	normal and streamwise vel.

Table 2: Test conditions in the experiments for the application of the convergence methods.

5.2.1 Applications in the Supercritical Lifting Case

Since the adaptive-wall concept has been developed primarily for transonic testing, the approach introduced in this research was first exploited in experiments where the model had a supercritical flow region on its surface. In some cases, nearsonic or transonic flow extended to the control levels before the wall boundary conditions were adjusted using the convergence schemes.

5.2.1.1 Two-Level Iterative Scheme with Streamwise Velocity Distribution

The objective of this particular case was to use the streamwise velocity component as the flow variable in the two-level compatibility assessment and to establish a base for schemes with resultant velocity distribution.

Since normal and streamwise velocity components were measured together, resultant velocity distributions at the control levels could be calculated and experimental steps could be simulated numerically by imposing the resultant "disturbance" velocity distribution, u'_r, as the flow variable. The supercritical lifting case was chosen to find out the error introduced by this assumption, especially in the presence of high velocity gradients, in the flow field about the model.

Initially, while there was no suction and blowing induced by the auxiliary system, velocity components were measured at $M = 0.703$ and $\alpha = 2.°$. The two-level iterative method was applied with the streamwise velocity component only. In Figures 5.9a and 5.10a, experimental and calculated streamwise disturbance velocity distributions are shown at the upper and the lower levels respectively. Evidently, a shock wave penetrates the control levels in the upper half. However, in the lower half, the flow is subcritical and the effect of wall interference is much smaller. After the third iteration, wall interference was reduced substantially in the upper half, achieving a 60 % reduction in the rms error as shown in Figure 5.9b. Below the model, an almost perfect matching of the experimental and unconfined velocity distributions at level 2 was obtained as illustrated in Figure 5.10b.

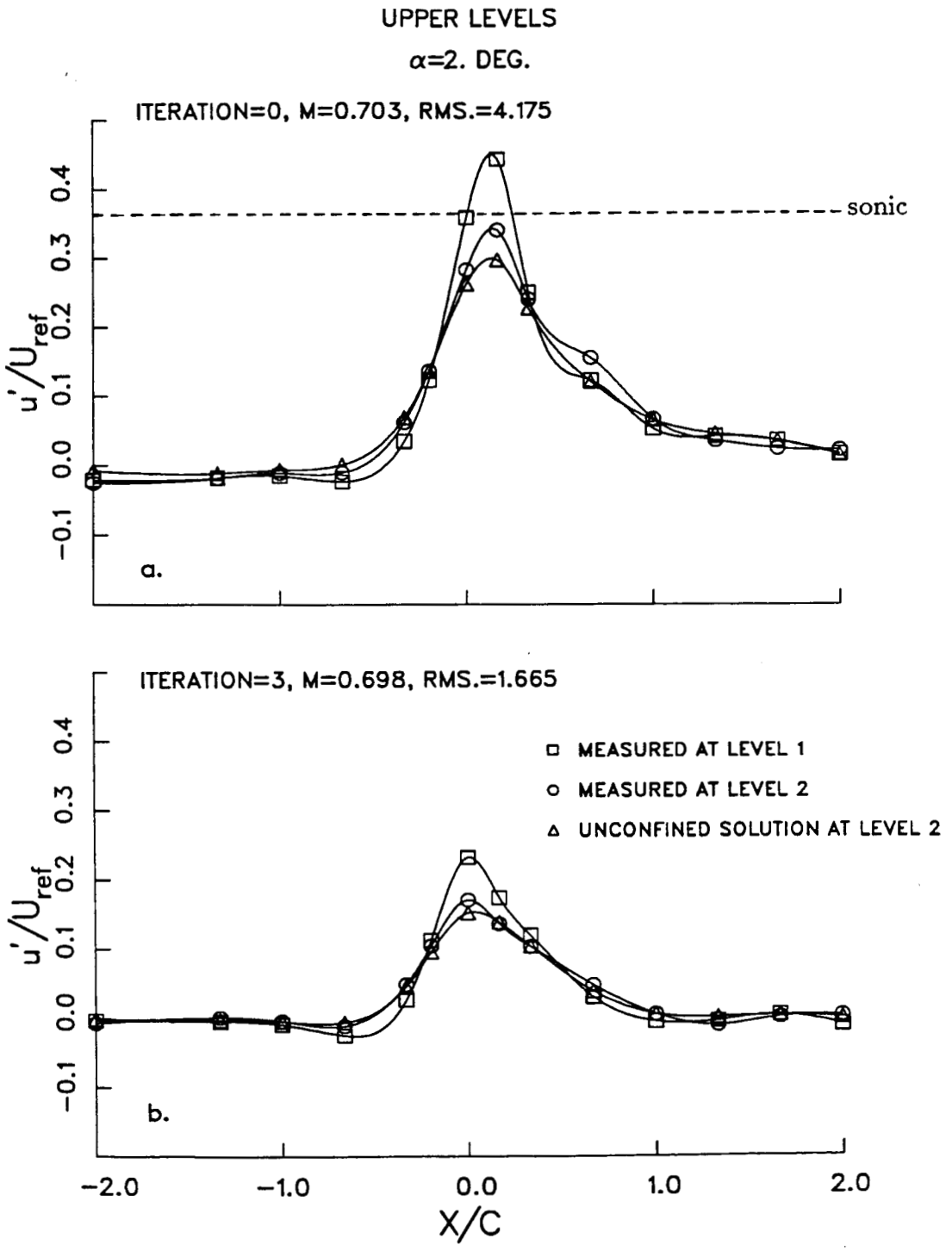

Figure 5.9: Streamwise velocity distribution at the upper levels in the supercritical lifting case, two-level iterative method.

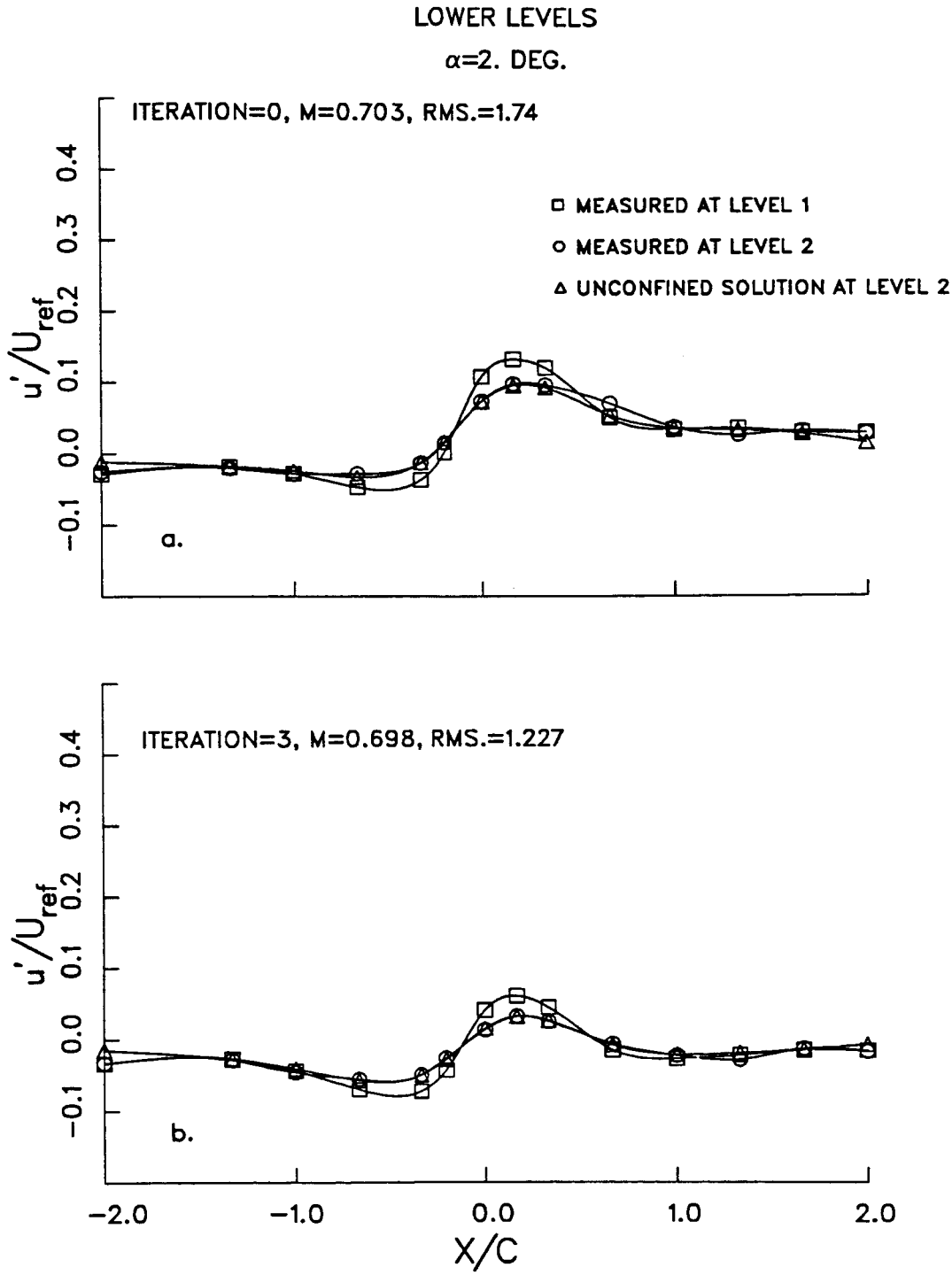

Figure 5.10: Streamwise velocity distribution at the lower levels in the supercritical lifting case, two-level iterative method.

The plenum pressure distributions were substantially different after three iterations compared to the initial case in which no suction and blowing was applied. Figure 5.11 shows the initial and the final pressure distributions of the each plenum. As expected, large pressure changes occurred in the plenum compartments in the vicinity of the model where the matching of the velocity distributions shows a large discrepancy, initially (Figure 5.9).

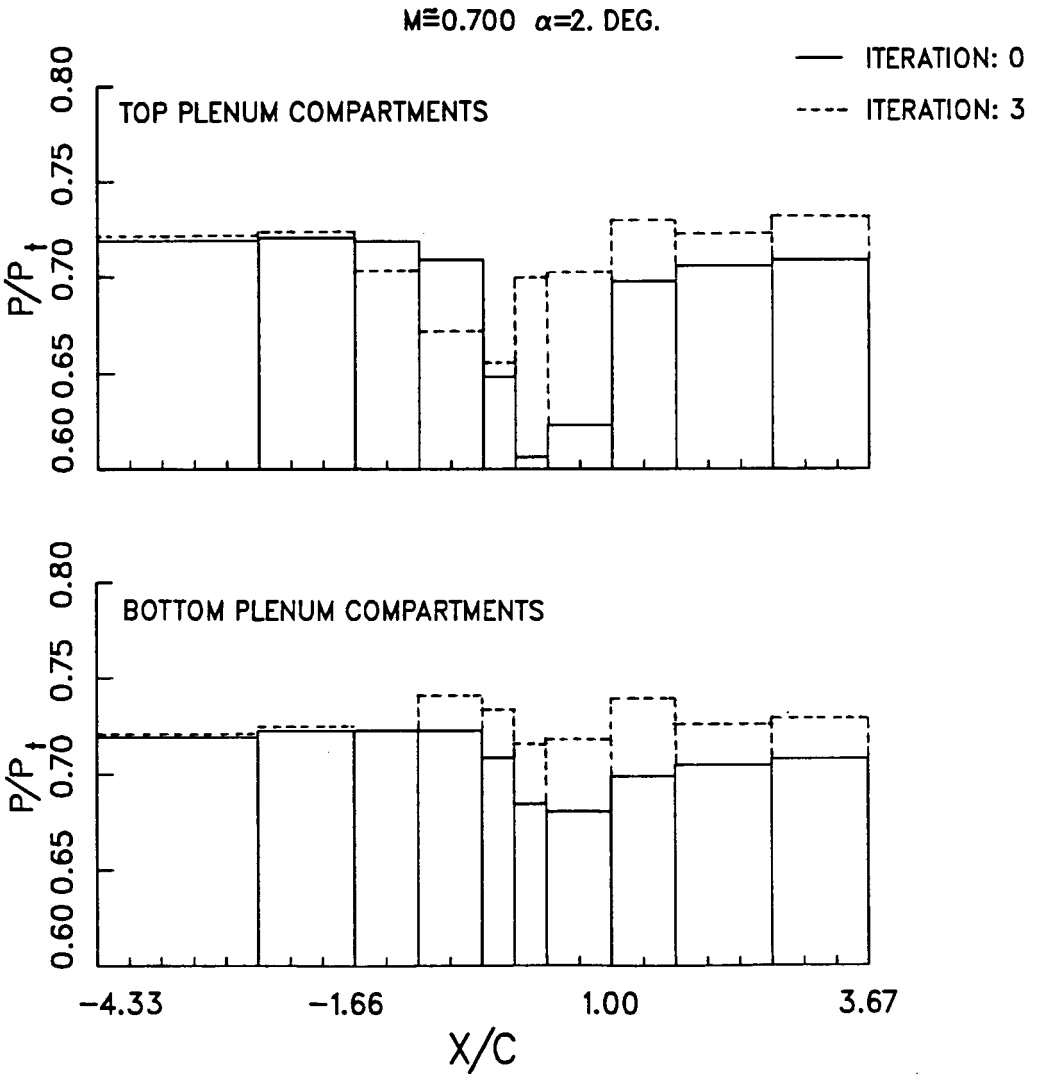

Figure 5.11: Plenum pressure distributions before and after the corrections applied.

The initial and final measured model pressure distributions were compared with the Calspan data[45] in Figure 5.12a. The effect of the wind tunnel wall interference is clearly observed on the model pressure distribution as the higher pressure coefficient and movement of the shock location between the initial and the final adapted cases. The Calspan data was taken in the Calspan eight-foot tunnel at a slightly higher Mach number compared to the present case, but it still provides a good comparison for our purpose. A transition strip used at the ten-percent chord location is believed to have been the cause for the suppression of the Calspan model pressure distribution. The Calspan data shows a local separation at ten-percent of the chord from the leading edge, while the present data also indicates a possible local separation at $x/C \sim 0.20$. The present experiments were conducted at a nominal chord Reynolds number of 10^6 like the Calspan data.

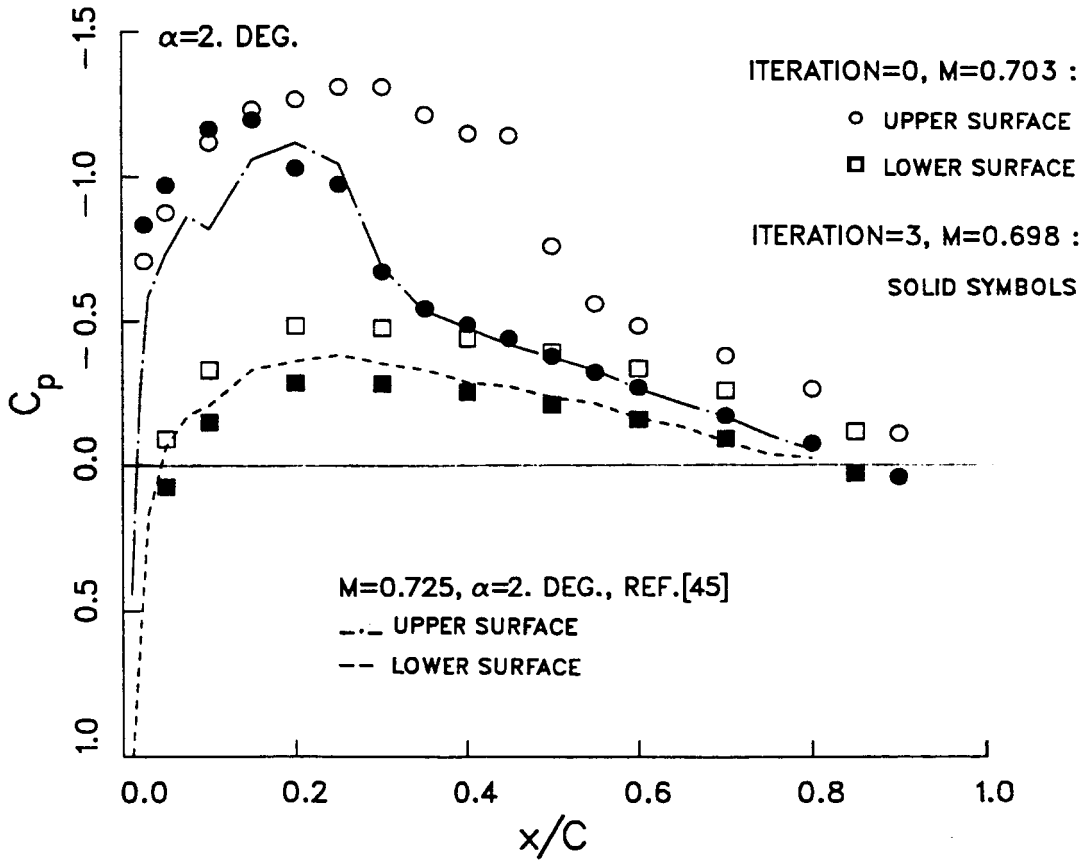

Figure 5.12a: Comparison of the initial and final model pressure distributions with the Calspan data[45].

Comparison of the initial and final model pressure distributions with the numerical solution from TAIR code[47] shows that the shock position is in good agreement after the corrections (Figure 12b). However, the numerical solution predicts a higher pressure coefficient at the leading edge compared to the experimental measurements. This is possibly due to the inviscid formulation used in the numerical code.

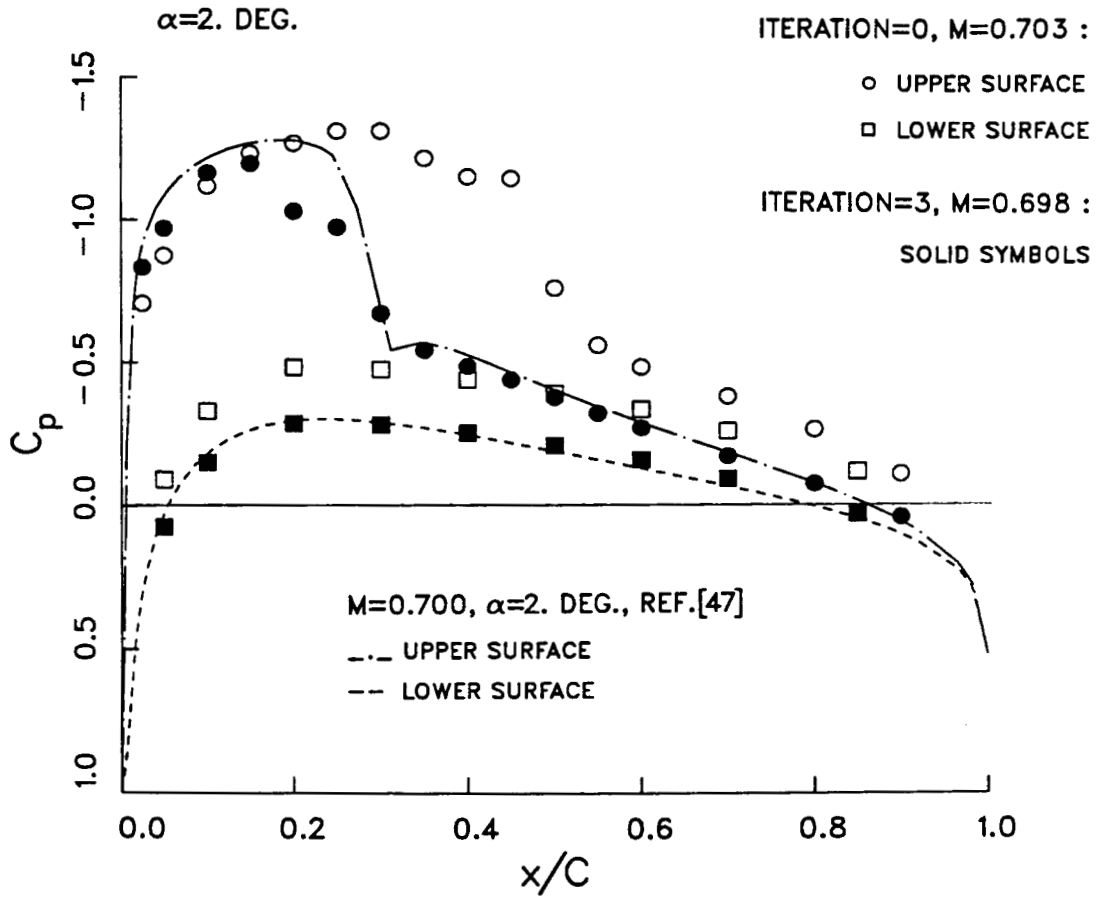

Figure 5.12b: Comparison of the initial and final model pressure distributions with the TAIR solution[47].

Since the normal velocity component was measured along with the streamwise velocity, the changes in the normal disturbance velocity distributions could be compared. Figure 5.13 shows the initial and the final velocity distributions at the upper levels. It is observed that there is a considerable reduction in the rms error.

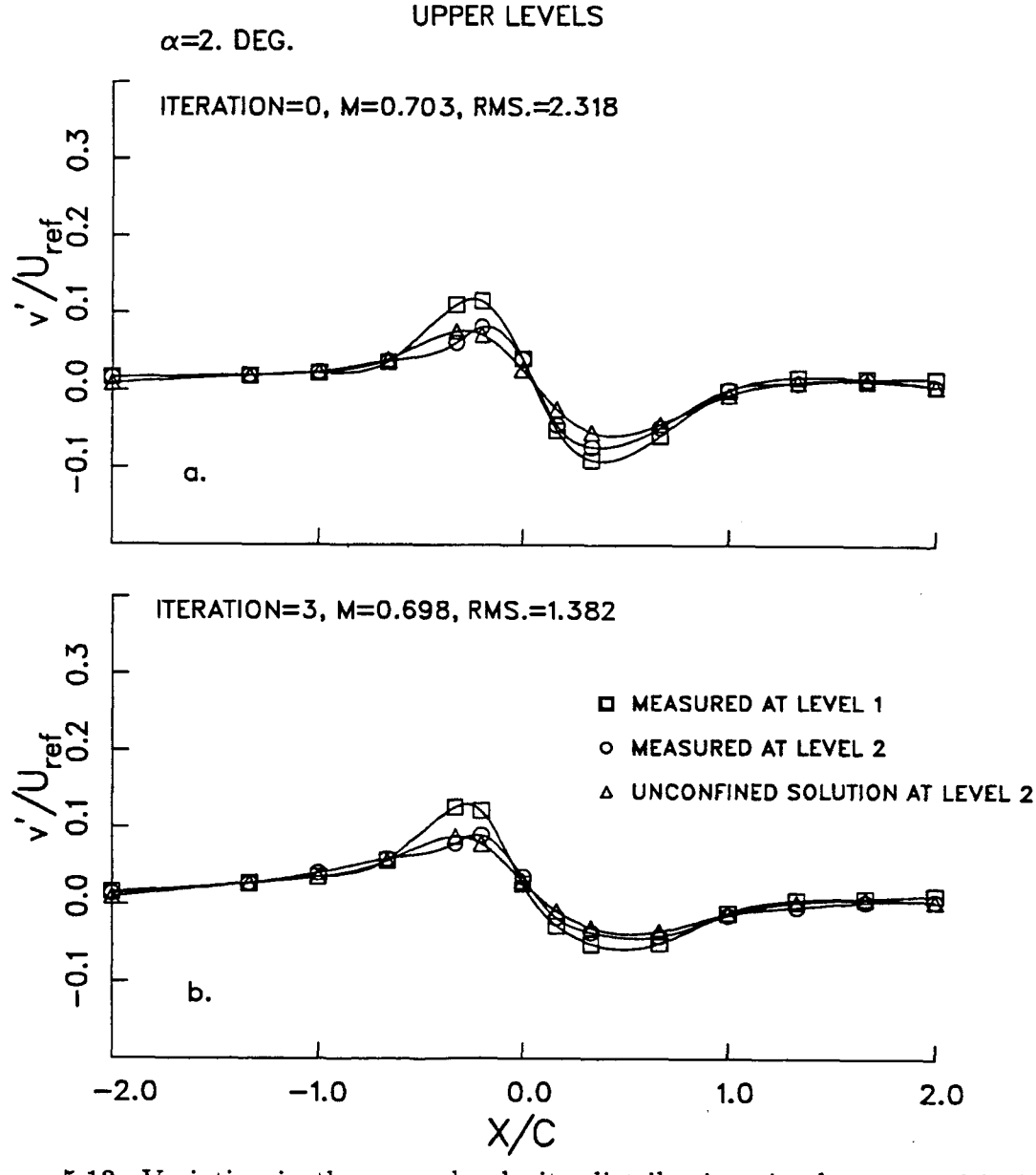

Figure 5.13: Variation in the normal velocity distributions in the supercritical lifting case, two-level iterative method.

The experimental iterations outlined above were reconstructed numerically with the resultant velocity distributions which were obtained combining measured streamwise and normal velocity components. The maximum error was found to be about 1 % when the resultant "disturbance" velocity was assumed to be the streamwise velocity at the control points. Results show that rms errors are slightly lower, about 4 %, compared to the scheme with the streamwise velocity distribution only. Otherwise, no significant differences were observed. The resultant velocity distributions are illustrated in Figures 5.14 and 5.15. By this simulation, it then becomes possible to establish the criteria with which the schemes can utilize the side-wall pressure distributions.

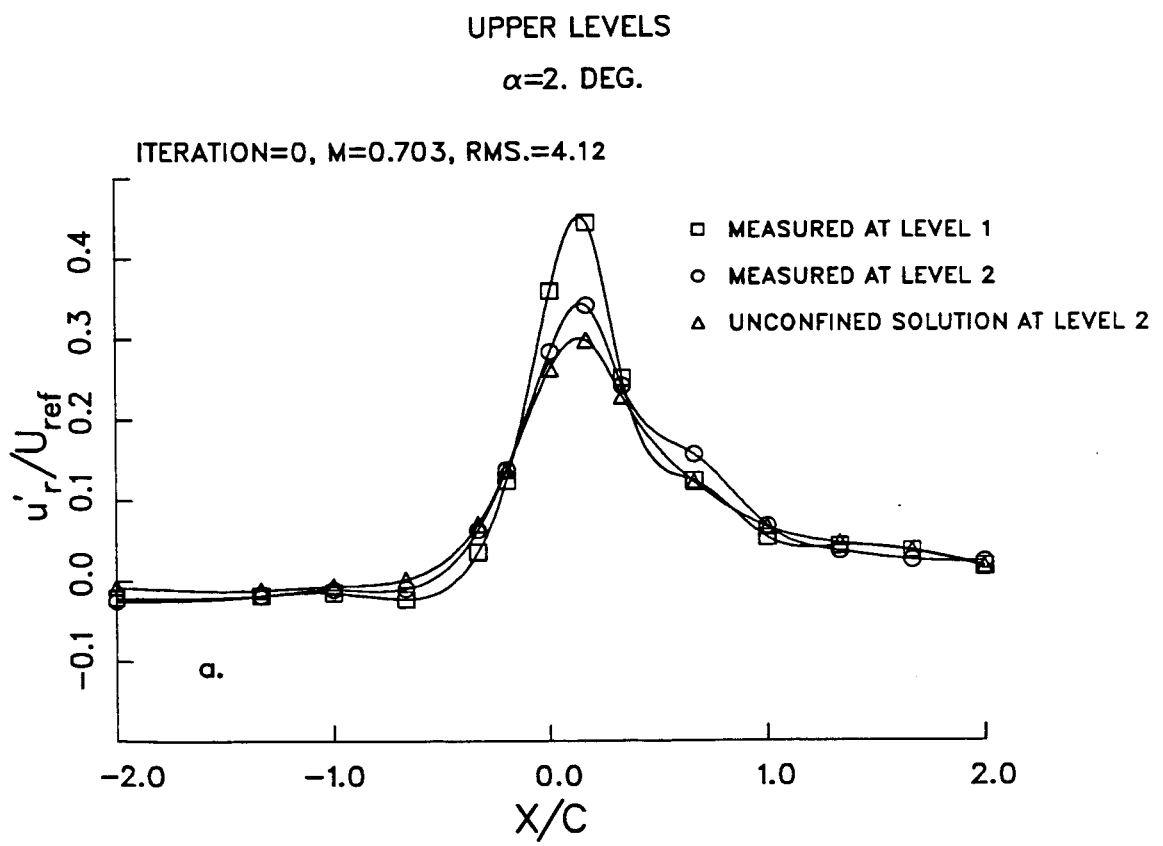

Figure 5.14a: Initial resultant velocity distributions computed from streamwise and normal velocity components at the upper levels.

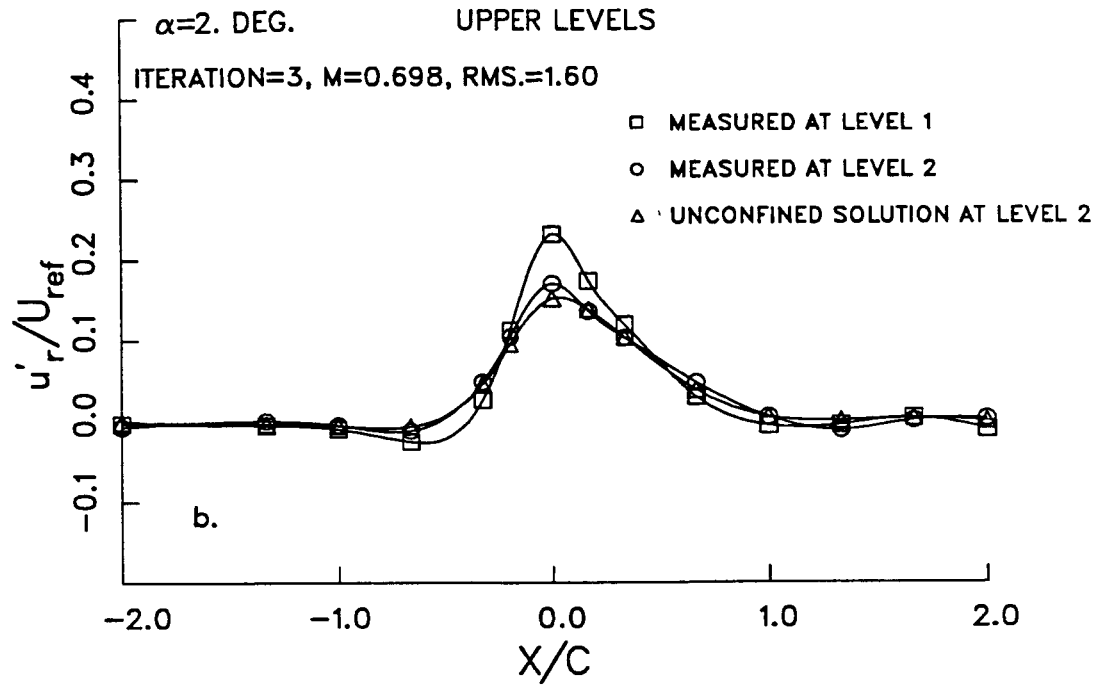

Figure 5.14b: Resultant velocity distributions at the upper levels after the corrections.

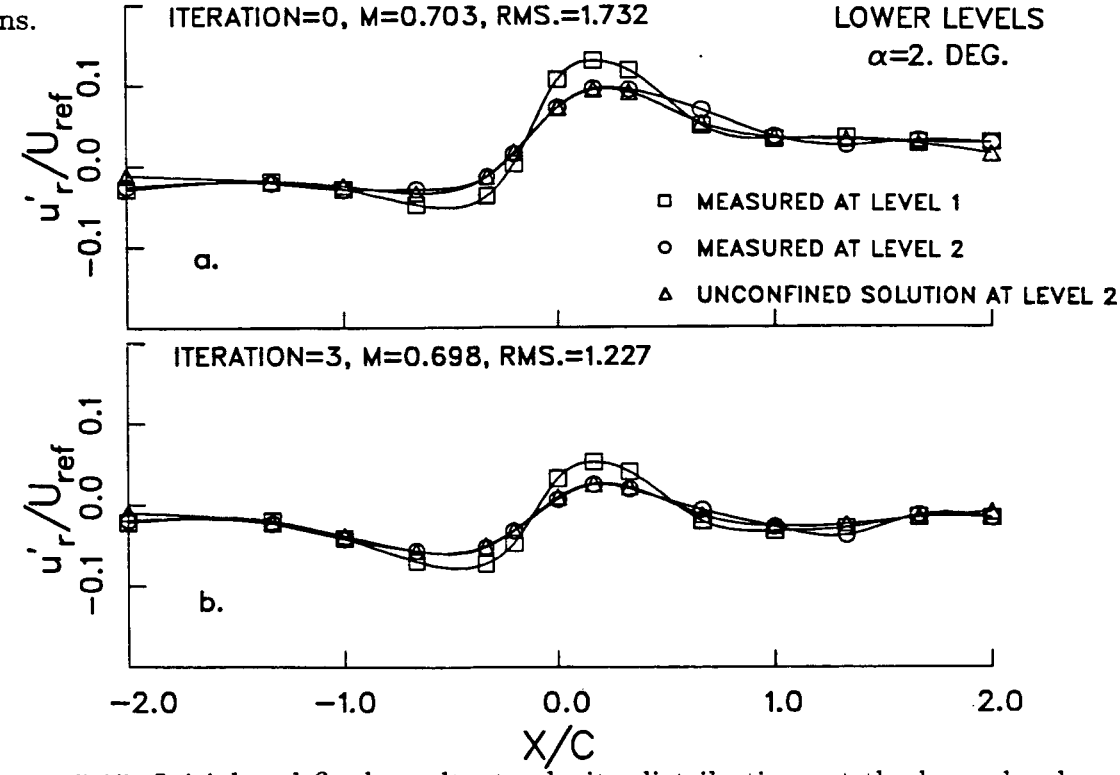

Figure 5.15: Initial and final resultant velocity distributions at the lower levels.

5.2.1.2 Two Level Iterative Scheme with Side-Wall Pressure Distribution

Velocity components were measured with the LDV system along the centerline of the test section away from the side-wall boundary layers. However, side-wall pressure measurements were subject to the viscous effects caused by the presence of boundary layers. In the previous example, it was demonstrated that the convergence of the adaptive-wall concept to the interference-free flow could be achieved if the iterations were carried out with the resultant velocity distribution. The remaining question is whether resultant velocity distribution may be estimated from side-wall pressure measurements. In the subcritical case, comparison of resultant velocity distributions from side-wall pressure measurements with those from LDV measurements, showed that the boundary layer assumption holds fairly well. At supercritical speeds or in a lifting case on the model, a complex flow field may exist on the side-walls caused by the presence of a shock wave. In that case, the side-wall pressure measurements may not give a good estimate for the velocity distribution. To explore the effects of supercritical flow and to validate the feasibility of the velocity simplification, the iterative method was applied with the side-wall pressure distribution.

Figures 5.16a and 5.17a illustrate the initial velocity distributions at the upper and the lower levels, respectively. Measurements were taken at $M = 0.702$ and at $\alpha = 2.^\circ$ Initially, a weak shock wave was present at the first level in the upper half. The comparison of this case to the one with the streamwise velocity distributions at the same Mach number and angle of attack (Figures 5.9a and 5.10a), shows that side-wall pressure measurements underestimate the velocity distributions at the control levels. Using the estimated resultant velocity distributions, the iterative scheme was applied and wall interference was almost eliminated at the upper levels after five iterations as shown in Figure 5.16b. About 70 % reduction in the rms error was achieved in the velocity distributions in the upper half. At the lower levels, some improvement is obtained in matching the unconfined flow solution to the measured velocity distribution over the model (Figure 5.17b).

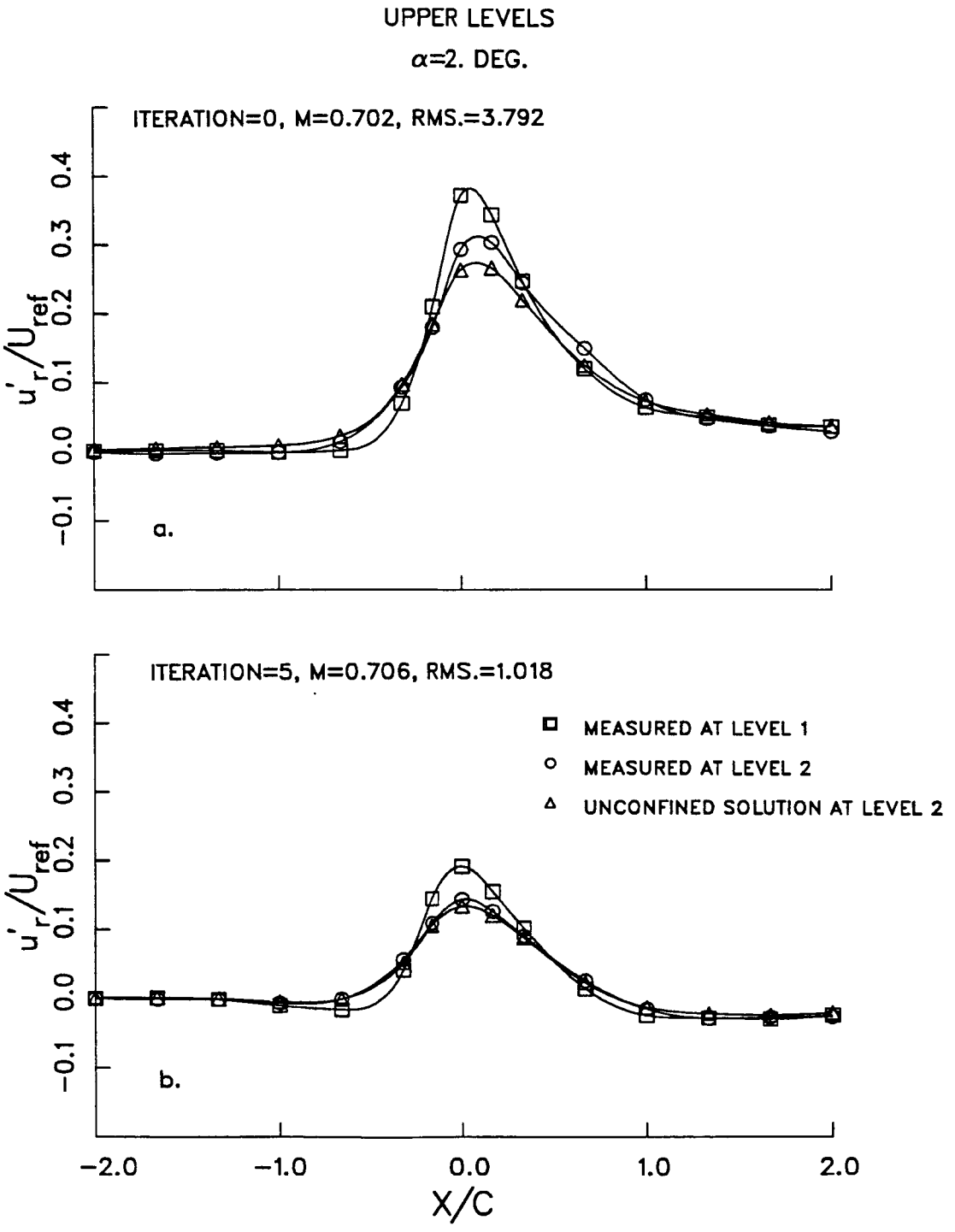

Figure 5.16: Resultant velocity distributions from side-wall pressure measurements at the upper levels in the supercritical lifting case, two-level iterative method.

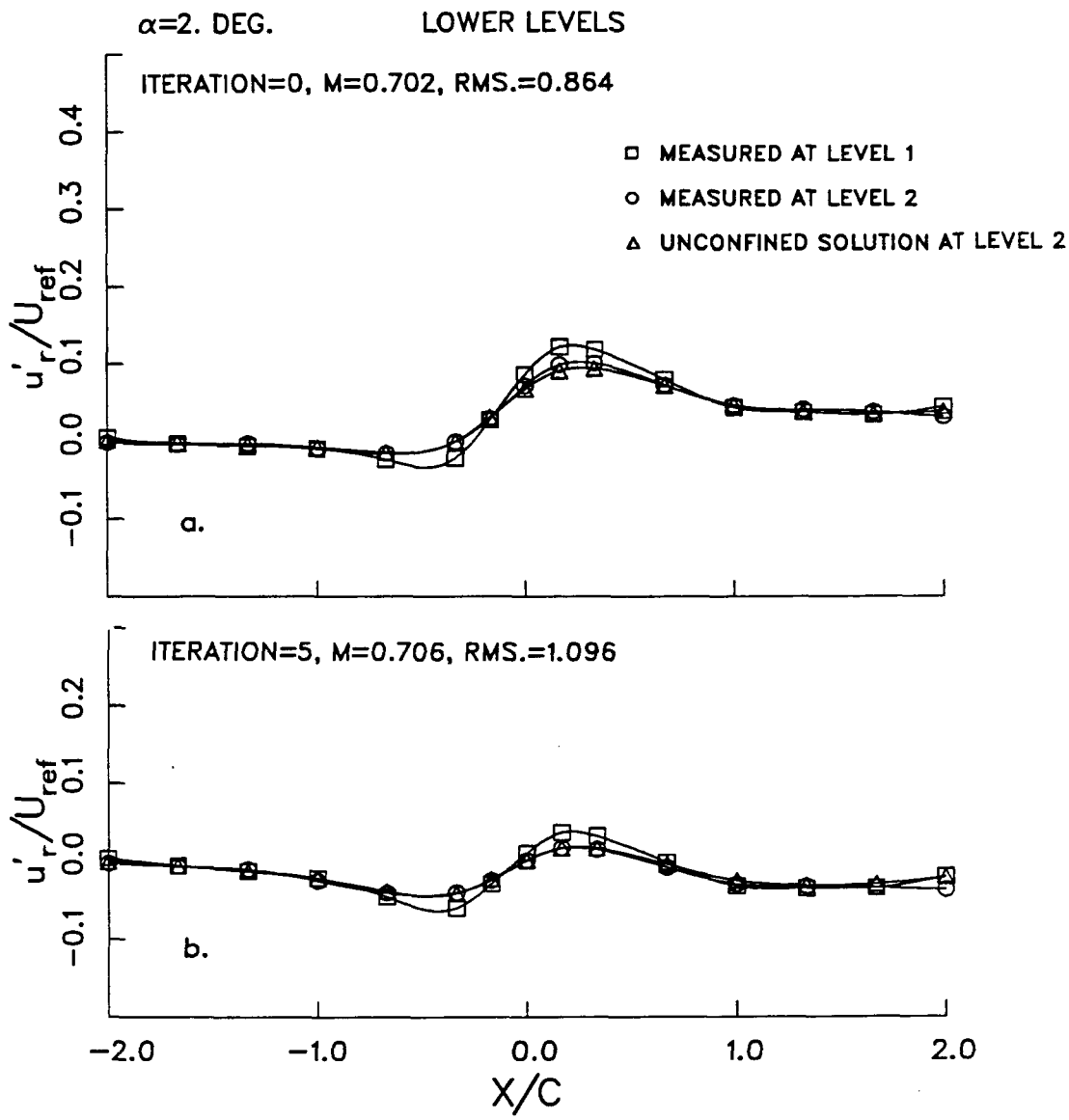

Figure 5.17: Resultant velocity distributions from side-wall pressure measurements at the lower levels in the supercritical lifting case, two-level iterative method.

Top and bottom plenum pressure distributions are given in Figure 5.18. Comparison with the previous case (Figure 5.11) shows similar pressure adjustments in the plenum compartments directly above and below the model while the last ones differ slightly. As pointed out previously, the small changes in the downstream compartments do not affect the upstream disturbance velocity distribution.

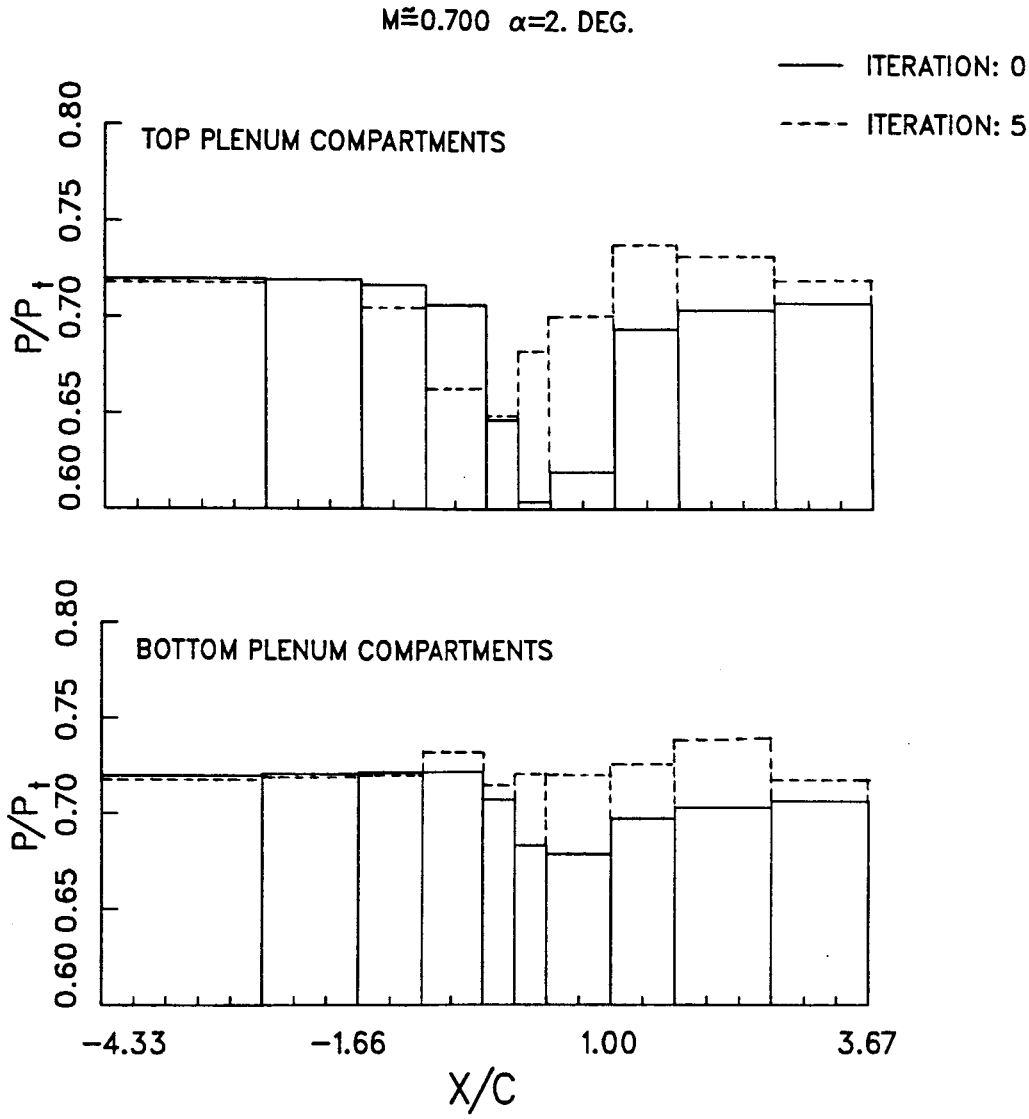

Figure 5.18: Plenum pressure distributions before and after the corrections.

Model pressure distributions measured after the initial and the final iterations, are compared with the Calspan data[45] and the numerical solution from the TAIR code[47] in Figure 5.19. The initial position of the shock wave is at the 50 %-chord of the model. In the final iteration, it was moved to a position in good agreement with the other results.

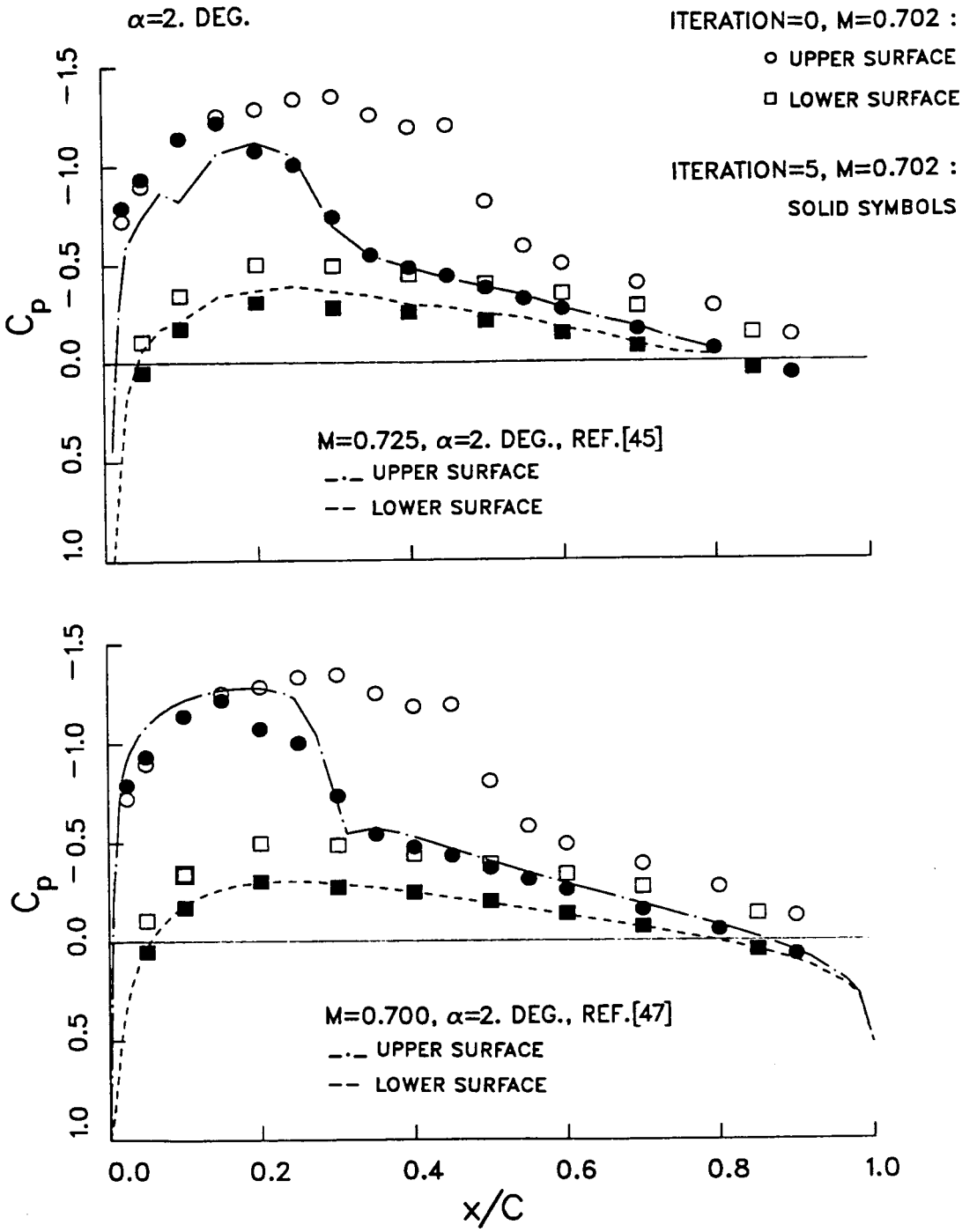

Figure 5.19: Comparison of the initial and final model pressure distributions with the Calspan data[45] and TAIR solution[47].

5.2.1.3 Two-Level One-Step Scheme with Side-Wall Pressure Distribution

After having shown the validity of using the side-wall pressure distribution in the adaptive-wall concept, the next step was to establish the applicability of the one-step scheme using the linearized influence coefficients.

Figures 5.20a and 5.21a show the initial resultant velocity distributions which were obtained from side-wall pressure measurements at $M = 0.699$ and $\alpha = 2.°$ at the upper and the lower levels respectively. Cumulative pressure corrections were determined by the one-step convergence scheme and they were applied in the plenum compartments as the final experimental step.

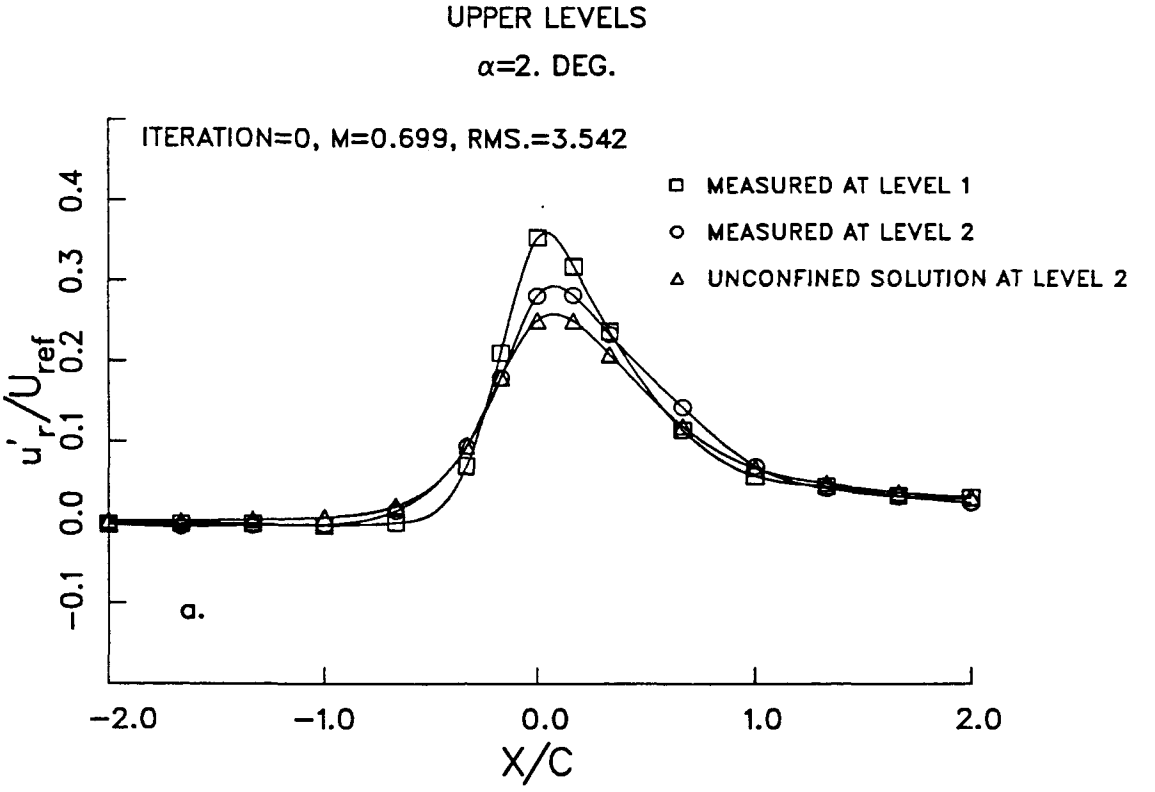

Figure 5.20a: Initial resultant velocity distributions from side-wall pressure measurements at the upper levels in the supercritical case, two-level one-step method.

Figure 5.20b shows the velocity distributions at the upper levels after one iteration. Although the rms error decreased considerably (about 58 %), a small amount of interference remained in the velocity distribution at a portion of the control level over the quarter-chord point of the model. However, a small variation is also observed at the corresponding lower level points (Figure 5.21b).

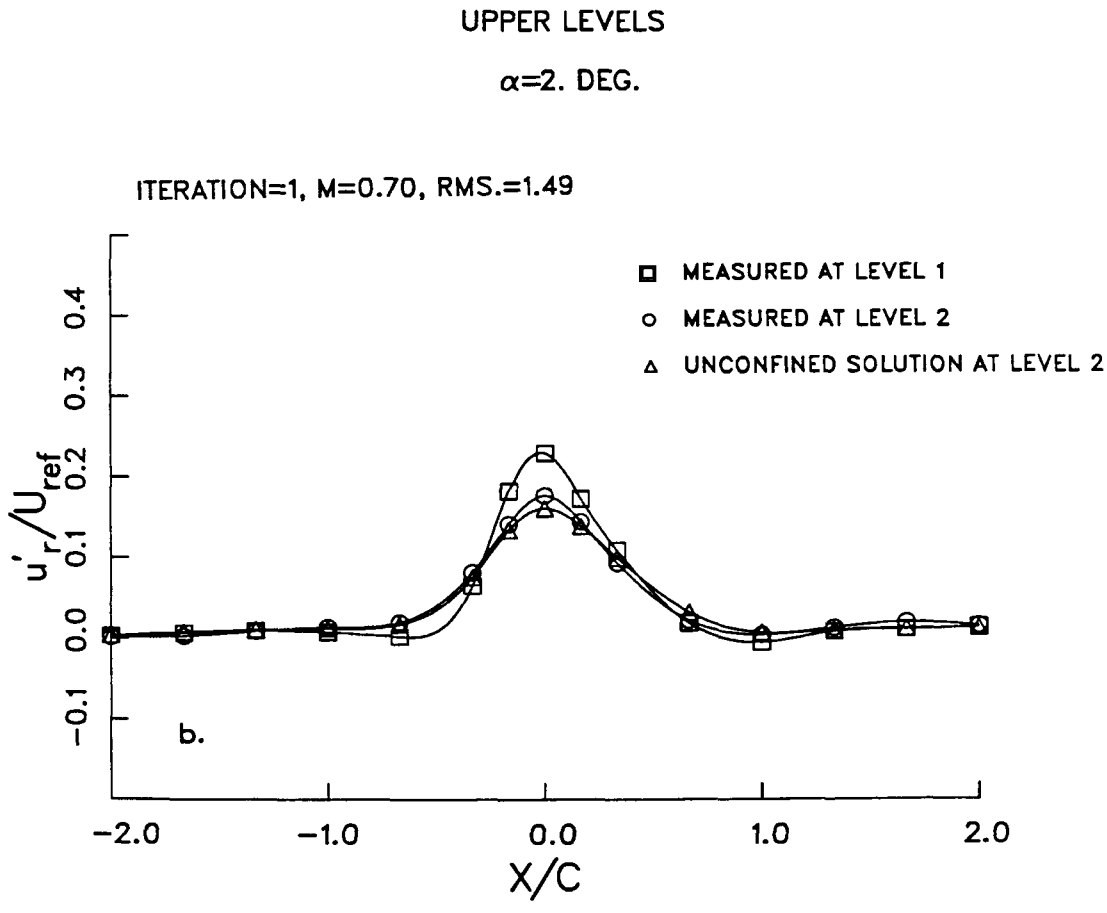

Figure 5.20b: Resultant velocity distributions from side-wall pressure measurements at the upper levels in the supercritical case after the corrections, two-level one-step method.

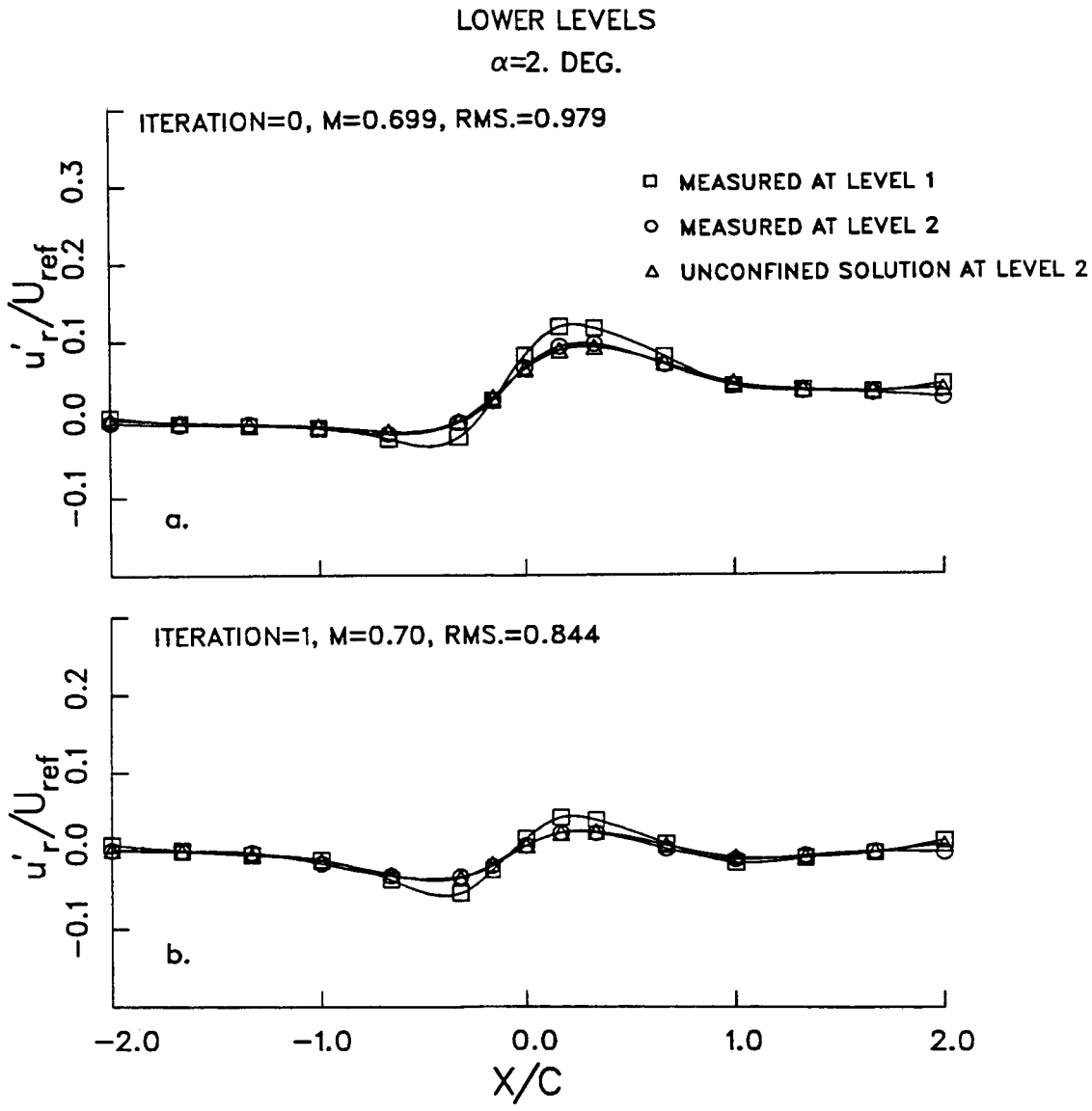

Figure 5.21: Resultant velocity distributions from side-wall pressure measurements at the lower levels in the supercritical case before and after the corrections using the one-step convergence scheme.

Comparison of the top and bottom plenum pressure distributions after the first iteration (Figure 5.22) with those from the application of the iterative scheme (Figure 5.18) reveals that plenum pressures were altered in the right direction. However, it also indicates that further adjustments are required in some plenum compartments.

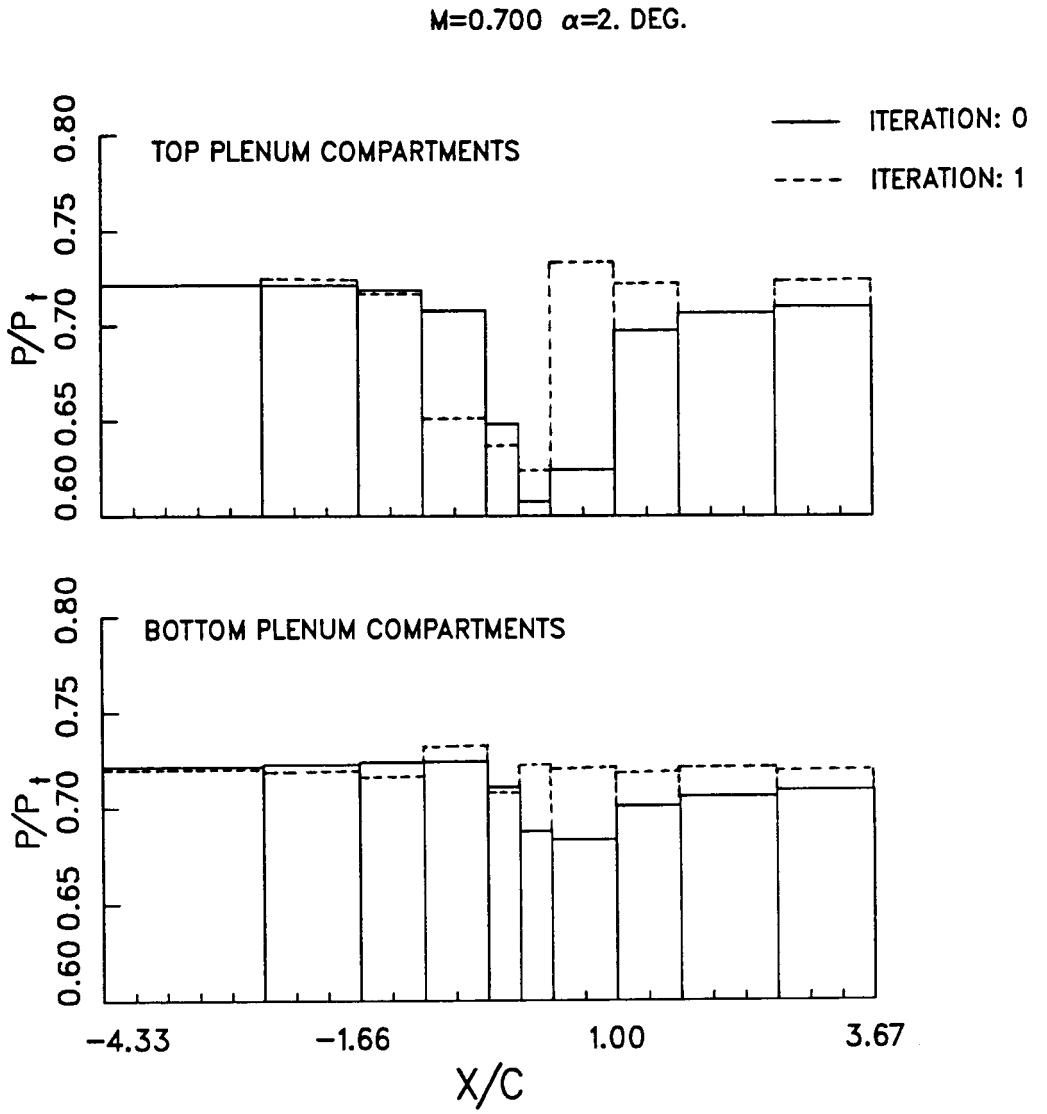

Figure 5.22: Plenum pressure distributions before and after the corrections using the one-step convergence scheme.

The discrepancy observed in the comparison of the measured model pressure distribution with the experimental[45] and the computational data[47], (Figure 5.23) is due to the residual interference that remained in the velocity distribution because of incomplete pressure adjustments. The position of the shock is slightly off toward

the trailing edge and the pressure coefficient is higher at $x/C \sim 0.10$ compared to the well-converged case in Figure 5.19.

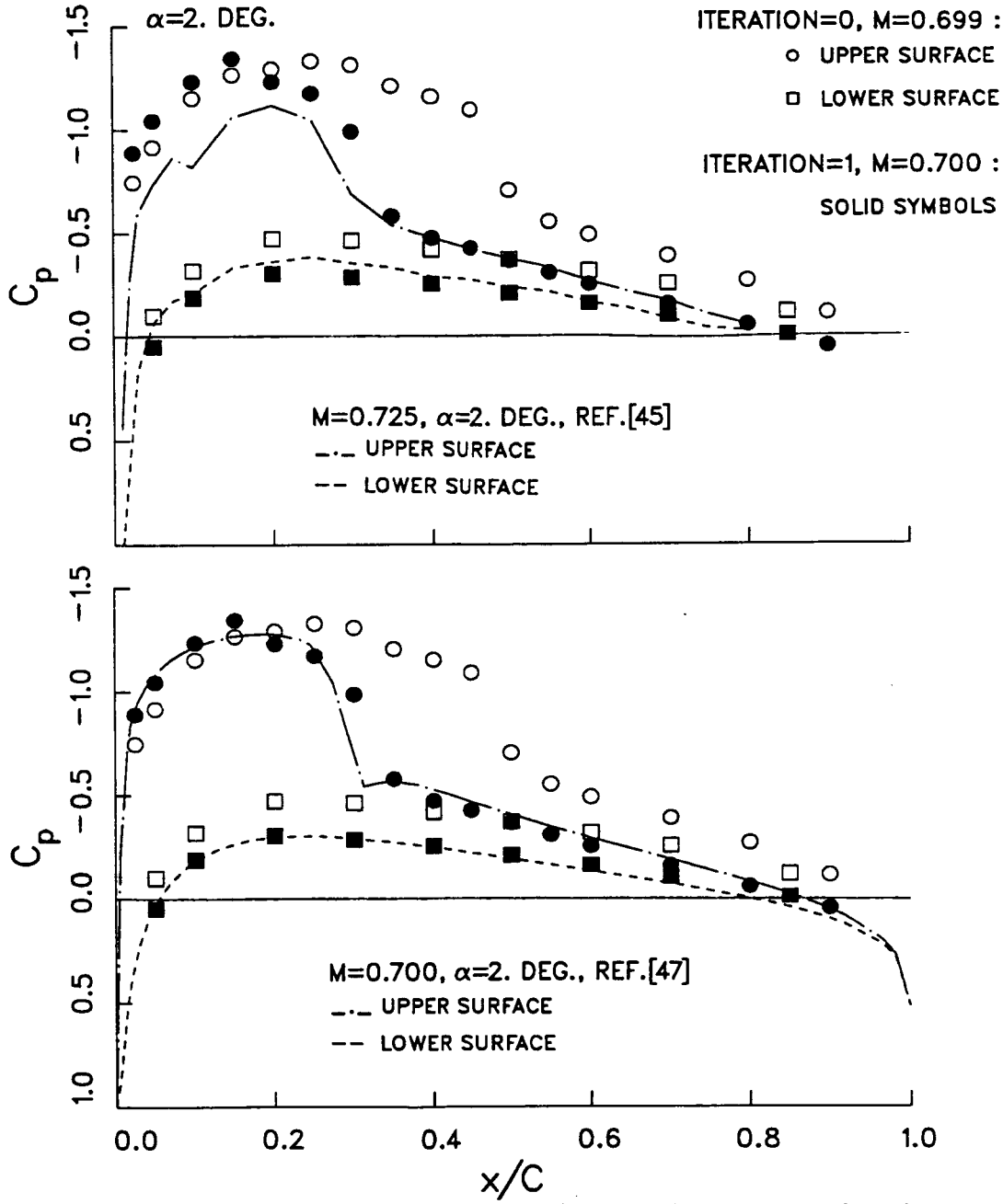

Figure 5.23: Comparison of the initial and final model pressure distributions with the Calspan data[45] and TAIR solution[47].

5.2.1.4 Discussion

These results suggest that the estimated resultant velocity distribution from side-wall pressure measurements and the approximate calculation of unconfined flow in the schemes with side-wall pressure distribution may be acceptable for adaptive-wall experiments.

The comparison of the iterative scheme (Figures 5.16 and 5.17) and the one-step scheme (Figures 5.20 and 5.21) reveals that the number of iterations could be reduced at least by three in this particular case with the application of the one-step convergence scheme. In this supercritical lifting case, it was also shown that convergence can be achieved with the use of linearized influence coefficients.

As shown in Figure 5.24a, in the presence of a shock wave that has penetrated the control level, the unconfined solution using the transonic small disturbance equation predicts a different velocity distribution at level 2 compared to the solution obtained from the linear equation.

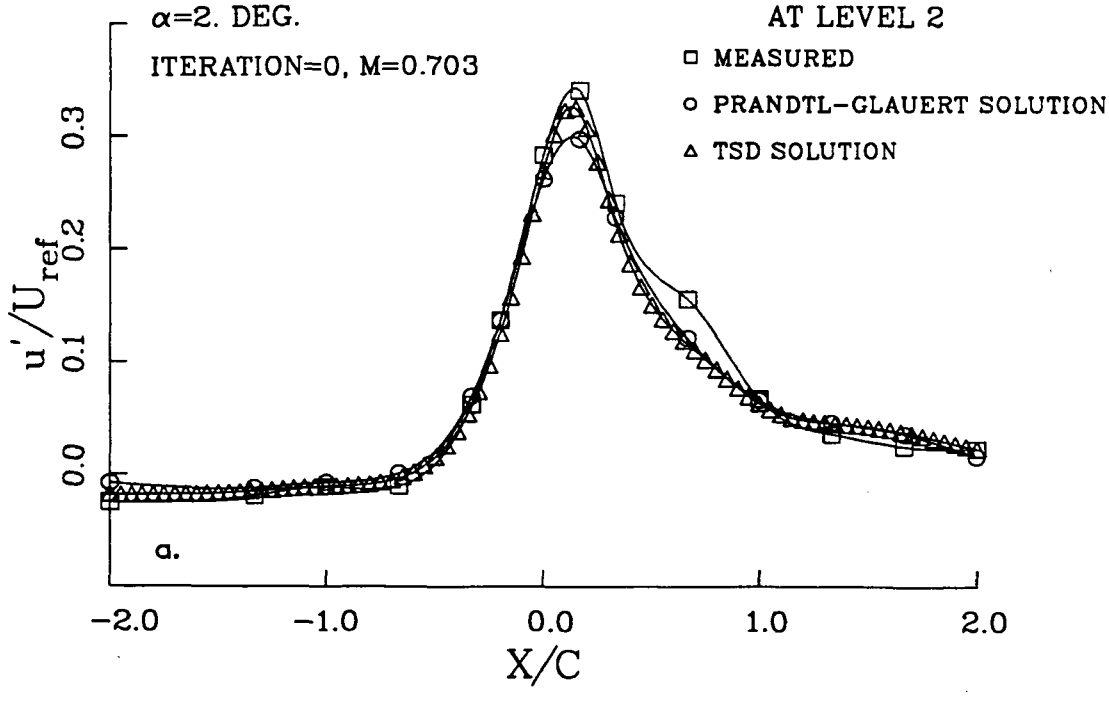

Figure 5.24a: Comparison of the linear and nonlinear unconfined flow solutions at level 2 with the measured data before the corrections in the supercritical case.

After the final iteration, linear and nonlinear solutions are in agreement since there is no shock wave present (Figure 5.24b). In spite of the initial presence of a shock wave at the control levels, the linearized equations were used to calculate the unconfined flow field and iterations were carried out successfully.

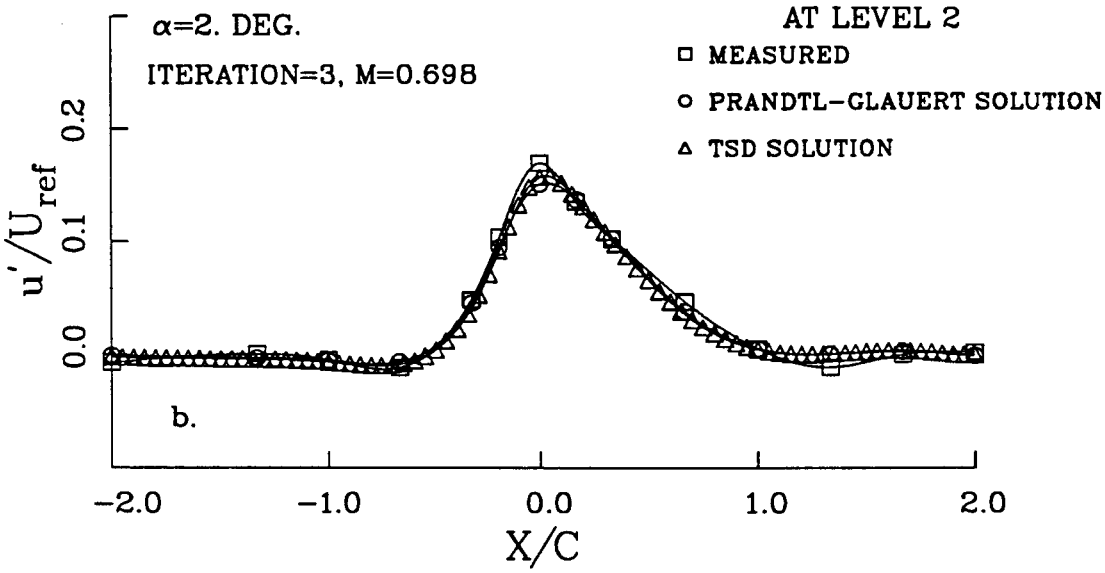

Figure 5.24b: Comparison of the linear and nonlinear unconfined flow solutions after the corrections.

Approximate calculations of the unconfined velocity distribution in the nonlinear flow field and plenum pressure corrections with the use of linearized influence coefficients are probably the major reasons for not obtaining a complete convergence in one-step. It is inferred that one more iteration would have achieved a better convergence to the interference-free flow as obtained in the iterative case.

5.2.2 Applications in the Subcritical Nonlifting Case

The purpose of the applications in this section is to demonstrate that the two-level iterative and one-step convergence schemes can easily be implemented with the simplified flow variable. With the advantage of having fast and reduced number of iterations, similar results can be obtained as compared to those of the one-level two-component iterative scheme. In order to compare the results properly, all the

experiments were carried out at $M \approx 0.7$ and $\alpha = 0.°$

5.2.2.1 One-Level Iterative Scheme with Disturbance Velocity Components

As stated previously the one-level two-component compatibility assessment was introduced by Sears[15], and verified experimentally in several studies[8,18]. In this example, velocity measurements were taken at level 1. Figure 5.25a shows the initial measured and calculated velocity distributions. Experiments were stopped at the fifth iteration because of time limitations and since little gain was apparent after the fourth iteration. Some discrepancies are observed between the unconfined solution and the measured streamwise velocity distribution after the final iteration as illustrated in Figure 5.25b. Some of the error is probably due to the slight variation in the freestream velocity and the sensitivity of the integration to the changes in the normal velocity component. The measured model pressure distribution is illustrated in Figure 5.26. After the final iteration, it is generally in good agreement with the experimental data base[46].

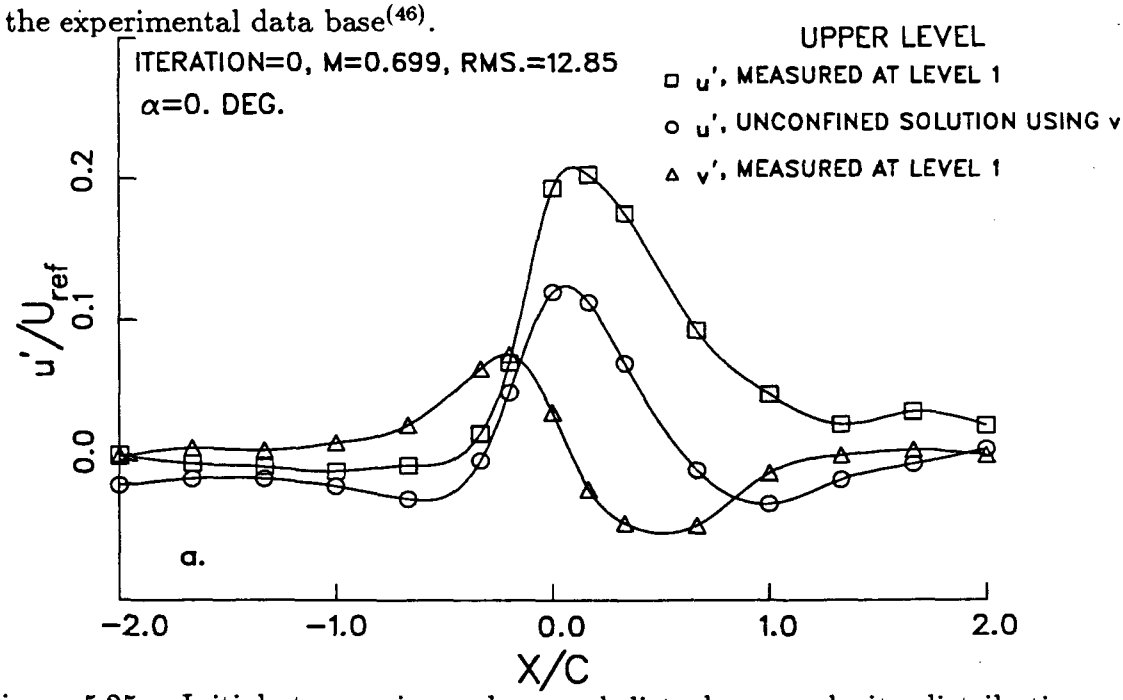

Figure 5.25a: Initial streamwise and normal disturbance velocity distributions in the subcritical nonlifting case, one-level iterative method.

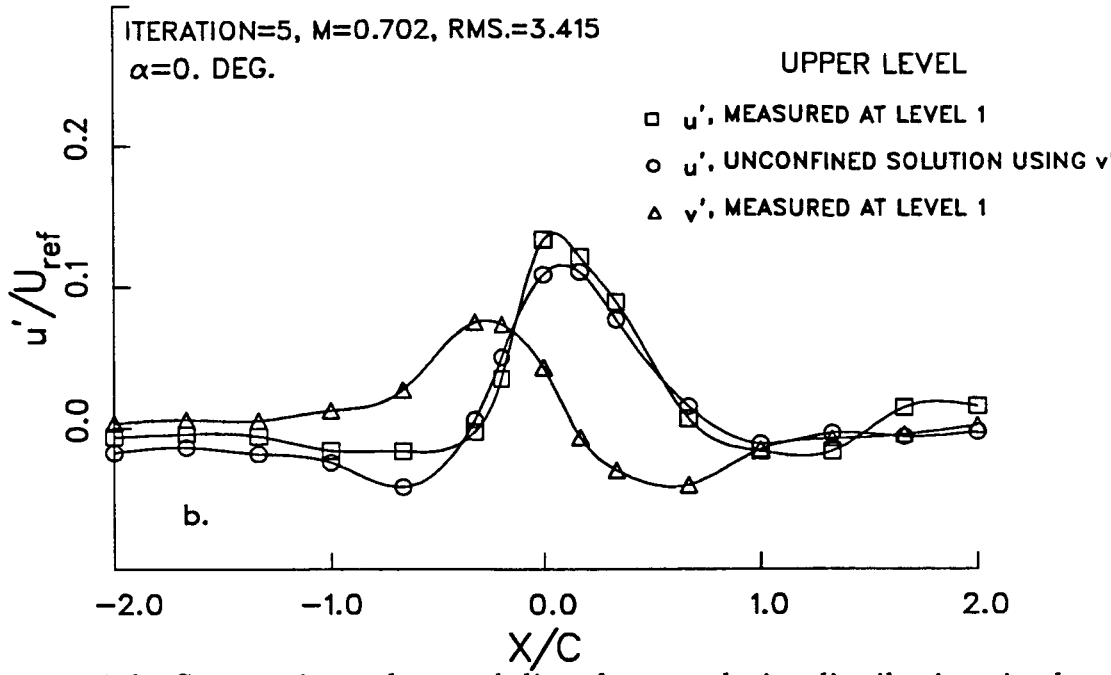

Figure 5.25b: Streamwise and normal disturbance velocity distributions in the subcritical nonlifting case after the corrections, one-level iterative method.

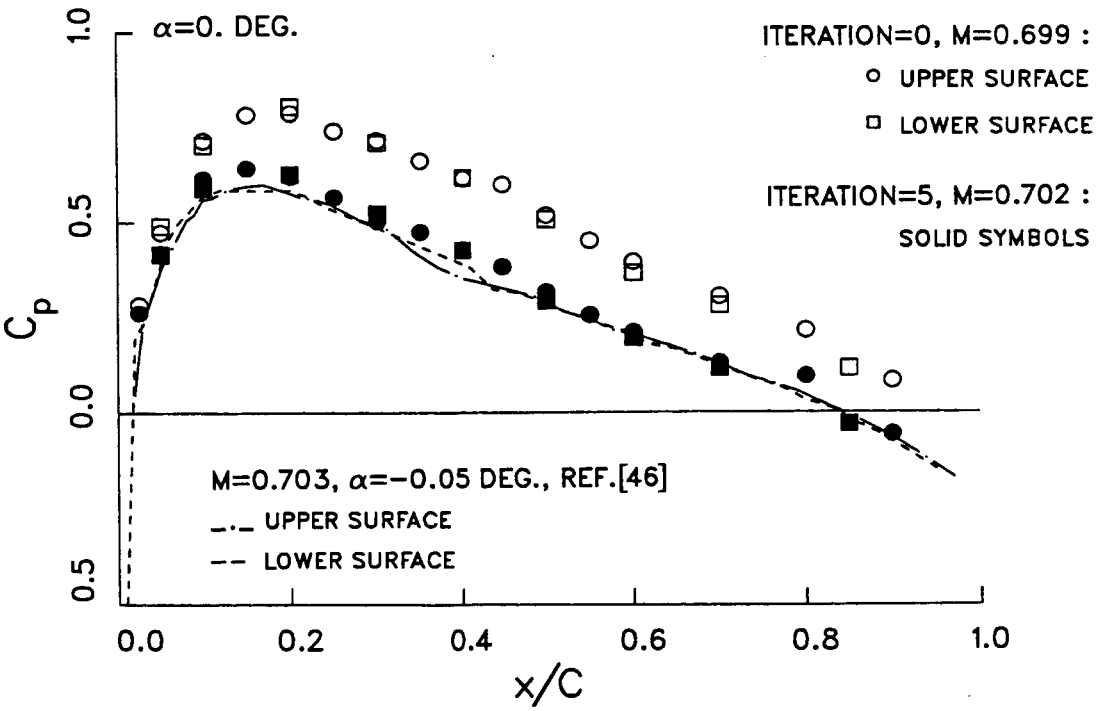

Figure 5.26: Comparison of the initial and final model pressure distributions with an experimental data base[46].

5.2.2.2 Two-Level One-Step and Iterative Schemes with Streamwise Velocity Distribution

In the application of the iterative scheme, initial velocity distributions were taken at $M = 0.702$ and zero angle of attack (Figure 5.27a). A fairly good convergence to the interference-free flow was achieved after 2 iterations as illustrated in Figure 5.27b. In the second iteration, 10 control points were used for the wall interference assessment at level 2 while the velocity measurements were made at 15 points at level 1 to eliminate the tail-effects as much as possible for the calculation of the unconfined flow. After the second iteration, the rms error decreased about 58 % and the disturbance velocities at level 1 and level 2 were reduced. Two more iterations were carried out to improve the rms error, but the gain was minimal and the velocity distributions and the model pressure coefficient remained approximately the same. This is probably due to inexact application of the small pressure corrections.

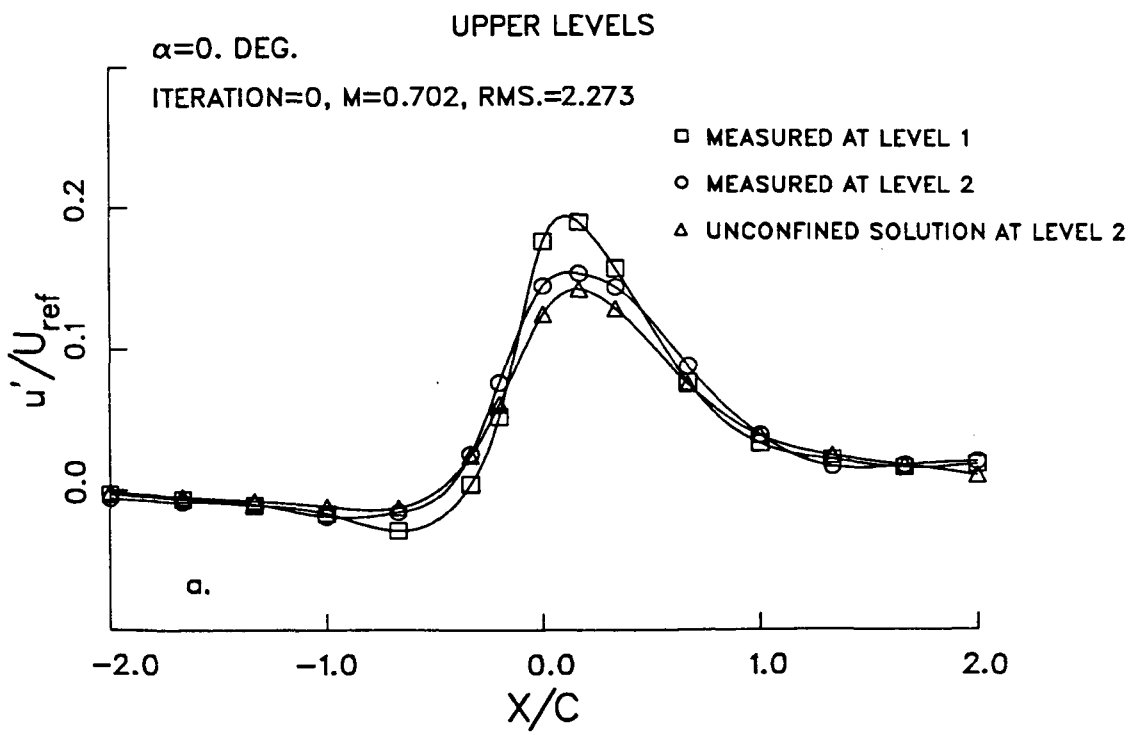

Figure 5.27a: Initial streamwise velocity distributions in the subcritical nonlifting case, two-level iterative method.

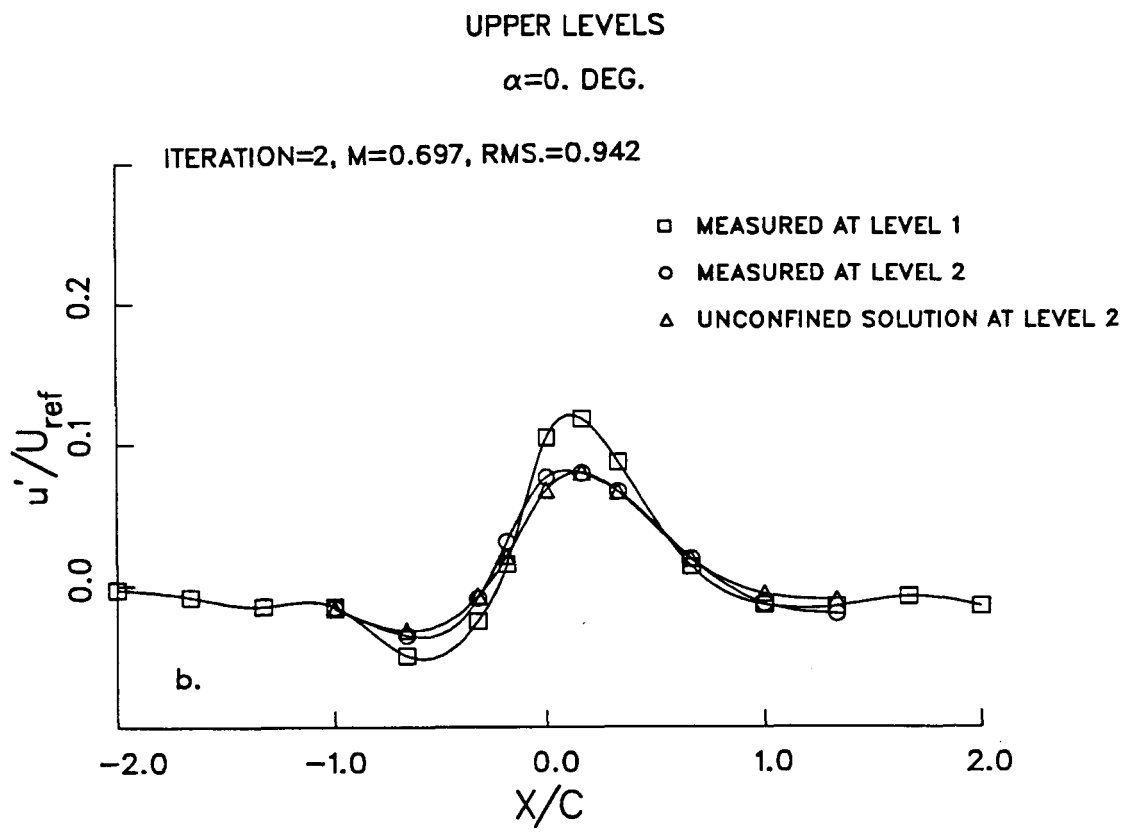

Figure 5.27b: Streamwise velocity distributions in the subcritical nonlifting case after the corrections, two-level iterative method.

In Figure 5.28, model surface pressure distributions after the zeroth and final iterations are compared with the experimental data taken at ONERA[46]. The effect of the wall interference is clearly observed between the initial and the final iterations. The converged case after the second iteration agrees well with the data base since the interference was eliminated rather well compared to the previous case.

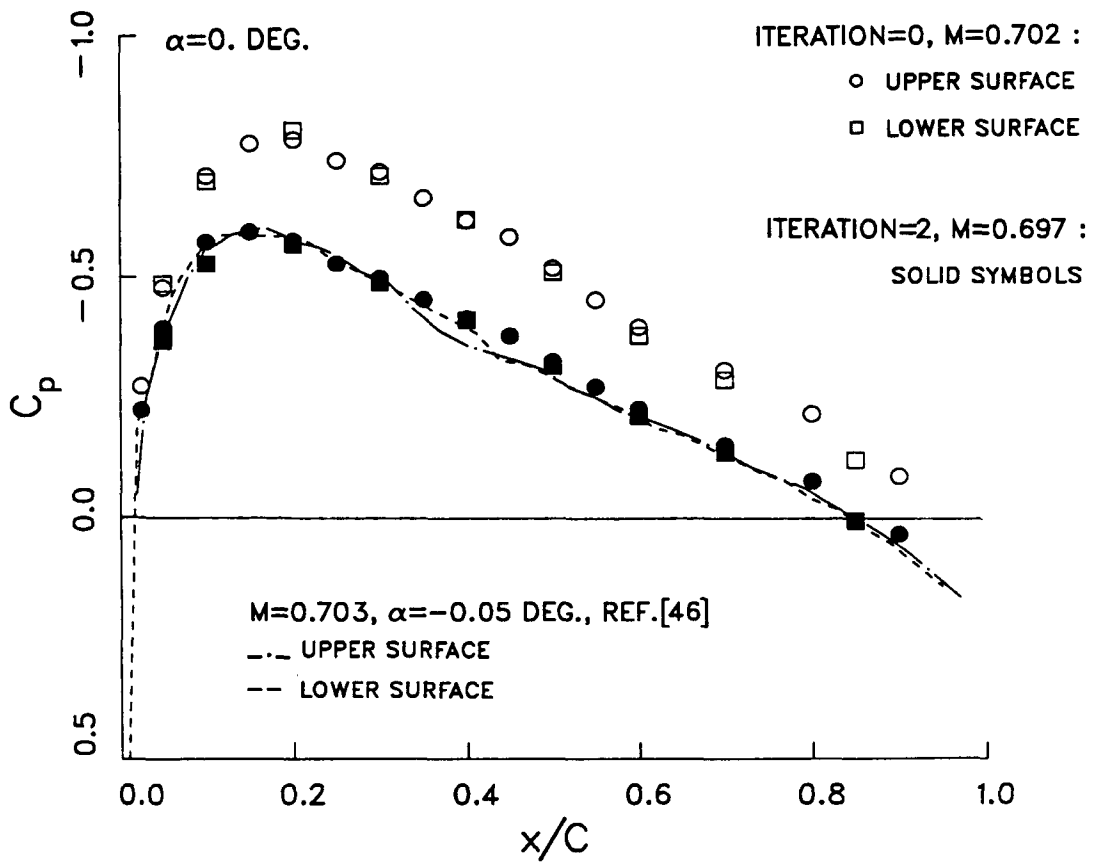

Figure 5.28: Comparison of the initial and final model pressure distributions with the ONERA data[46].

The one-step convergence scheme was applied at the same flow conditions, that is, at about the same Mach number and the angle of attack. The cumulative pressure corrections were determined using the one-step algorithm. After the first iteration, the test section Mach number was adjusted to 0.702 from 0.744 since it varied when suction and blowing were applied. Figure 5.29 illustrates the velocity distributions before and after the pressure corrections.

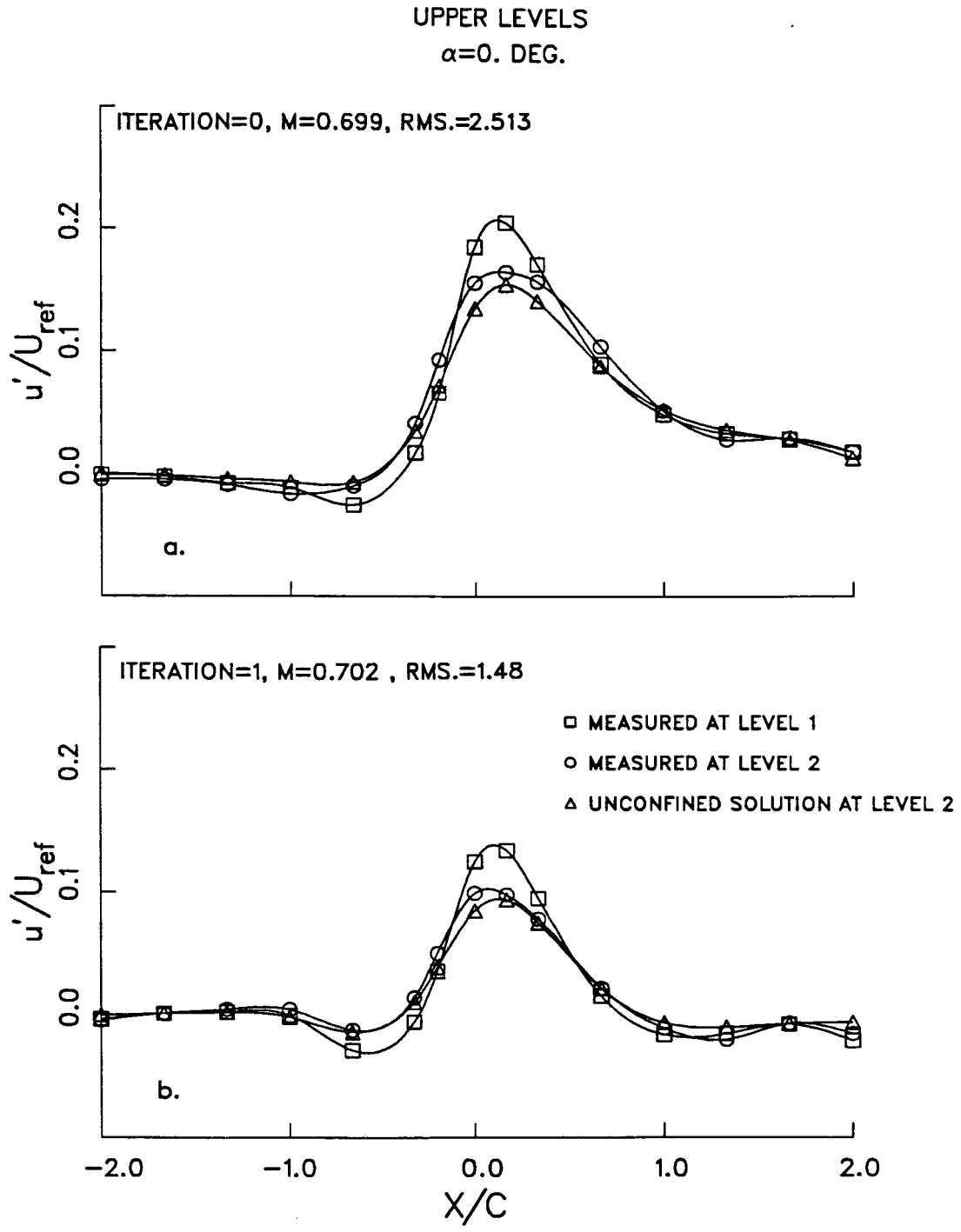

Figure 5.29: Streamwise velocity distributions in the subcritical nonlifting case before and after the corrections, two-level one-step method.

The measured model pressure distribution is compared with the ONERA data in Figure 5.30 and a good agreement is observed although a perfect matching of the velocity distributions at level 2 could not be obtained in one iteration. In these last two cases, the discrepancies between the unconfined solution and the measured velocities at level 2 are observed above the quarter-chord point of the model which is located at $X/c = 0$ (Figures 5.27 and 5.29). One reason is probably the incomplete control caused by the finite number of plenum compartments over this region with the high velocity gradient.

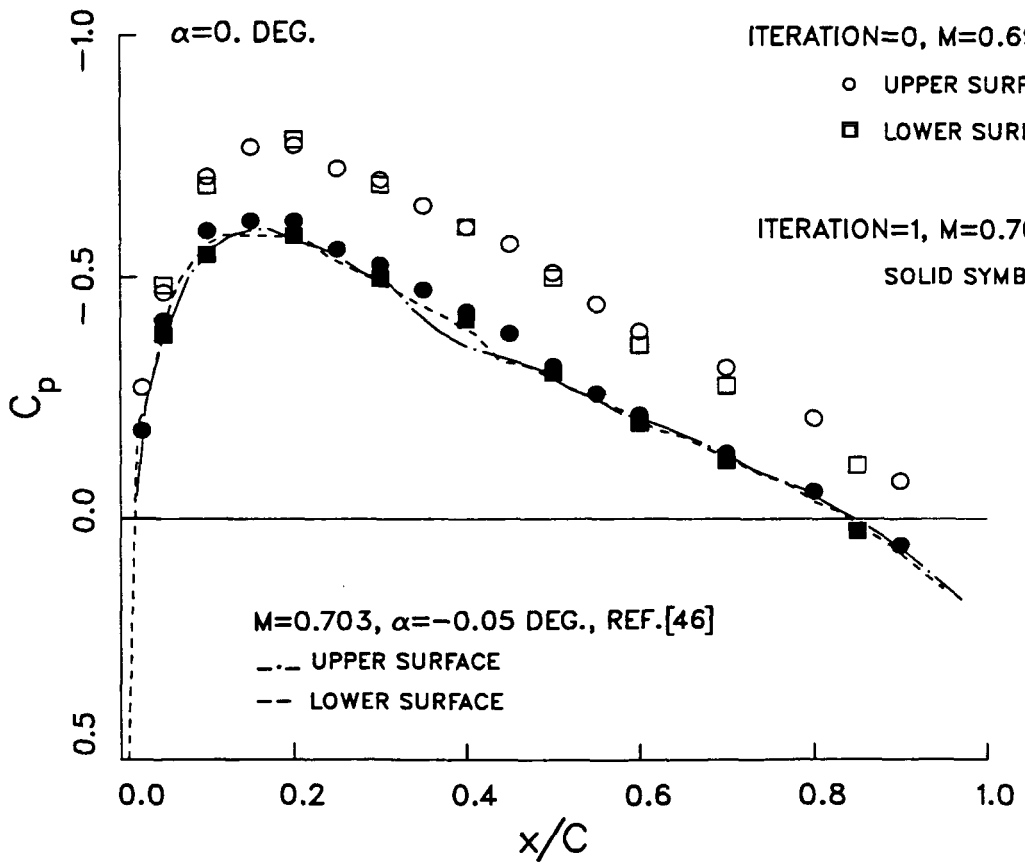

Figure 5.30: Comparison of the initial and final model pressure distributions with the ONERA data[46].

5.2.2.3 Two-Level One-Step and Iterative Schemes with Side-Wall Pressure Distribution

The one-step and iterative convergence schemes were applied with the resultant velocity distributions determined from side-wall pressure measurements.

Figure 5.31a illustrates the initial velocity distributions at the control levels at $M = 0.706$ and zero angle of attack for the case of the one-step method. After the application of cumulative pressure corrections which were determined using the one-step algorithm, wall interference was almost eliminated as illustrated in Figure 5.31b. Due to the suction and blowing applied in the plenum compartments, the test section Mach number increased to 0.715 and for comparison purposes with the iterative case, the model surface pressure distribution was taken at that Mach number.

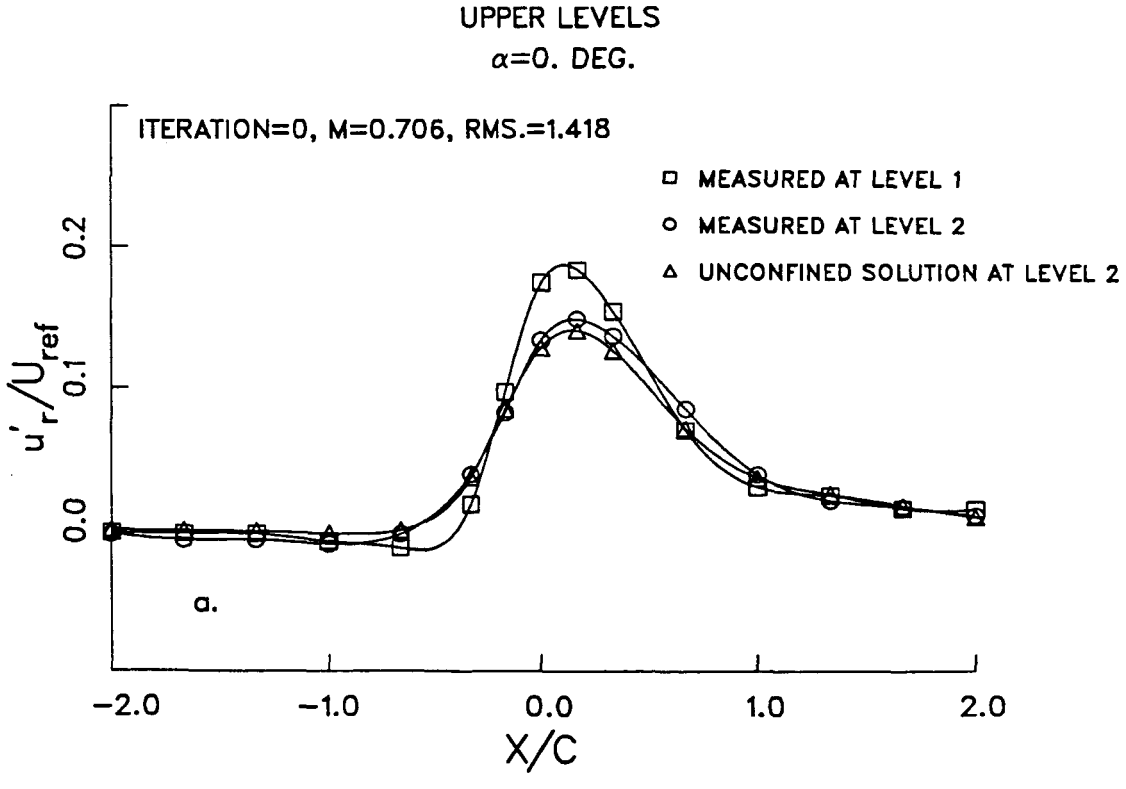

Figure 5.31a: Initial resultant velocity distributions from side-wall pressure measurements in the subcritical nonlifting case, two-level one-step method.

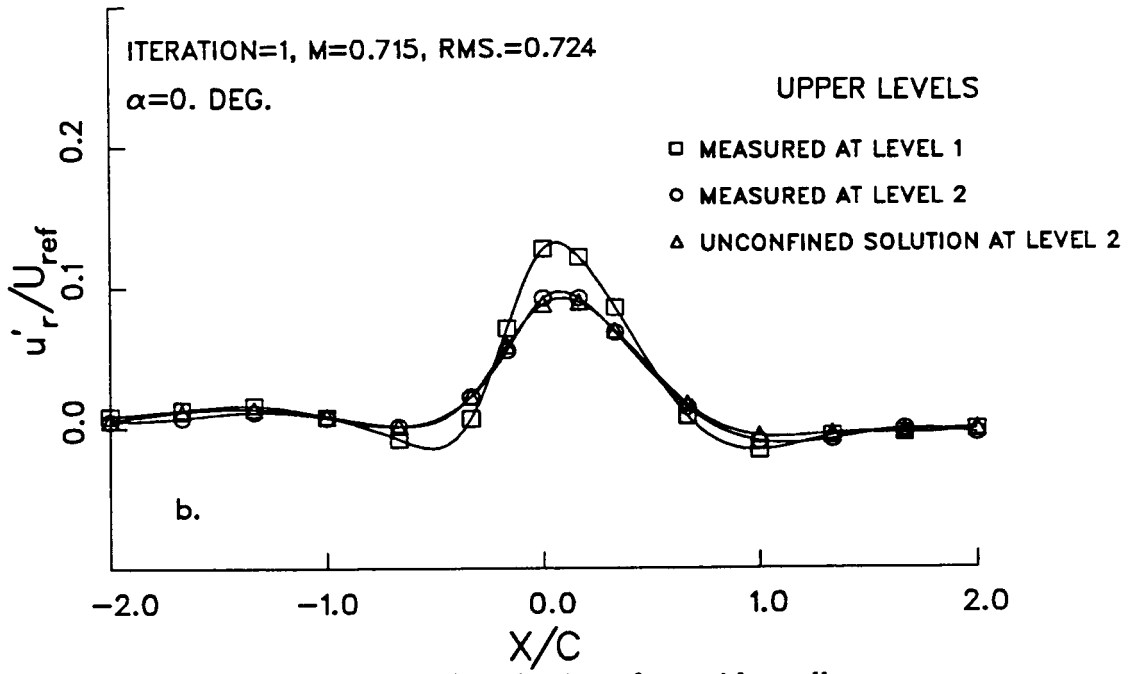

Figure 5.31b: Resultant velocity distributions from side-wall pressure measurements after the one-step iteration in the subcritical nonlifting case.

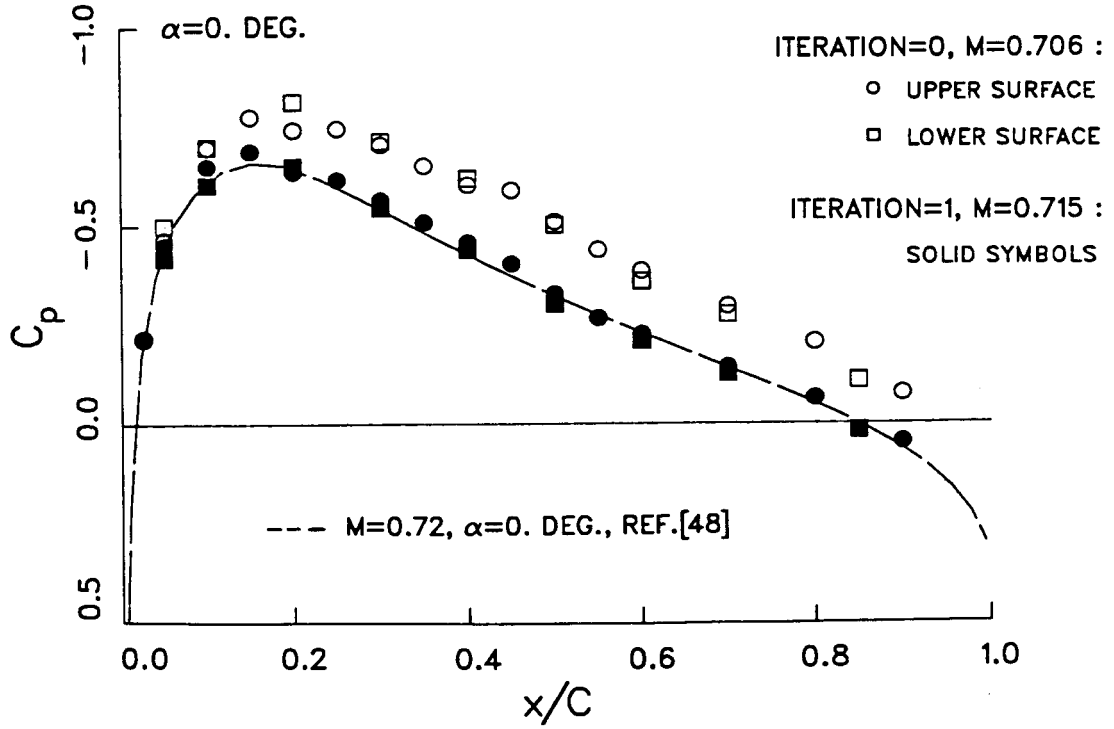

Figure 5.32: Comparison of the initial and final model pressure distributions with the computational data[48].

The iterative scheme was started at $M = 0.726$ as shown in Figure 5.33a and the flow initially was nearsonic at the airfoil surface. As presented in Figure 5.33 a, b, c and d, convergence to the interference-free flow was achieved in three iterations. After two iterations, wall interference was eliminated significantly. The last iteration further reduced the rms error for a better convergence. Initial and final model pressure distributions were compared with the computational data compiled by Lock[48]. Figures 5.32 and 5.34 show that similar results were obtained after the final iterations for both methods.

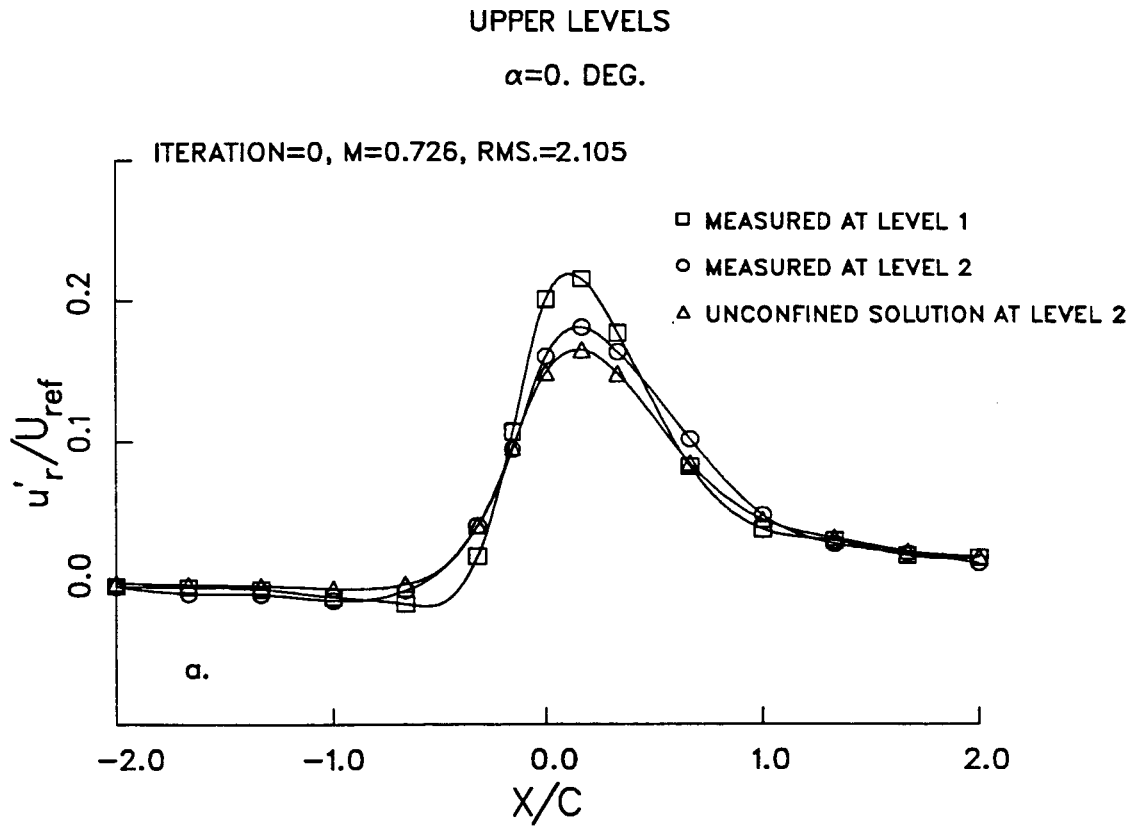

Figure 5.33a: Initial resultant velocity distribution from side-wall pressure measurements in the subcritical nonlifting case, two-level iterative method.

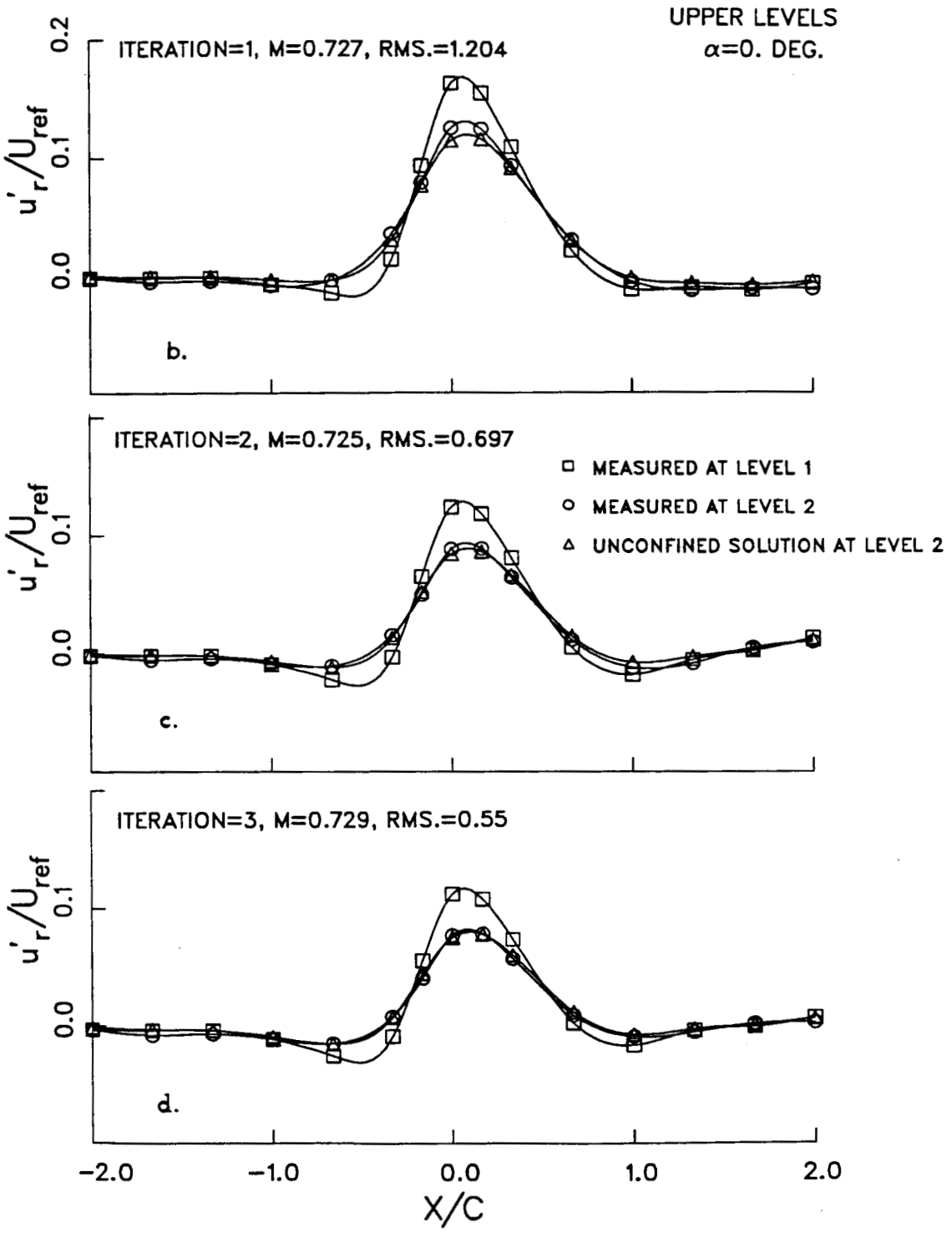

Figure 5.33b,c,d: Convergence sequence in the application of the iterative convergence scheme in the subcritical nonlifting case.

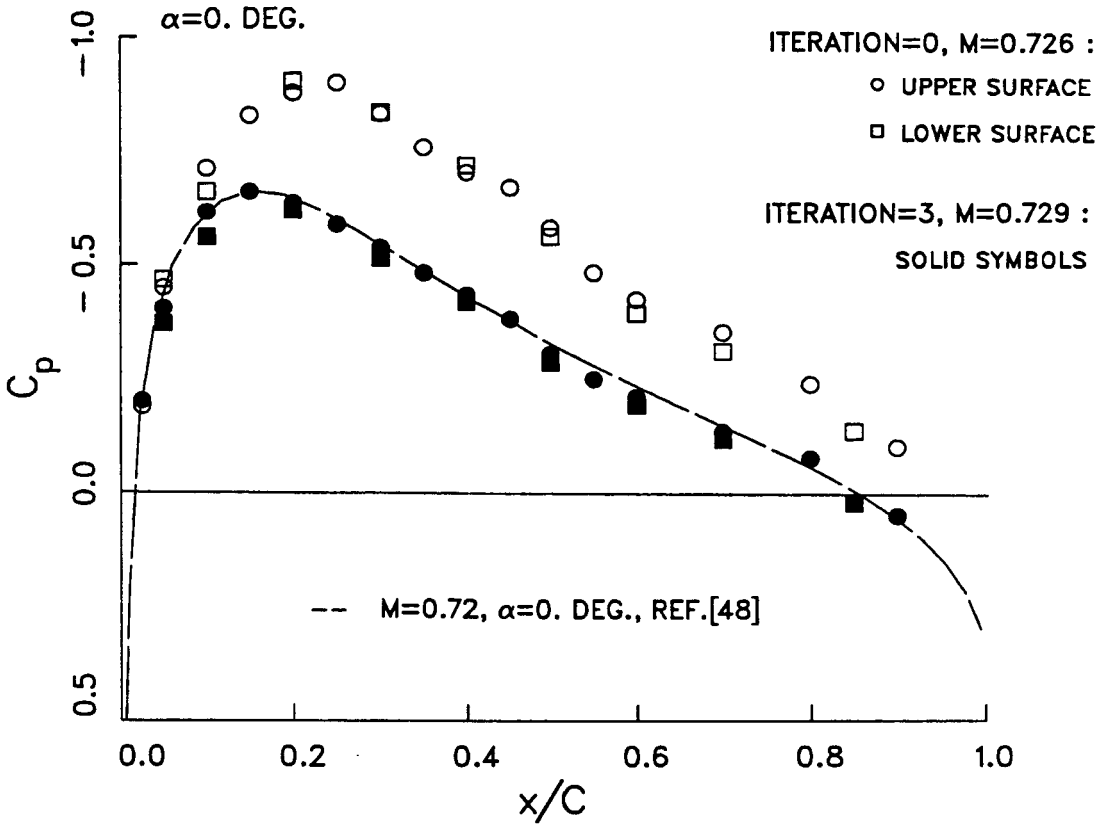

Figure 5.34: Comparison of the initial and final model pressure distributions with the computational data[48].

5.2.3 Additional Applications with the Side-Wall Pressure Distribution

5.2.3.1 Subcritical Nonlifting Case

Because of the blockage effect, the maximum Mach number attained in the test section was approximately limited to $M = 0.75$ with a nonlifting model if there was no wall control. At these flow conditions, the iterative scheme was applied with the side-wall pressure distribution. Initially, the flow was supercritical at some points of both control levels. Although the model was not at incidence, wall effects

were very severe on the velocity distributions and the model pressure coefficients at this Mach number (Figure 5.35a and 5.36). Convergence to the interference free flow was achieved in three iterations (Figure 5.35b). The rms error in the velocity distributions dropped from 4.799 to a final value of 0.806.

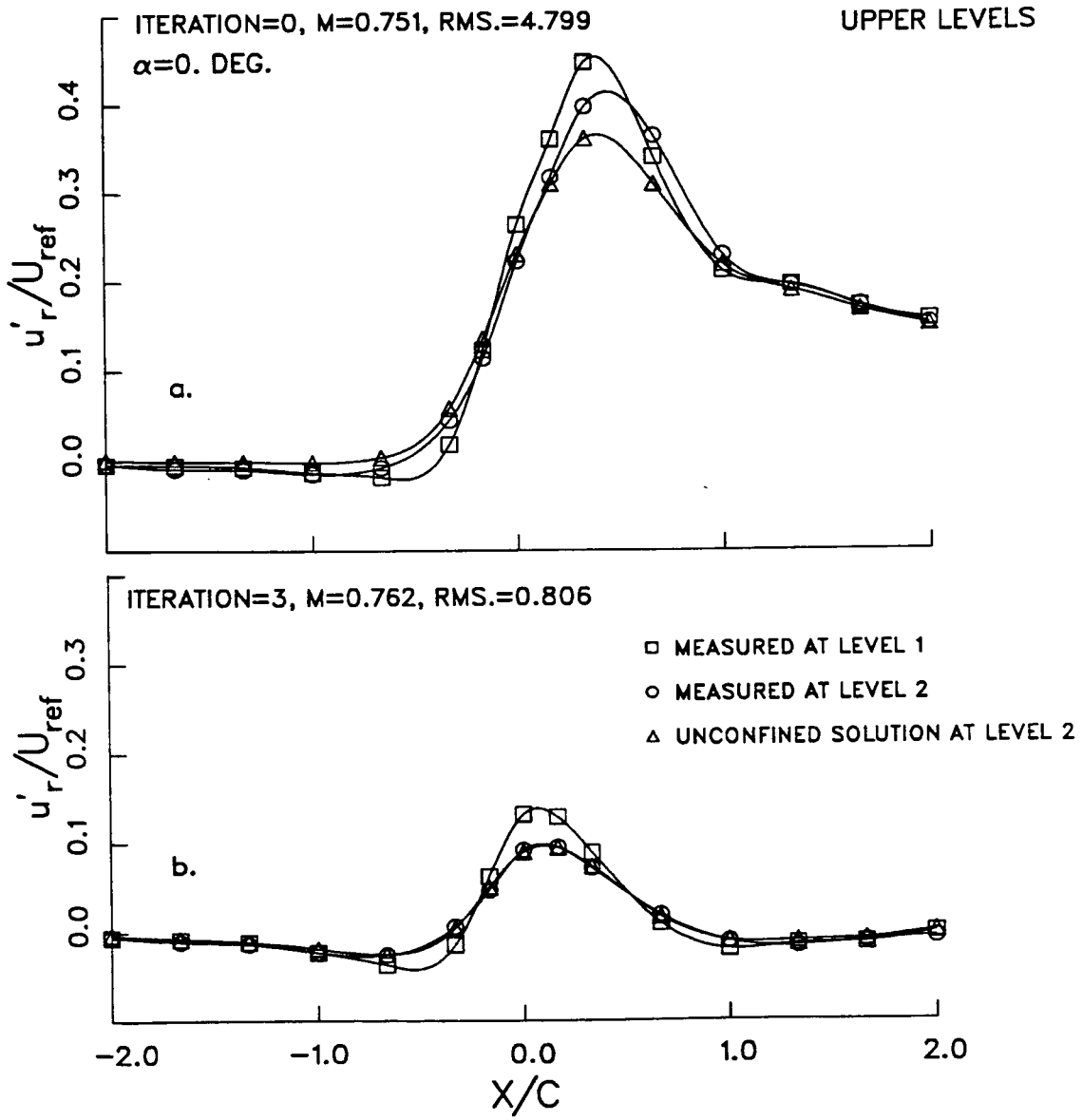

Figure 5.35: Resultant velocity distributions from side-wall pressure measurements in the subcritical nonlifting case before and after the corrections, two-level iterative method.

The comparison of the measured model pressure coefficients with the experimental data base[46] before and after the convergence, shows the drastic improvement in Figure 5.36.

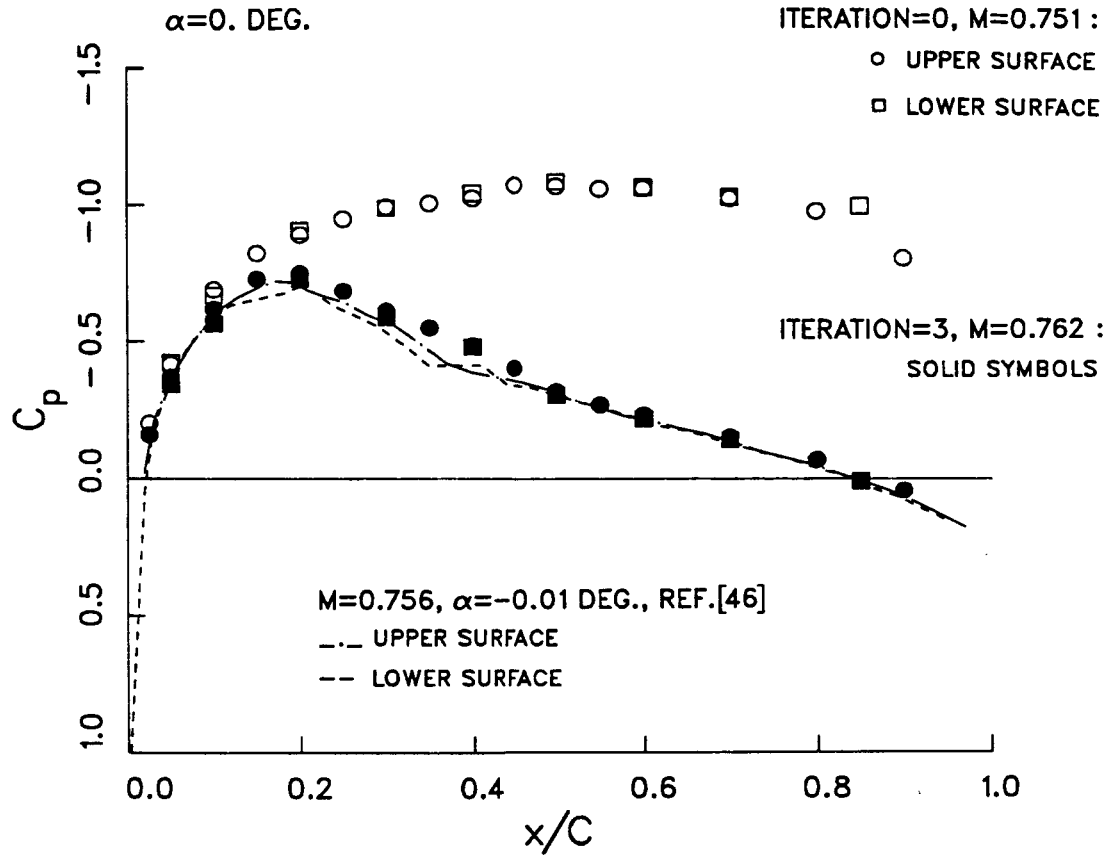

Figure 5.36: Comparison of the initial and final model pressure distributions with an experimental data base[46].

5.2.3.2 Subcritical Lifting Case

As noted before, although the influence coefficients were evaluated at one flow condition, they were used in determining the pressure corrections at different Mach numbers and model incidences. At $\alpha = 2.°$ and $M = 0.654$, the effect of wall interference initially was less severe on the model pressure coefficient (Figure 5.38) compared to the lifting case at $M = 0.7$ (Figure 5.12). In this case, excellent results

were achieved in five iterations which were carried out with side-wall pressure measurements (Figures 5.37a and 5.37b). After the final iteration, the measured model pressure distribution agrees well with the data base[48] as illustrated in Figure 5.38.

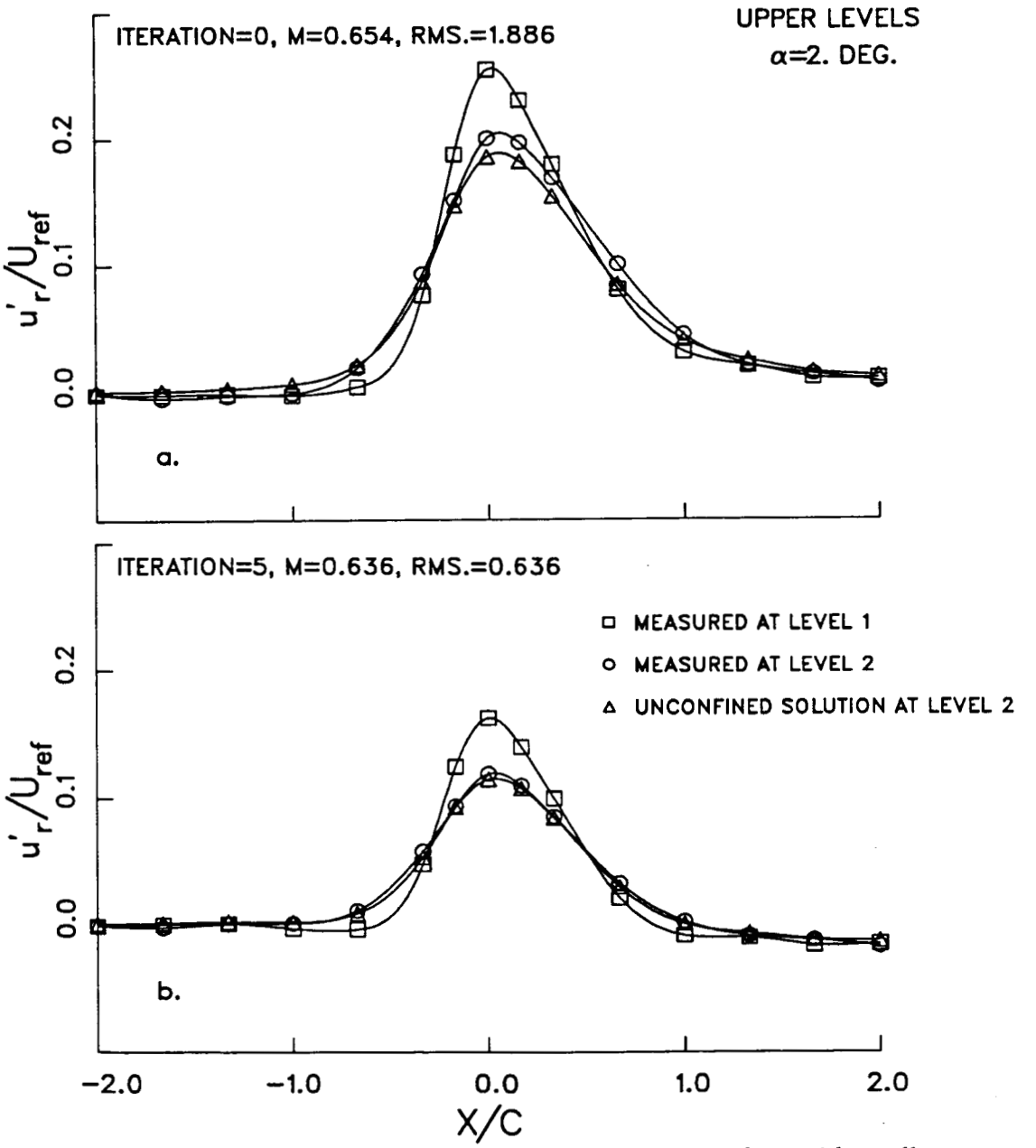

Figure 5.37: Initial and final resultant velocity distributions from side-wall pressure measurements in the subcritical lifting case, two-level iterative method.

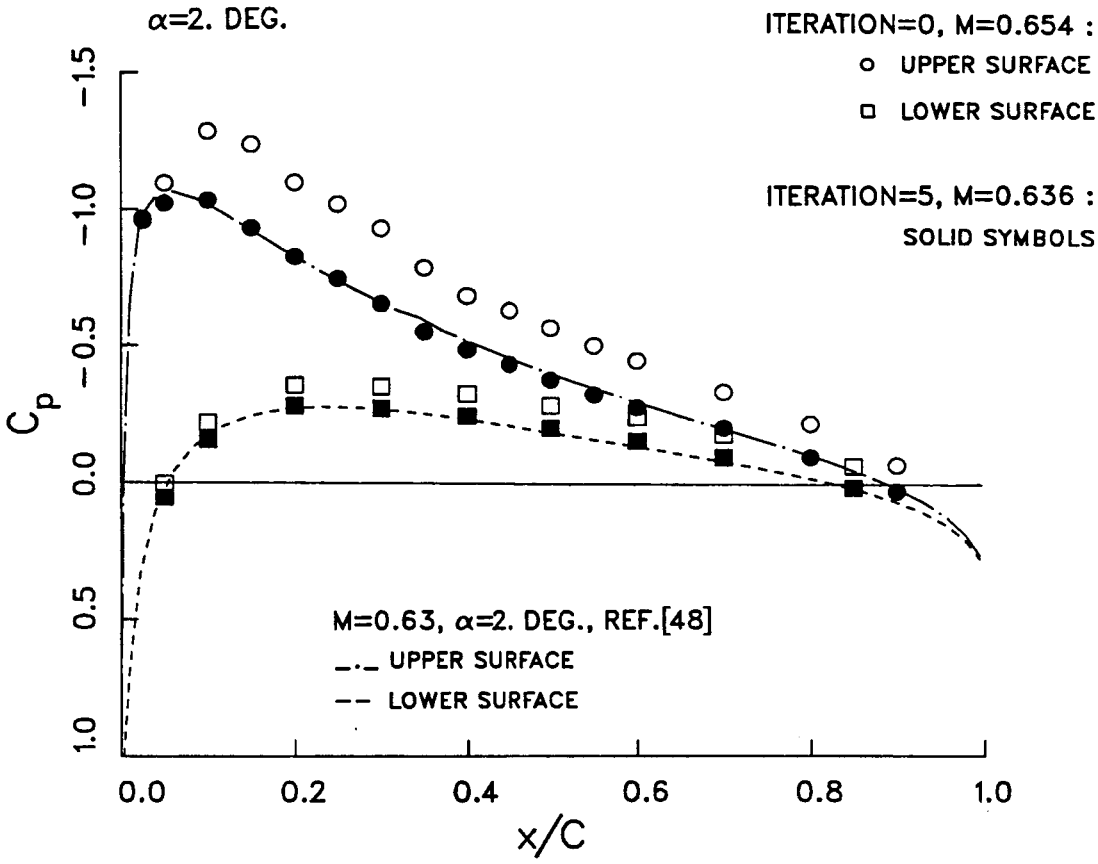

Figure 5.38: Comparison of the initial and final model pressure distributions with the computational data[48].

5.2.3.3 Subcritical Lifting Case

In one specific case, model incidence was set to the maximum $\alpha = 4.°$ and it was considered sufficiently high for the purpose of these experiments. It took six iterations to arrive at the unconfined flow conditions at $M = 0.6$ while the rms error in the velocity distribution was reduced by about 70 % (Figures 5.39a and 5.39b). The flow was supercritical on the airfoil surface. Figure 5.40 shows the initial and final measured model pressure distributions and the experimental data base[46] for comparison. In general, the agreement is good and discrepancies are attributed to the differences in the angle of attack.

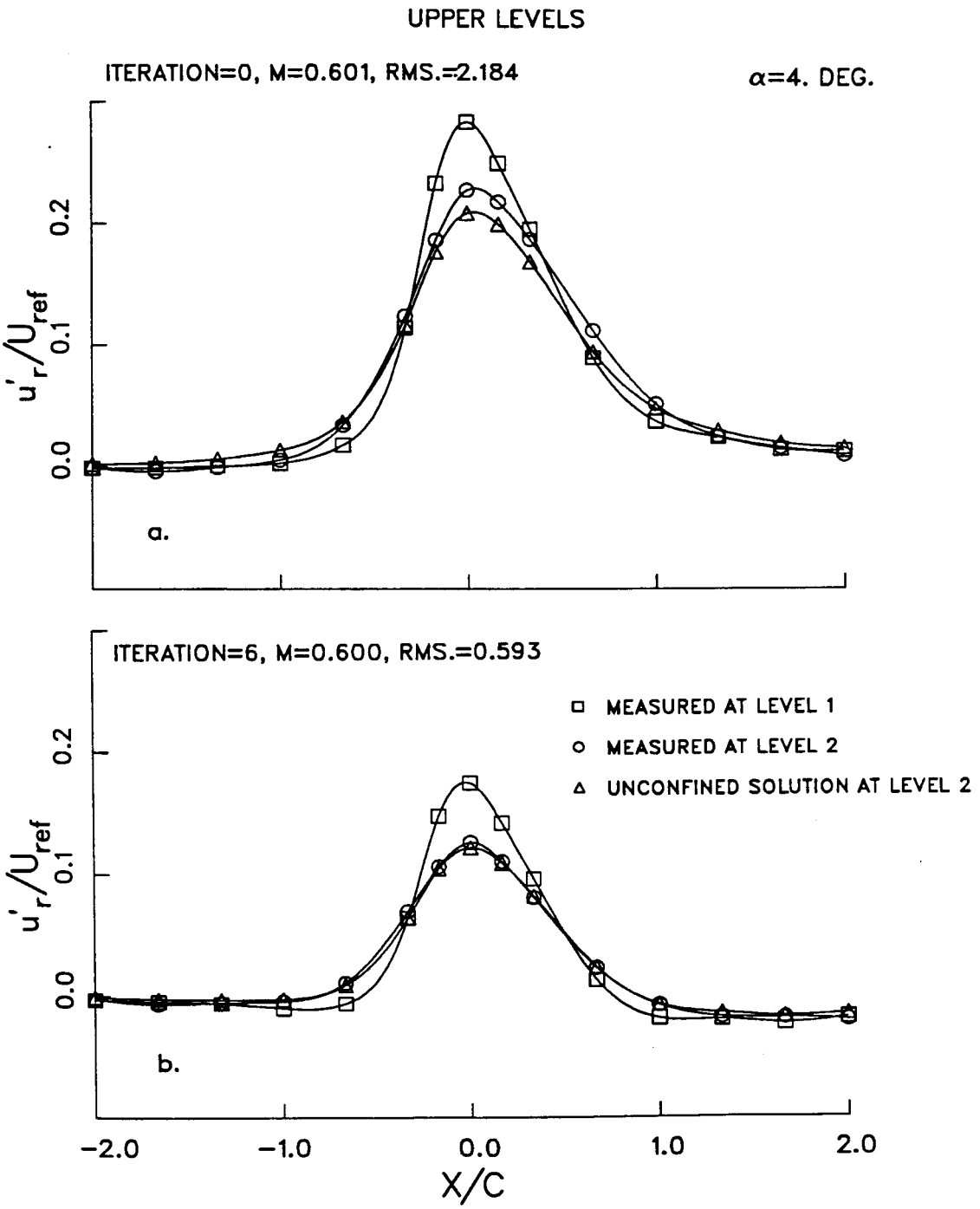

Figure 5.39: Initial and final resultant velocity distributions from side-wall pressure measurements in a subcritical lifting case, two-level iterative method.

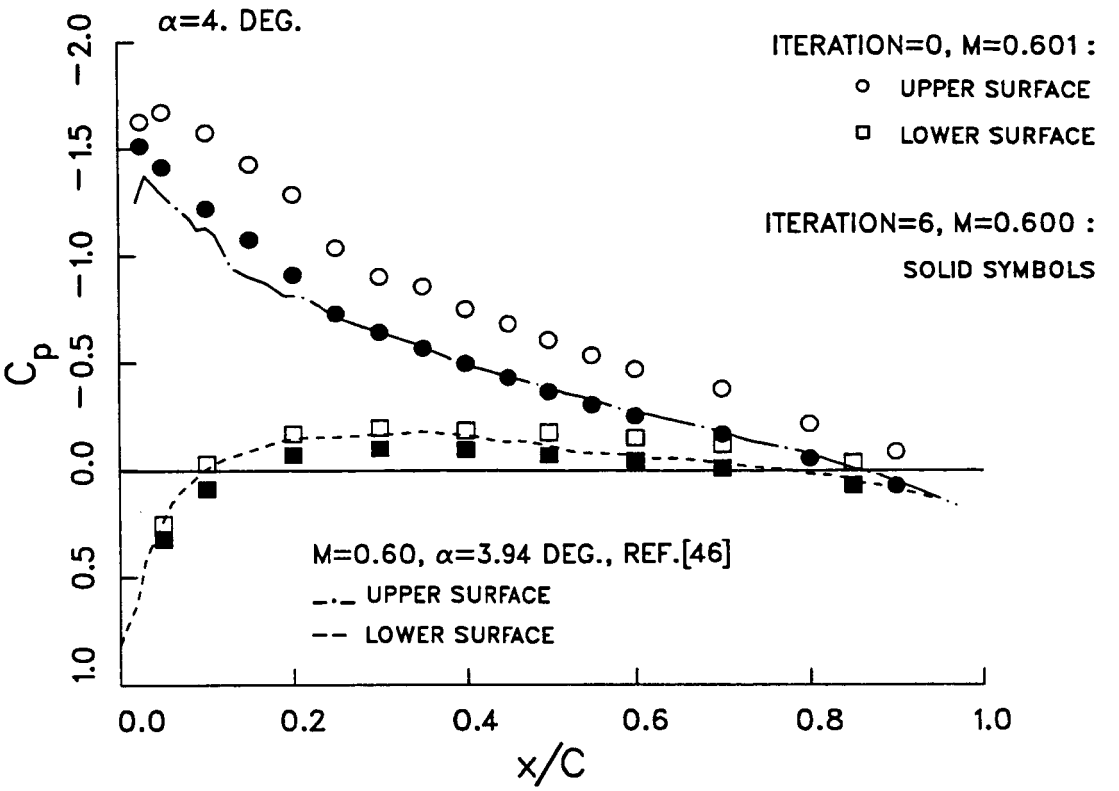

Figure 5.40: Comparison of the initial and final model pressure distributions with the ONERA data[46].

5.2.3.4 Supercritical Lifting Case

In extreme cases, such as $M = 0.7$ and $\alpha = 4.°$, wall effects were more pronounced and complete wall control could not be provided because of insufficient suction and/or blowing capability. However, to show the capabilities of the schemes with the side-wall pressure distribution in such a severe case, the iterative and the one-step schemes were implemented with the available suction and blowing. Initially, a great amount of wall interference was present as shown in Figure 5.41a. Although it was considerably reduced in five iterations, discrepancies in the velocity distribution over the quarter-chord of the model could not be eliminated because of the lack of the sufficient wall control, Figure 5.41b. There was little interference at the lower control levels and it was improved slightly as shown in Figure 5.42.

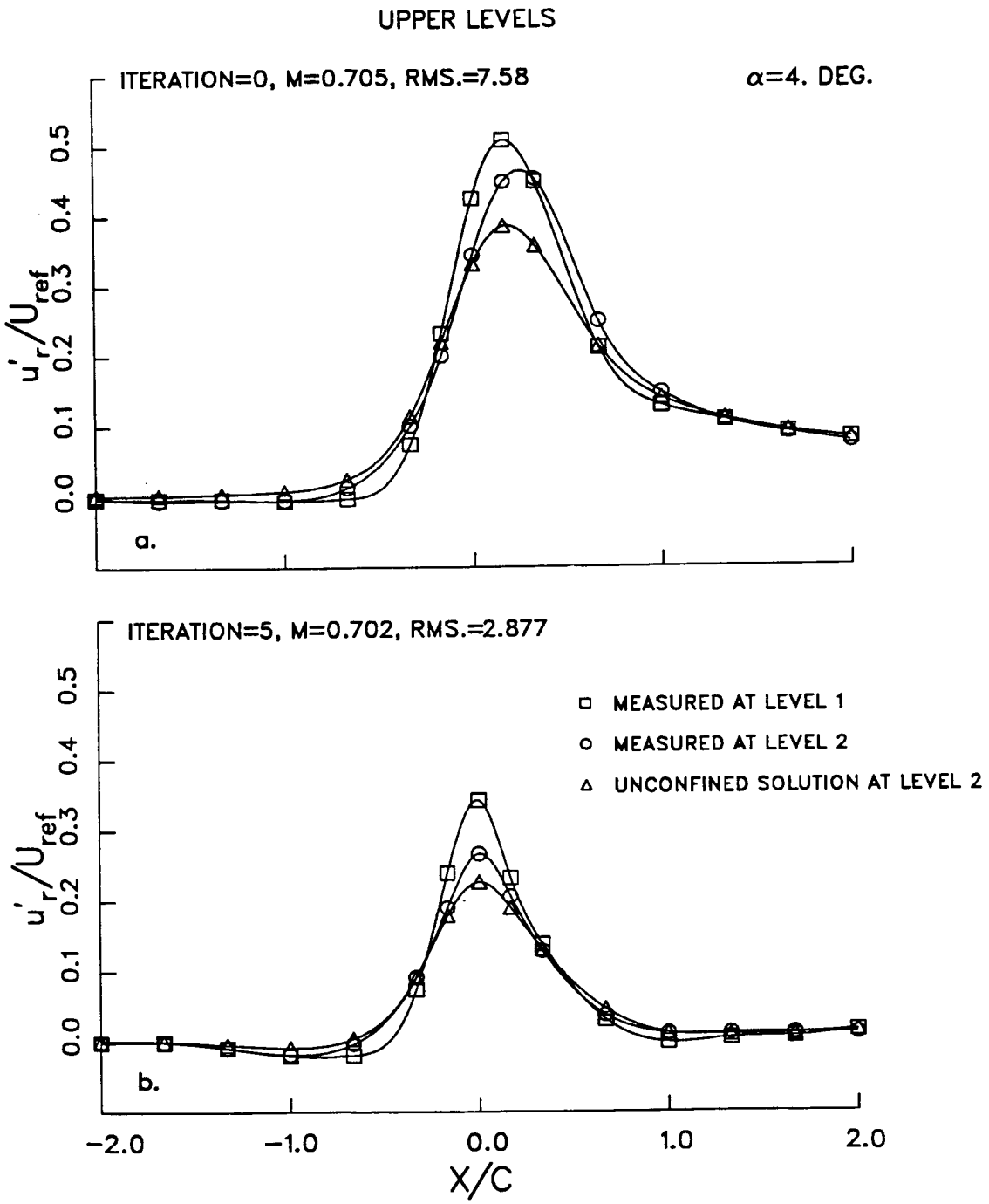

Figure 5.41: Initial and final resultant velocity distributions from side-wall pressure measurements at the upper levels in a supercritical lifting case, two-level iterative method.

The same flow conditions were obtained with both schemes after the final iteration as presented in Figures 5.43 and 5.44. The shock location on the model upper surface was moved considerably and the pressure distribution was improved on the lower surface in spite of the limited wall control and the use of the linear flow analysis.

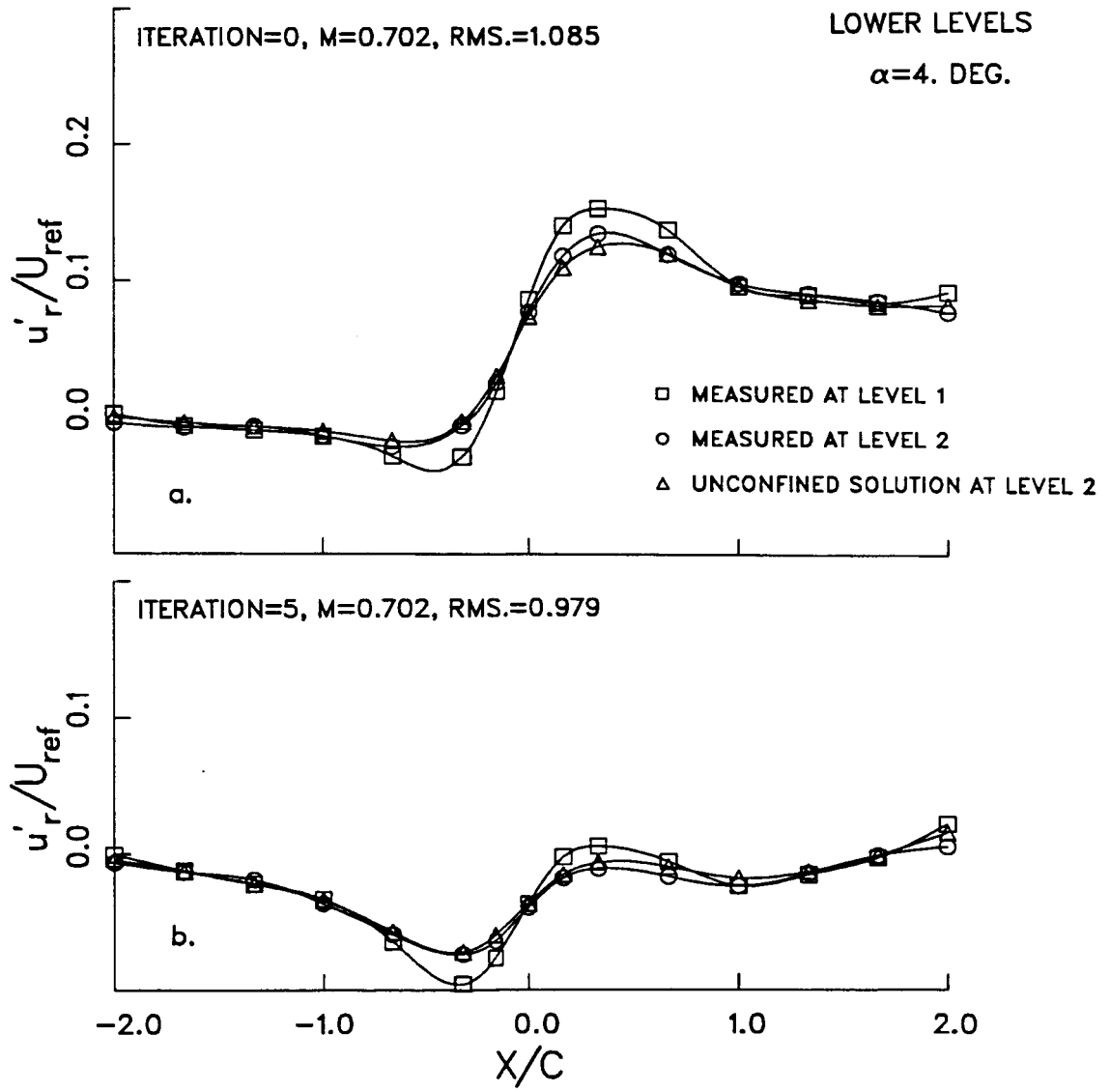

Figure 5.42: Initial and final resultant velocity distributions from side-wall pressure measurements at the lower levels in a supercritical lifting case, two-level iterative method.

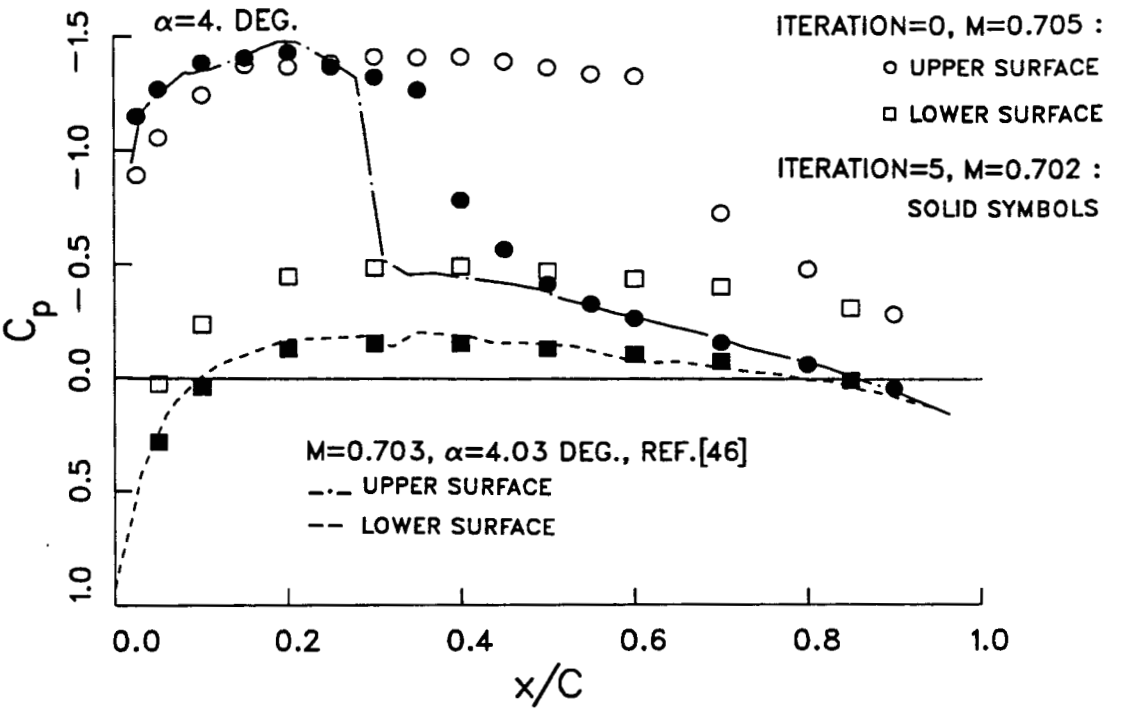

Figure 5.43: Comparison of the initial and final model pressure distributions with the ONERA data[46] _ iterative method.

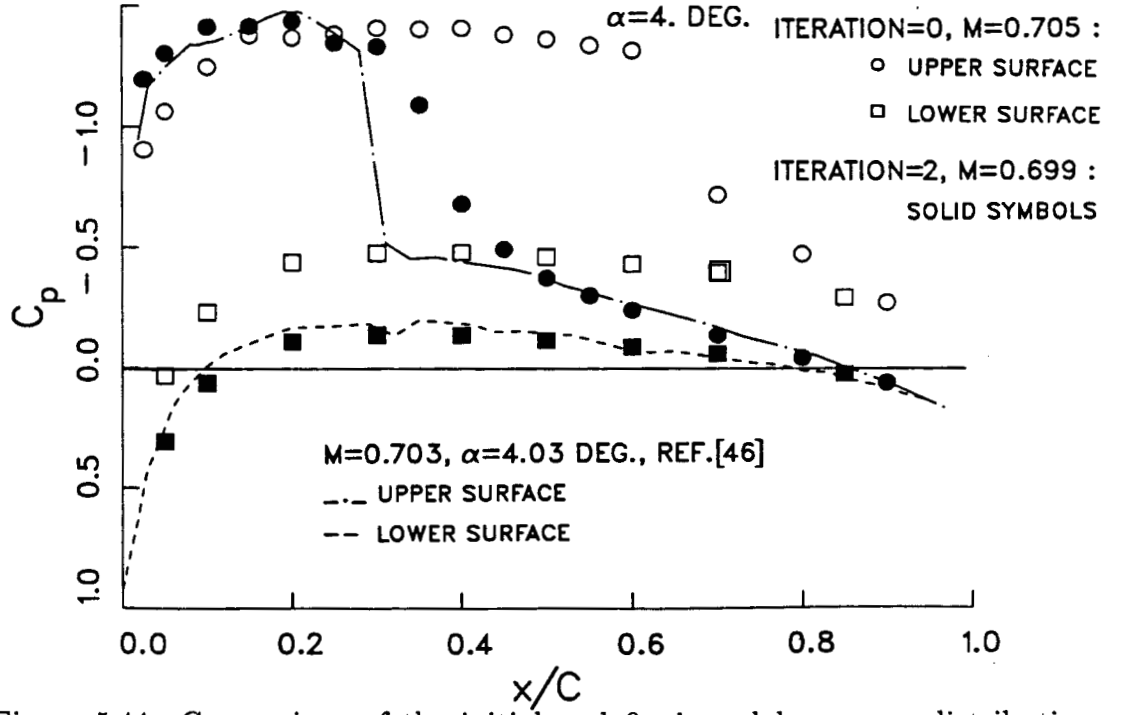

Figure 5.44: Comparison of the initial and final model pressure distributions with the ONERA data[46] _ one-step method.

Chapter 6

Comparison of the Convergence Schemes

One of the primary objectives of this study is to compare the different convergence schemes applied with different flow parameters. Based on the results presented in the preceeding chapter and the available data from other sources, comparisons made in three different categories are given in the following sections. It should be noted that the present experiments are not designed to create a data base for the pressure distributions for a NACA 0012 airfoil section. But instead, model pressure distributions were measured and compared with the other experimental and numerical data to demonstrate the consistency of the results and the applicability of the methods presented in this study. Moreover, in spite of the abundance of the experimental data on NACA 0012 airfoil, discrepancies between different wind tunnel results are not uncommon and a careful analysis is required to ensure the accuracy and quality of the data[50].

6.1 One-Level versus Two-Level Convergence Scheme

First, results from the applications of the one-level method[15] and the two-level method[26] will be compared at similar flow conditions. Figure 6.1 illustrates the comparison of the measured model pressure distributions after the final corrections.

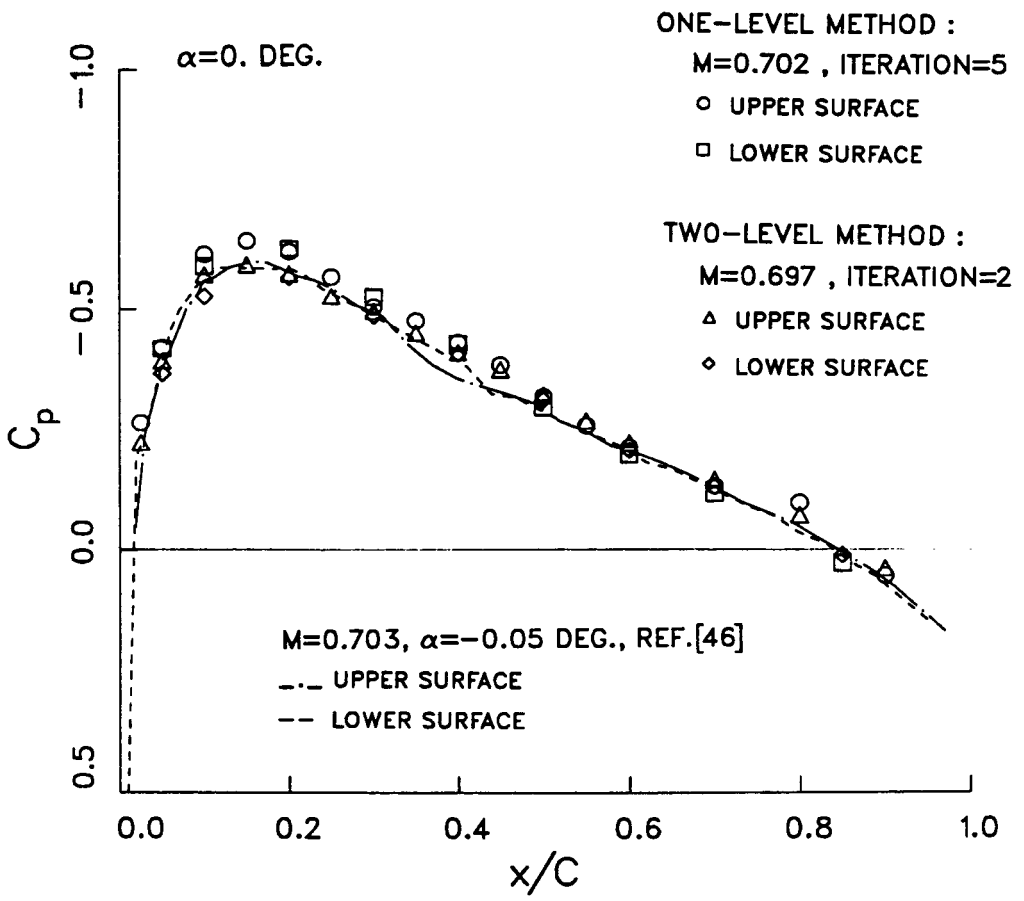

Figure 6.1: Comparison of the model pressure coefficients from the application of the one-level and the two-level iterative methods and with the ONERA data[46].

Both methods were applied iteratively in this nonlifting case, and similar pressure coefficients were obtained except at the regions between 10 % and 30 % of the chord. This discrepancy is partly due to the imperfect matching of the velocity distributions at the control level (Figure 5.25b). The maximum difference between the two pressure coefficients is about 0.06 (relative maximum variation=12 %, average

distribution while both velocity components were required in the one-level method. In the application of the one-level method, the number of iterations is considerably higher compared to the other method. Both results were also compared with experimental data[46] in which height/chord ratio is 3.71 and $Re = 3.79$ x 10^6. In the present experiments, height/chord=1.44 and $Re \sim 10^6$. The pressure distribution from the two-level method is found to be in good agreement with the data base.

6.2 Convergence Schemes with Streamwise Velocity versus those with Side-Wall Pressure Distribution

Side-wall pressure distribution was used as the flow variable in the application of the adaptive-wall concept to simplify the instrumentation and to reduce the testing time. To demonstrate the feasibility of this approach, the iterative and the one-step convergence schemes were applied using both streamwise velocity and side-wall pressure distributions. The results presented in Chapter 5, have shown that the two-level compatibility assessment method can be successfully applied with the side-wall pressure distribution and converges to unconfined flow conditions.

Supercritical Lifting Case, ($M \sim 0.7, \alpha = 2.°$)

In Figure 6.2, the comparison of the measured model pressure distributions shows the consistency of the results from both applications in the supercritical lifting case. Both experiments were conducted at about the same Mach number and angle of attack. Although the number of iterations is higher in the experiments with the side-wall pressure measurements, the testing time for each iteration was about 5 and 10 times shorter, in nonlifting and lifting cases respectively, compared to the experiments with the LDV measurements (based on same number of control points including on-line analysis and adjustment of the plenum pressures).

Both pressure measurements were compared with the data from the Calspan 8-foot tunnel ($Re = 10^6$ and transition strip at x/c=0.10 at the leading edge). Although it was taken at a slightly higher Mach number, it provides a good comparison for our purpose. The shock location seems to be in good agreement and boundary layer trip is probably the cause of the local separation and the lower pressure coefficient at the leading edge.

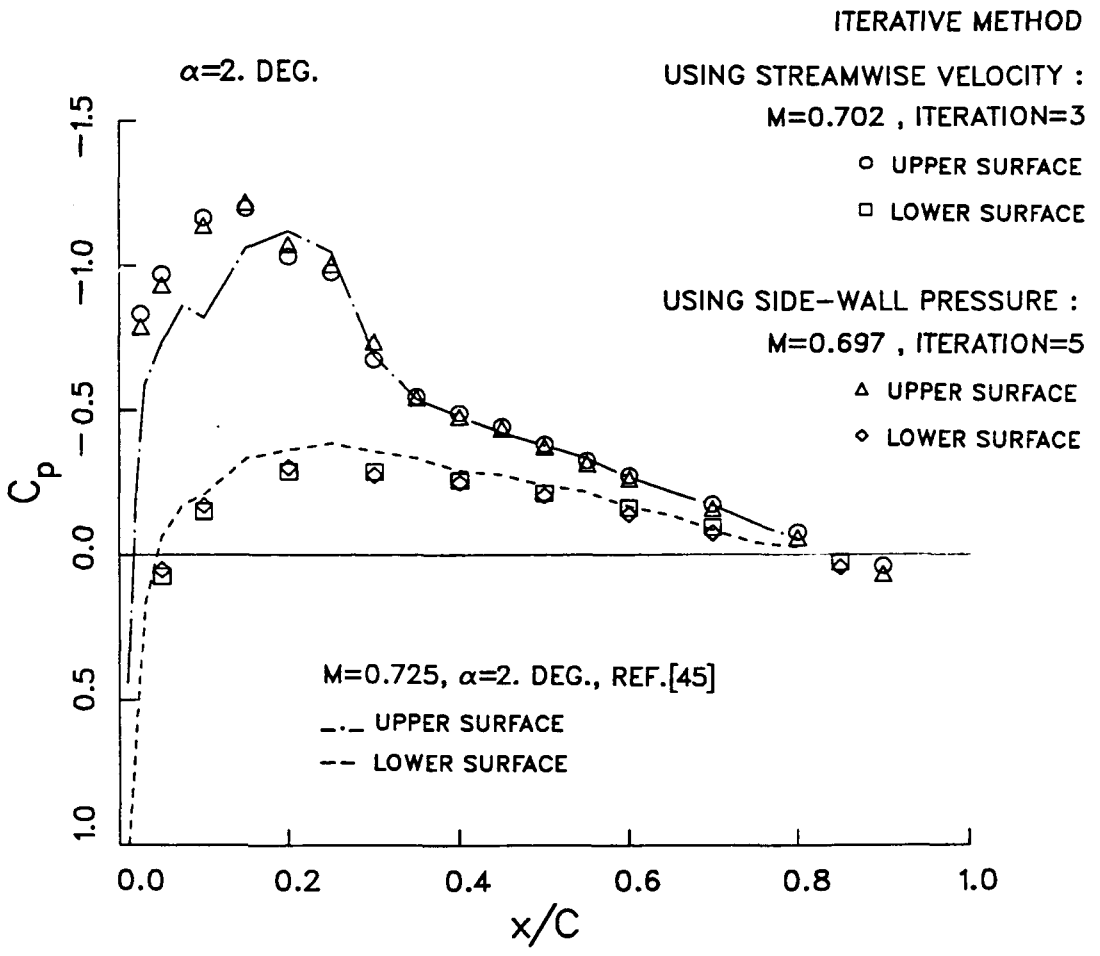

Figure 6.2: Comparison of the model pressure coefficients obtained from the application of the iterative methods using the streamwise velocity and the side-wall pressure.

Another comparison is given in Figure 6.3 for the same results with other data taken in the NASA Langley 0.3 meter cryogenic adaptive wind tunnel[51]. This tunnel has a flexible-wall test section and the presented data was taken at M=0.70 and Re=3.02 10^6. Model angle of attack was given as 1.976° and it has a boundary layer trip at x/c=0.05 . In this case, the model incidence is slightly smaller and shock location is nearer the leading edge compared to our data. However, top and bottom pressure coefficients are found to be in good overall agreement.

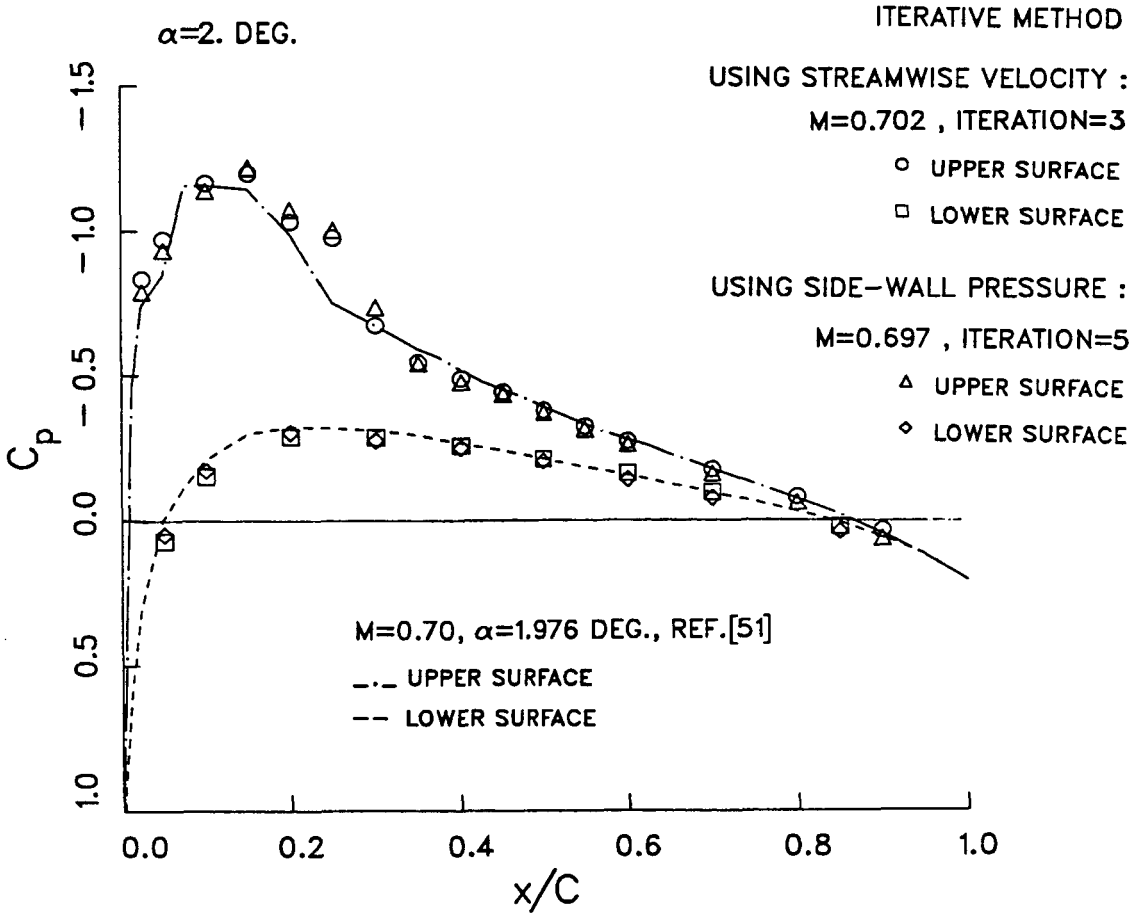

Figure 6.3: Comparison of the model pressure coefficients obtained from the application of the iterative methods using the streamwise velocity and the side-wall pressure, and with the LANGLEY flexible-wall adaptive wall data[51].

Subcritical Lifting Case, ($M \sim 0.65, \alpha = 2.°$)

Model pressure distributions taken at similar Mach numbers (M=0.649 for the experiments with streamwise velocity distribution and M=0.636 for the side-wall pressure measurements) are compared in Figure 6.4 . It can be seen that the pressure measurements for the lower surface are in good agreement, but the data on the upper surface differ, especially at the leading edge (the maximum difference=0.136, relative maximum variation$\sim$ 14 %, average variation on the upper surface$\sim$ 7 %).

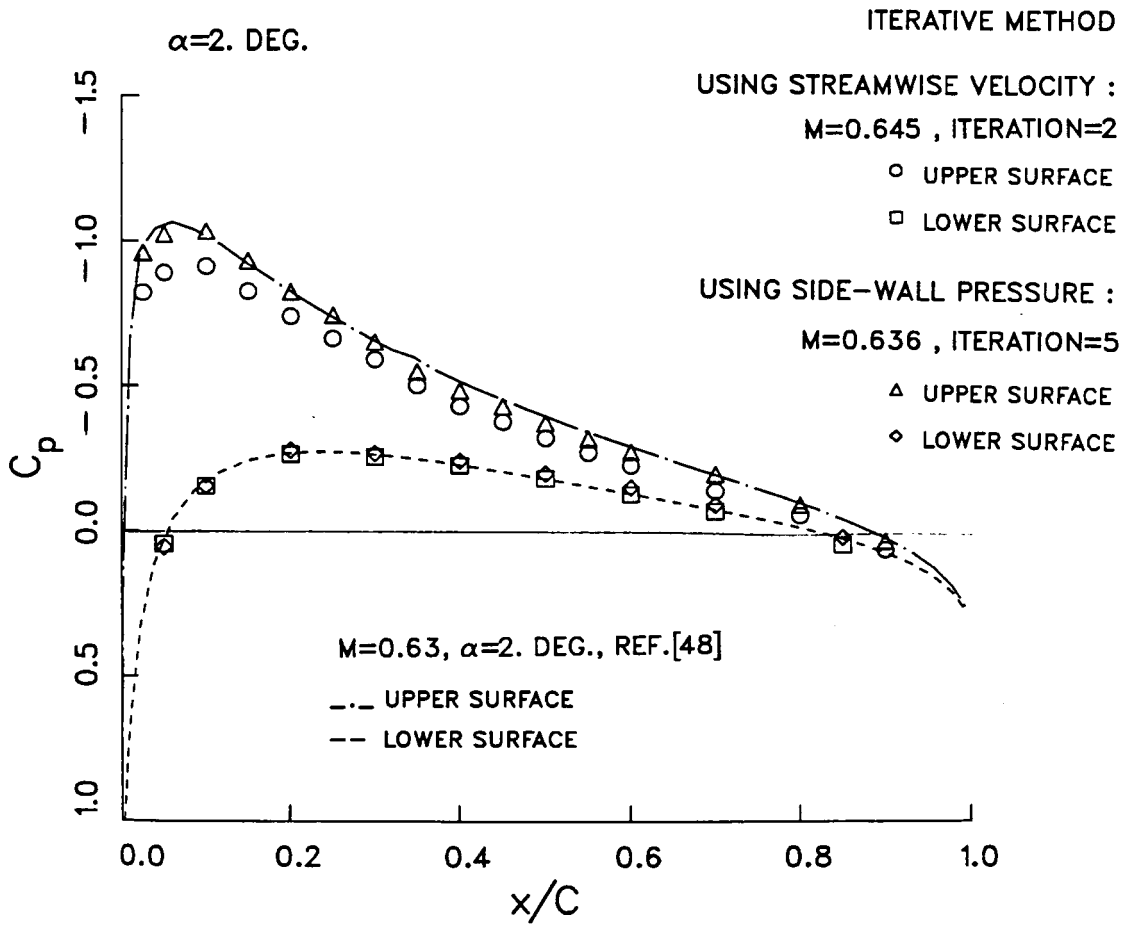

Figure 6.4: Comparison of the model pressure coefficients obtained from the application of the iterative methods using the streamwise velocity and the side-wall pressure and with the computational data[48].

The experiments with the side-wall pressure distribution showed a perfect matching in the velocity distributions as shown in Figure 5.37 . A good convergence was also achieved in the application of the iterative scheme using the streamwise velocity. The discrepancies may be due to the slight differences in the setting of the model incidence. The present data are compared with the exact solution by Sells as reported by Lock[48] in Figure 6.4 and with the experimental data from the Calspan 8-foot tunnel[45] in Figure 6.5 . The discrepancies are attributed to the differences in the Mach number, and the angle of attack.

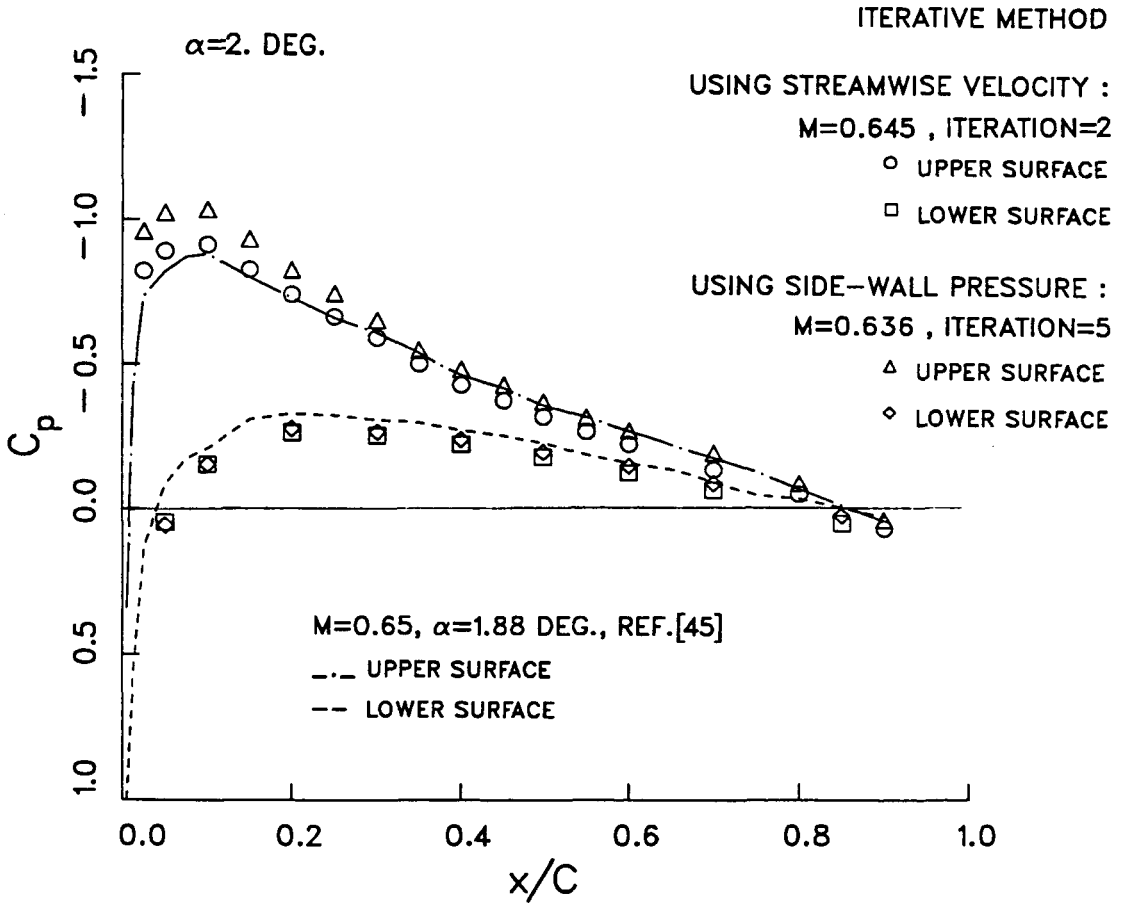

Figure 6.5: Comparison of the model pressure coefficients obtained from the application of the iterative methods using the streamwise velocity and the side-wall pressure and with the CALSPAN data[45].

6.3 Iterative Scheme versus One-Step Scheme

The purpose of the one-step method is to obtain the unconfined flow conditions in a single iteration if possible, or otherwise to minimize the number of iterations. Experiments were conducted to demonstrate the relative merits of the iterative scheme and the one-step convergence scheme introduced in this study.

Subcritical nonlifting case with streamwise velocity

In Figure 6.6, the comparison of the measured model pressure distributions from the experimental iterative and one-step convergence schemes shows that similar results were achieved in one iteration.

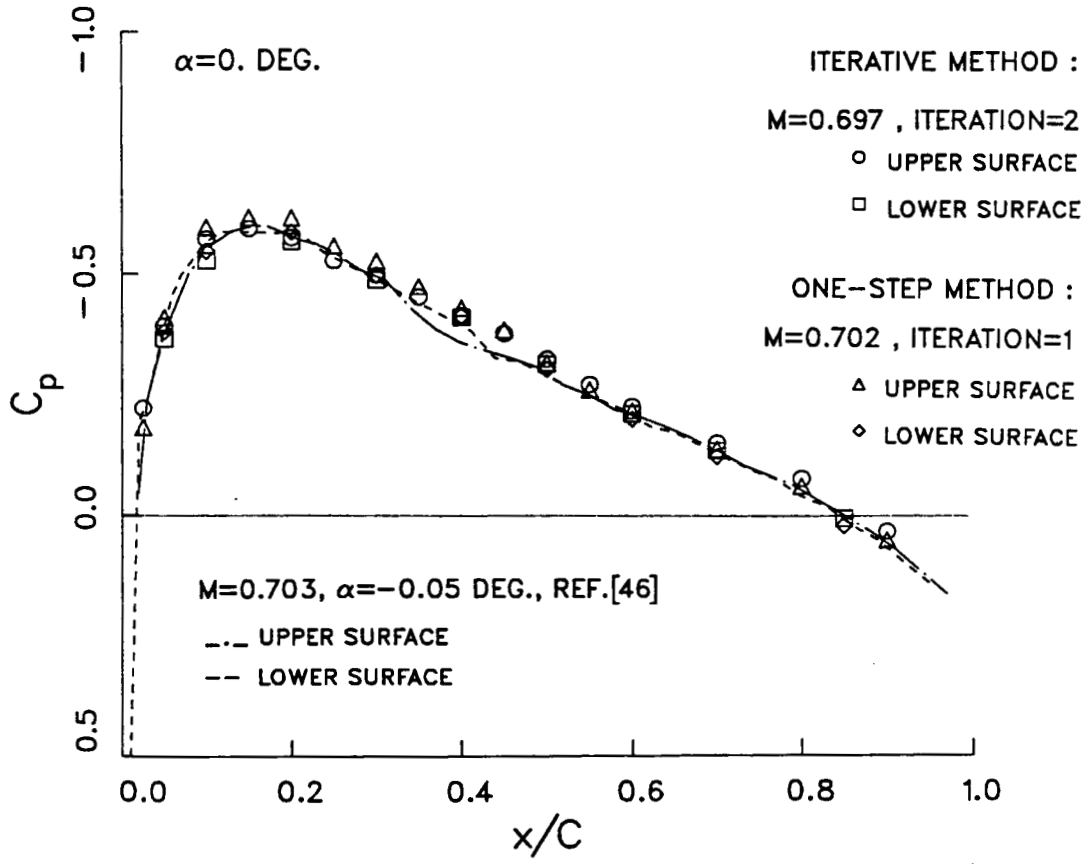

Figure 6.6: Comparison of the model pressure coefficients obtained from the application of the iterative and the one-step methods using the streamwise velocity.

Experiments were carried out at $M \sim 0.7$ and at zero angle of attack. Aside from the slight variations caused by the differences in the Mach numbers, the model pressure coefficients after the final iterations are found to be in good agreement. The present pressure data is also compared with the experimental data from ONERA[46] in Figure 6.6 and with the data taken in the NASA Langley 8-foot transonic pressure tunnel[49] in Figure 6.7. The ONERA data which was discussed previously is usually in good agreement with the present results in spite of the small discrepancies.

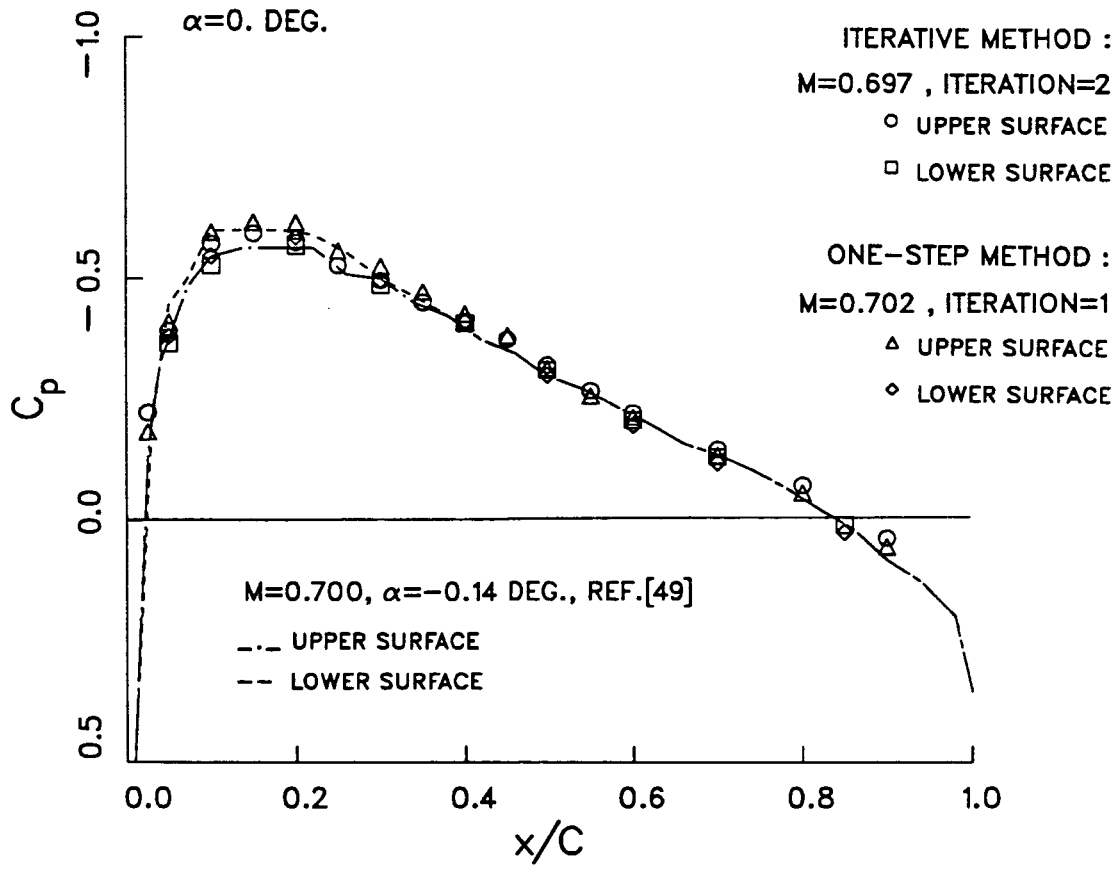

Figure 6.7: Comparison of the model pressure coefficients obtained from the application of the iterative and the one-step methods using the streamwise velocity.

The variation between the upper and the lower surface pressure coefficients at $0.10 \leq x/c \leq 0.30$ in Harris' data[49] in Figure 6.7 would probably stem from the differences in the angle of attack (Re$\sim$ 3.0 x 10^6 in both data base). Otherwise, the present pressure data agrees reasonably well with Harris' data over the rest of the chord length.

Subcritical Nonlifting Case with Side-Wall Pressure Distribution

In this case, the iterative and the one-step convergence schemes were applied using the side-wall pressure distribution at slightly higher Mach numbers compared to the previous example. Experiments with both schemes produced similar pressure coefficients as illustrated in Figure 6.8 . As seen from the comparison, convergence to the unconfined flow was achieved in one iteration using the one-step method while three iterative steps were required to arrive at the same conditions using the iterative convergence scheme. The small discrepancies could possibly stem from the differences in the Mach numbers. Experimental data was compared with the numerical solution reported by Lock[48]. The comparison is reasonably good over the entire chord length. Lock's data in general is in good agreement with the Calspan data[45] (M=0.725, $\alpha = 0.°$) although it was not presented here.

Supercritical Lifting Case with Side-Wall Pressure Distribution

Experiments using the one-step convergence scheme did not produce the same results in one iteration, however the effect of the wall interference on the model pressure distribution was greatly reduced as seen in Figure 6.9 . The pressure coefficient is slightly higher in the region $0.025 \leq x/c \leq 0.30$ and the shock position is about 5 % further downstream compared to the iterative case. Imperfect matching in the velocity distributions (Figure 5.20b) in the same region is probably the main reason for the discrepancy. One more iteration would yield similar results to those obtained using the iterative scheme. Although unconfined flow conditions could not be achieved in one iteration, the number of iterations was reduced drastically compared to the iterative method. In Figure 6.9, the Calspan data is included for comparison with the measured model pressure distributions.

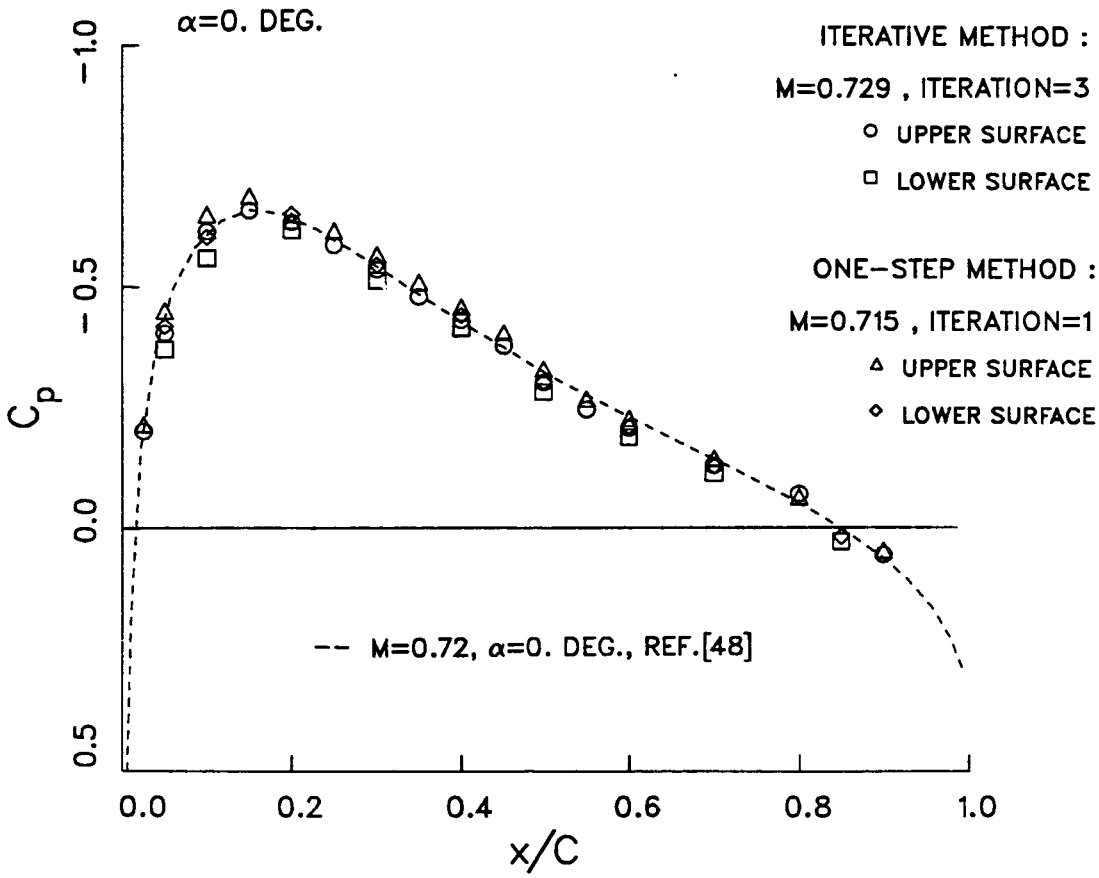

Figure 6.8: Comparison of the model pressure coefficients obtained from the application of the iterative and the one-step methods using the side-wall pressure.

Supercritical Lifting Case with Side-Wall Pressure Distribution

At M=0.7 and $\alpha = 4°$, wall interference effects were severe and the available wall control was not sufficient to provide the necessary adjustments. However, the iterative and the one-step convergence schemes were applied with the available wall control. In Figure 6.10, the comparison of the model pressure coefficients demonstrates the ability of the one-step method to produce similar corrections in fewer

iterations compared to the iterative scheme. Results are also compared with experimental data[46]. Except for the shock locations, the present data is in agreement with the experimental data from ONERA. The discrepancy is obviously dependent on the incomplete wall corrections in the present experiments.

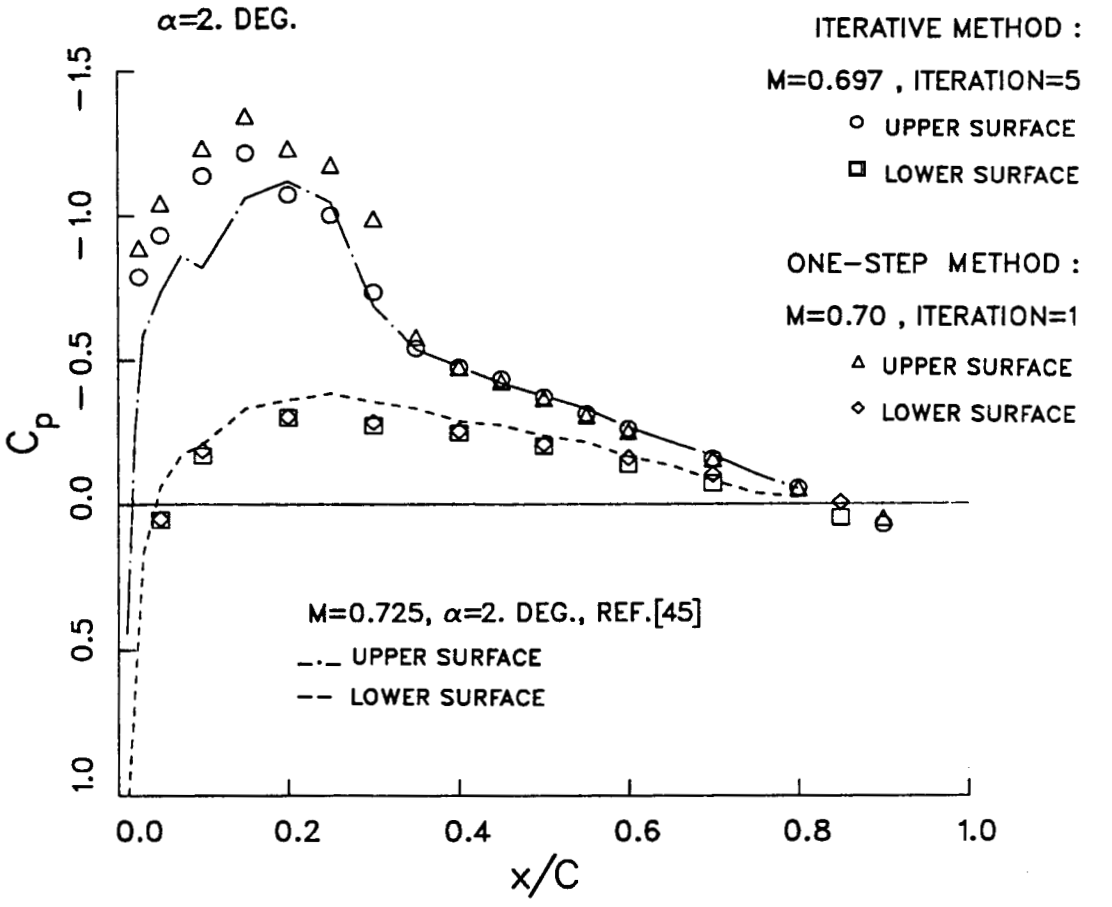

Figure 6.9: Comparison of the model pressure coefficients obtained from the application of the iterative and the one-step methods using the side-wall pressure.

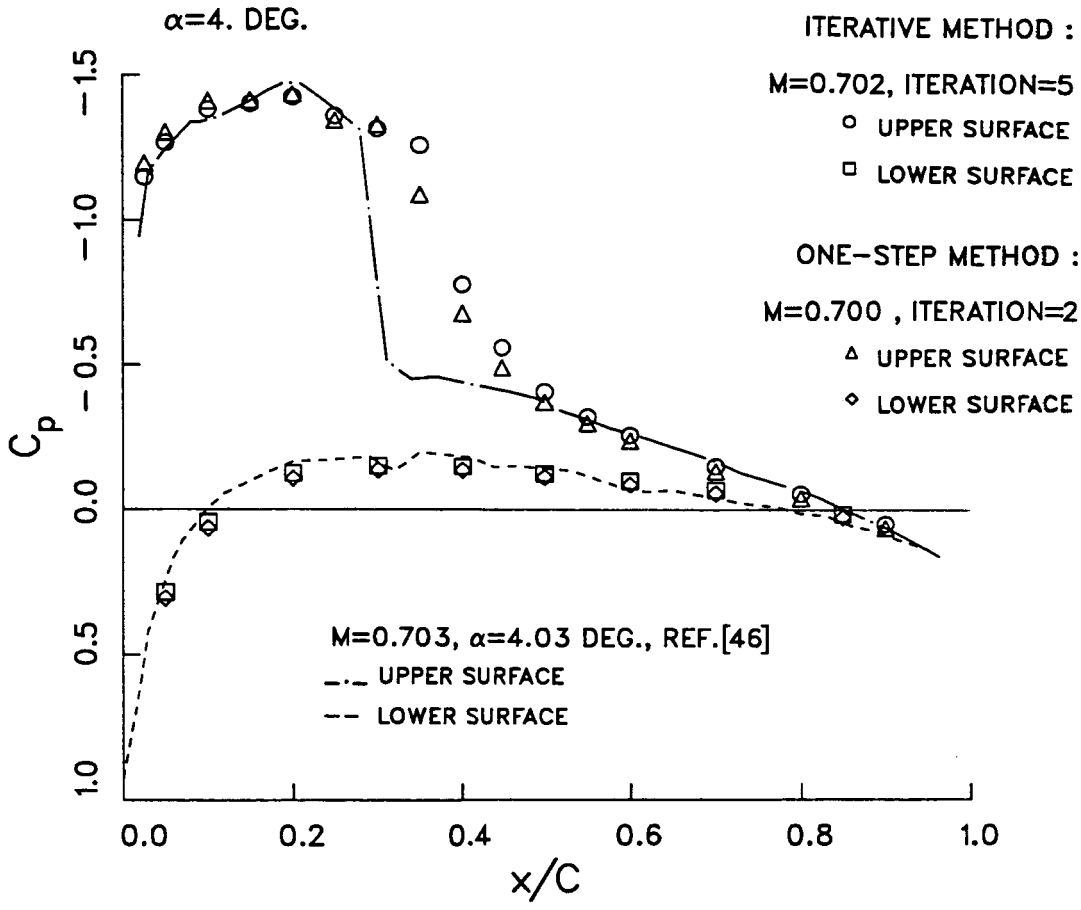

Figure 6.10: Comparison of the model pressure coefficients obtained from the application of the iterative and the one-step methods using the side-wall pressure.

6.4 Testing Time Comparisons

In this section, a comparison of the typical testing times in the application of the convergence schemes is given to determine the relative time efficiency of the preferred technique, the one-step convergence scheme using the side-wall pressure.

Testing time for each iteration depended mostly on the measurement technique.

Velocity measurements using the LDV system usually took about 20 minutes for a nonlifting case (a total of 30 control points at two control levels) and about 40 minutes for a lifting case. For a lifting case, velocity measurements had to be taken in the upper and lower control levels since the flow was not symmetrical with respect to the model. Collection of the LDV data consisted of data taking, processing and moving the LDV system along the control levels. Side-wall pressure measurements and data processing took about 1 minute regardless of model configuration. Application of the pressure corrections in the plenum compartments contributed an average of 5 minutes while the calculation of unconfined flow and pressure corrections were negligible, about 0.1 minute.

In a typical application using the iterative method, the total testing time after three iterations was about 75 minutes using the LDV system. The same application using the side-wall pressure measurements took about 18 minutes, reducing the total testing time by a factor of approximately 5. Application of the one-step convergence scheme took approximately 8 minutes using the side-wall pressure measurements, which reduced the total testing time by a factor of approximately 10.

Chapter 7

Conclusions and Recommendations

7.1 Conclusions

A fast and reliable method for the elimination of the wind tunnel wall interference effects has been demonstrated. The main conclusions that have been arrived at in connection with the use of this method are as follows:

1. The experiments demonstrated that it is feasible to use the side-wall pressure distribution as a flow variable in the adaptive-wall convergence schemes. The measurement technique requires simple instrumentation and reduces total testing time considerably. The convergence schemes applied using the side-wall pressure yielded accurate and consistent results. Measurements of the model pressure distributions agree well with the other experimental and computational data.

2. Existence of linear influence coefficients independent of Mach number and presence of the model permits a fast correction scheme. Influence coefficient matrices, which were constructed using the superposition principle, could be used to determine the pressure corrections at different Mach numbers, with and without lift.

3. The use of the less complicated side-wall pressure instrumentation instead

of the LDV measurement of velocity was found to reduce the testing time by a factor of approximately five. The one-step method of adapting the wall conditions to satisfy interference-free flow, using either the streamwise velocity or the side-wall pressure, further reduces the testing time by a further factor of two to three when compared to the iterative scheme.

4. The adaptive-wall corrections determined by using the linearized flow equations provided sufficient control to achieve convergence to interference-free flow for both the subcritical and mildly supercritical flows.

7.2 Recommendations

The recommendations for the future regarding adaptive-wall experiments are as follows:

1. The use of influence coefficients should be further investigated to determine the limits of their applicability in the case of highly supercritical flows for which shock waves may extend to the tunnel walls.

2. Automated control of suction and blowing to the plenum compartments should be incorporated for production testing in order to obtain faster, more precise wind tunnel wall adaptation.

3. The number of plenum compartments should be increased especially over the region near the model to improve flow control.

Appendix A

Numerical Evaluation of the Cauchy Integral

This section shows the removal of the singularity in the numerical evaluation of the Cauchy integral. On a singular strip:

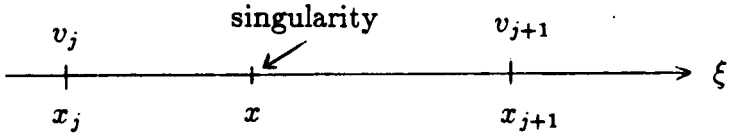

The Cauchy integral equation for the evaluation of the streamwise disturbance velocity is given as:

$$u(x,\eta) = -\frac{1}{\pi\beta} \oint_{-\infty}^{+\infty} \frac{v(\xi,\eta)d\xi}{\xi - x}$$

Define $l_j = x_{j+1} - x_j$ and $\xi = x - x_j$.

Assume that the normal disturbance velocity along the singular strip varies linearly as a function of ξ, that is;

$$v(\xi,\eta) = a\xi + b$$

The coefficients a and b can be evaluated using the boundary conditions given at the ends of the strip. They are given as follows;

at $\xi = x_j \quad v = v_j$ and at $\xi = x_{j+1} \quad v = v_{j+1}$

Then;

$$a = \frac{v_{j+1} - v_j}{x_{j+1} - x_j}$$

$$b = v_j - \frac{v_{j+1} - v_j}{x_{j+1} - x_j} x_j$$

Hence, the functional relation for the normal velocity can be expressed as:

$$v(\xi, \eta) = v_j + \frac{v_{j+1} - v_j}{l_j}(\xi - x_j)$$

Substituting this equation into the Cauchy integral equation, the following expression is obtained:

$$u(x, \eta) = -\frac{1}{\beta\pi}\left\{\int_0^{l_j}\left[v_j + \frac{v_{j+1} - v_j}{l_j}(x - x_j)\right]\frac{d\xi}{\xi - x} + \int_0^{l_j}(\frac{v_{j+1} - v_j}{l_j})d\xi\right\}$$

At the singular point, a limiting value can be found about a circle assuming its radius, ϵ, goes to zero while ξ approaches x. Then, the equation above can be written as:

$$u(x, \eta) = -\frac{1}{\beta\pi}\left\{\int_0^{l_j}\left(v_j + \frac{v_{j+1} - v_j}{l_j}(x - x_j)\right)\left(\lim_{\epsilon \to 0}(\int_0^{x-\epsilon}\frac{d\xi}{\xi - x} + \int_{x+\epsilon}^{l_j}\frac{d\xi}{\xi - \epsilon})\right) + \frac{v_{j+1} - v_j}{l_j}\int_0^{l_j} d\xi\right\}$$

As a result, the velocity about the singularity on the singular strip can be determined using the following nonsingular equation:

$$u(x_s, \eta) = -\frac{1}{\beta\pi}\left[\left(v_j + \frac{v_{j+1} - v_j}{l_j}(x - x_j)\right)\ln(\frac{l_j - x}{x}) + (v_{j+1} - v_j)\right]$$

Appendix B

Transonic Small Disturbance Equation

In this section, a finite difference formulation for the solution of the transonic small disturbance equation using Murmon-Cole method will be given. The transonic small disturbance equation can be written in the following form by applying the Murman-Cole scheme:

$$(1-\mu_{i,j})A_{i,j}\frac{D_{xx}}{\Delta x^2}\phi_{i,j}+\mu_{i-1,j}A_{i-1,j}\frac{D_{xx}}{\Delta x^2}\phi_{i-1,j}+\frac{D_{yy}}{\Delta y^2}\phi_{i,j}=0$$

where

$$A_{i,j}=1-M_\infty^2-(\gamma+1)\frac{M_\infty^2}{q_\infty}\frac{\phi_{i+1,j}-\phi_{i-1,j}}{x_{i+1,j}-x_{i-1,j}}$$

and

$$\mu_{i,j}=\begin{cases}0 & \text{if } A_{i,j}>0\\ 1 & \text{if } A_{i,j}<0\end{cases}$$

$$\frac{D_{xx}}{\Delta x^2}\phi_{i,j}=\frac{2}{(x_{i+1,j}-x_{i-1,j})}\left(\frac{\phi_{i+1,j}-\phi_{i,j}}{x_{i+1,j}-x_{i,j}}-\frac{\phi_{i,j}-\phi_{i-1,j}}{x_{i,j}-x_{i-1,j}}\right)$$

$$\frac{D_{yy}}{\Delta y^2}\phi_{i,j}=\frac{2}{(y_{i,j+1}-y_{i,j-1})}\left(\frac{\phi_{i,j+1}-\phi_{i,j}}{y_{i,j+1}-y_{i,j}}-\frac{\phi_{i,j}-\phi_{i,j-1}}{y_{i,j}-y_{i,j-1}}\right)$$

$$A_{i-1,j} = 1 - M_\infty^2 - (\gamma+1)\frac{M_\infty^2}{q_\infty}\frac{\phi_{i,j} - \phi_{i-2,j}}{x_{i,j} - x_{i-2,j}}$$

The Murman-Cole method becomes:

$$\begin{aligned}
&(1-\mu_{i,j}^n)A_{i,j}^n \frac{2}{(x_{i+1,j} - x_{i-1,j})}\left(\frac{\phi_{i+1,j}^n - \phi_{i,j}^{n+1}}{x_{i+1,j} - x_{i,j}} - \frac{\phi_{i,j}^n - \phi_{i-1,j}^{n+1}}{x_{i,j} - x_{i-1,j}}\right) \\
&+\mu_{i-1,j}^n A_{i-1,j}^n \frac{2}{(x_{i,j} - x_{i-2,j})}\left(\frac{\phi_{i,j}^{n+1} - \phi_{i-1,j}^{n+1}}{x_{i,j} - x_{i-1,j}} - \frac{\phi_{i-1,j}^{n+1} - \phi_{i-2,j}^{n+1}}{x_{i-1,j} - x_{i-2,j}}\right) \\
&+\frac{2}{(y_{i,j+1} - y_{i,j-1})}\left(\frac{\phi_{i,j+1}^{n+1} - \phi_{i,j}^{n+1}}{y_{i,j+1} - y_{i,j}} - \frac{\phi_{i,j}^{n+1} - \phi_{i,j-1}^{n+1}}{y_{i,j} - y_{i,j-1}}\right) = 0
\end{aligned}$$

This equation can be arranged as follows:

$$S_5\phi_{i,j-1}^{n+1} + S_1\phi_{i,j}^{n+1} + S_4\phi_{i,j+1}^{n+1} = -S_0\phi_{i+1,j}^n - S_2\phi_{i-1,j}^{n+1} - S_3\phi_{i-2,j}^{n+1}$$

where

$$\begin{aligned}
S_1 = (1-\mu_{i,j}^n)A_{i,j}^n &\frac{2}{(x_{i+1,j} - x_{i-1,j})}\left(\frac{1}{x_{i+1,j} - x_{i,j}} + \frac{1}{x_{i,j} - x_{i-1,j}}\right) \\
&+\mu_{i-1,j}^n A_{i-1,j}^n \frac{2}{(x_{i,j} - x_{i-2,j})}\left(\frac{1}{x_{i,j} - x_{i-1,j}}\right) \\
&-\frac{2}{y_{i,j+1} - y_{i,j-1}}\left(\frac{1}{y_{i,j+1} - y_{i,j}} + \frac{1}{y_{i,j} - y_{i,j-1}}\right)
\end{aligned}$$

$$\begin{aligned}
S_2 = (1-\mu_{i,j}^n)A_{i,j}^n &\left(\frac{2}{(x_{i+1,j} - x_{i-1,j})}\right)\left(\frac{1}{x_{i,j} - x_{i-1,j}}\right) \\
-\mu_{i-1,j}^n A_{i-1,j}^n &\frac{2}{(x_{i,j} - x_{i-2,j})}\left(\frac{1}{x_{i,j} - x_{i-1,j}} + \frac{1}{x_{i-1,j} - x_{i-2,j}}\right)
\end{aligned}$$

$$S_3 = \mu_{i-1,j}^n A_{i-1,j}^n \frac{2}{(x_{i,j} - x_{i-2,j})}\left(\frac{1}{x_{i-1,j} - x_{i-2,j}}\right)$$

$$S_4 = \frac{2}{y_{i,j+1} - y_{i,j-1}}\left(\frac{1}{y_{i,j+1} - y_{i,j}}\right)$$

$$S_5 = \frac{2}{y_{i,j+1} - y_{i,j-1}} \left(\frac{1}{y_{i,j} - y_{i,j-1}} \right)$$

The numerical equations derived can easily be solved by using the Gauss-Seidel line iteration technique. The solutions of the transonic small disturbance theory are valid for small perturbations and for freestream Mach numbers only slightly different from sonic. In the present study, the computational domain does not contain the airfoil and the freestream Mach numbers do not exceed $M = 0.75$, so that the inviscid approximation and the assumption of small disturbances hold well.

Appendix C

Influence Coefficient Matrices

Plenum Com. → / Control Points ↓		PL 2	PL3	PL4	PL5	PL6	PL7	PL8	PL9
1	Suction	20.4							
	Blowing	24.8							
2	Suction	22.3	5.1						
	Blowing	43.	12.5						
3	Suction	26.3	6.						
	Blowing	56.7	22.2						
4	Suction	27.6	11.6	3.1					
	Blowing	52.8	35.7	5.					
5	Suction	29.6	17.1	4.8					
	Blowing	48.9	49.1	10.					
6	Suction	30.	16.3	11.2	2.7				
	Blowing	42.4	47.5	20.	5.9				
7	Suction	27.1	15.	13.	3.5				
	Blowing	42.	45.	26.1	10.5				
8	Suction	28.	13.3	14.8	5.7				
	Blowing	45.	41.7	24.9	21.6				
9	Suction	25.	13.6	16.6	7.9	2.4			
	Blowing	48.	40.4	25.2	29.3	8.5			
10	Suction	26.5	13.7	17.6	11.3	5.7			
	Blowing	48.5	40.8	24.7	30.	16.6			
11	Suction	26.2	14.5	19.4	15.3	10.9	12.4		
	Blowing	44.2	42.7	23.6	28.4	25.	14.		
12	Suction	26.4	14.7	17.5	13.5	10.7	23.4	6.8	
	Blowing	40.4	39.9	24.	25.1	27.7	23.8	16.8	
13	Suction	27.	14.9	16.5	9.7	8.8	28.3	11.8	
	Blowing	39.	36.	24.2	20.7	19.6	35.	19.8	
14	Suction	24.6	14.3	17.4	8.5	8.2	26.	19.	6.7
	Blowing	40.1	36.	24.4	20.8	17.5	36.7	24.3	9.6
15	Suction	26.7	13.1	16.3	8.7	8.2	25.5	20.	12.
	Blowing	39.5	38.9	25.	21.4	18.3	32.	35.3	9.8

Table C.1: Influence coefficient matrices for suction and blowing from streamwise velocity distribution at level 1 in the presence of a nonlifting model at $M = 0.5$, $[\Delta V]/[\Delta P] = [(m/s)/psi]$.

Plenum Com. → / Control Points ↓		PL 2	PL3	PL4	PL5	PL6	PL7	PL8	PL9
1	Suction	20.1							
	Blowing	23.3							
2	Suction	23.1	5.1						
	Blowing	38.	9.9						
3	Suction	26.	7.						
	Blowing	52.8	18.						
4	Suction	28.2	11.3	3.1					
	Blowing	49.3	39.7	5.3					
5	Suction	27.	15.6	4.8					
	Blowing	45.7	55.	9.3					
6	Suction	26.4	14.7	11.3	1.				
	Blowing	42.4	52.	24.7	5.				
7	Suction	24.2	14.1	13.6	2.				
	Blowing	44.	45.7	28.2	8.				
8	Suction	26.9	13.	16.6	4.5				
	Blowing	42.4	37.5	26.2	22.2				
9	Suction	27.1	15.	17.8	7.4	2.4			
	Blowing	40.7	33.9	22.5	28.4	8.6			
10	Suction	28.4	14.8	19.	10.5	6.			
	Blowing	39.8	33.7	22.8	30.	15.			
11	Suction	26.2	16.9	16.7	14.8	13.6	11.3		
	Blowing	40.	36.5	21.1	26.4	29.	10.		
12	Suction	26.6	15.	15.2	13.5	11.6	20.	5.	
	Blowing	41.4	39.9	21.	22.2	26.7	22.8	12.3	
13	Suction	24.7	15.3	15.7	11.4	9.6	28.7	11.	
	Blowing	38.8	34.6	18.9	18.	18.2	36.4	19.	
14	Suction	24.5	15.2	17.4	9.8	8.2	27.	17.	6.0
	Blowing	37.1	32.	17.3	20.5	17.	36.5	21.5	9.6
15	Suction	25.7	13.1	19.	9.5	9.4	25.8	22.8	11.9
	Blowing	30.8	28.	18.6	21.8	18.4	27.	31.8	9.8

Table C.2: Influence coefficient matrices for suction and blowing from streamwise velocity distribution at level 2 in the presence of a nonlifting model at $M = 0.5$, $[\Delta V]/[\Delta P] = [(m/s)/psi]$.

Plenum Com. → / Control Points ↓		PL 2	PL3	PL4	PL5	PL6	PL7	PL8	PL9
1	Suction	15.7	2.0						
	Blowing	24.7	4.7						
2	Suction	19.2	4.3						
	Blowing	40.7	11.1						
3	Suction	21.2	8.						
	Blowing	44.4	24.						
4	Suction	22.2	11.6	4.7					
	Blowing	42.2	40.	7.9					
5	Suction	22.3	13.5	8.9					
	Blowing	41.1	47.5	21.					
6	Suction	22.4	14.1	13.6	3.				
	Blowing	40.1	45.	39.	8.8				
7	Suction	22.2	14.1	15.	4.4	1.8			
	Blowing	40.	43.	43.6	13.6	6.			
8	Suction	22.2	14.1	16.1	5.6	2.9			
	Blowing	40.	41.	45.	18.6	9.2			
9	Suction	22.2	14.	16.7	6.8	4.3			
	Blowing	40.	40.	43.7	22.	13.7			
10	Suction	22.2	14.	17.1	7.4	5.9	4.7		
	Blowing	40.	40.	42.	23.	19.5	6.8		
11	Suction	22.2	14.	16.9	7.9	7.7	9.9		
	Blowing	40.	40.	39.4	21.5	23.7	17.6		
12	Suction	22.2	14.	16.5	7.9	8.	14.9	5.2	
	Blowing	40.	40.	38.4	20.2	22.1	33.2	7.6	
13	Suction	21.4	14.	16.6	7.7	7.8	17.7	9.9	
	Blowing	39.5	40.	38.1	20.2	20.3	39.2	17.7	
14	Suction	21.4	14.	16.6	7.7	7.7	18.5	15.2	6.1
	Blowing	39.5	40.	38.	20.2	19.1	35.3	32.1	4.5
15	Suction	21.4	14.	16.4	7.6	7.7	18.4	18.4	11.6
	Blowing	39.5	40.	38.	20.2	19.1	32.7	38.8	11.1

Table C.3: Influence coefficient matrices for suction and blowing from sidewall pressure distribution at level 1 without a model at $M = 0.5$, $[\Delta V]/[\Delta P] = [(m/s)/psi]$.

Plenum Com. → / Control Points ↓		PL 2	PL3	PL4	PL5	PL6	PL7	PL8	PL9
1	Suction	15.7	2.0						
	Blowing	24.7	4.7						
2	Suction	20.1	3.8						
	Blowing	44.7	9.5						
3	Suction	21.2	8.						
	Blowing	46.8	24.						
4	Suction	22.2	12.4	3.7					
	Blowing	42.2	43.	6.2					
5	Suction	22.3	14.2	8.9					
	Blowing	40.6	51.	19.5					
6	Suction	22.4	14.5	14.6	2.7				
	Blowing	39.8	45.	44.	7.4				
7	Suction	22.2	14.3	16.0	4.4	1.3			
	Blowing	40.	43.	49.6	13.5	4.4			
8	Suction	22.2	14.2	16.9	6.2	2.5			
	Blowing	40.	41.	48.	21.3	8.			
9	Suction	22.2	14.1	17.2	7.3	4.3			
	Blowing	40.	40.	44.7	25.4	14.2			
10	Suction	22.2	13.9	17.1	7.9	6.3	4.		
	Blowing	40.	40.	41.7	24.6	21.5	4.3		
11	Suction	22.2	13.9	16.9	8.3	8.4	9.8		
	Blowing	40.	40.	39.4	21.8	25.9	16.2		
12	Suction	22.2	14.1	16.5	8.	8.3	16.	4.2	
	Blowing	40.	40.	38.4	20.2	22.1	38.6	5.6	
13	Suction	21.4	14.	16.6	7.7	7.8	18.6	9.8	
	Blowing	39.5	40.	38.1	20.2	20.3	42.7	16.9	
14	Suction	21.4	14.	16.6	7.7	7.7	18.6	16.1	4.6
	Blowing	39.5	40.	38.	20.2	19.1	35.3	35.2	2.7
15	Suction	21.4	14.	16.4	7.6	7.7	18.4	19.2	10.5
	Blowing	39.5	40.	38.	20.2	19.1	29.8	41.	8.4

Table C.4: Influence coefficient matrices for suction and blowing from side-wall presure velocity at level 2 without a model at $M = 0.5$, $[\Delta V]/[\Delta P] = [(m/s)/psi]$.

Plenum Com. → / Control Points ↓		PL 2	PL3	PL4	PL5	PL6	PL7	PL8	PL9
1	Suction	-5.57							
	Blowing	-10.24							
2	Suction	-3.52	-1.9						
	Blowing	-5.45	-7.31						
3	Suction		-2.79						
	Blowing		-7.77						
4	Suction		-2.12	-1.75					
	Blowing		-6.3	-5.22					
5	Suction			-2.81					
	Blowing			-7.63					
6	Suction			-4.86	-2.14				
	Blowing			-5.	-4.36				
7	Suction				-3.73	-2.37			
	Blowing				-5.16	-4.56			
8	Suction				-4.36	-3.51			
	Blowing				-4.68	-5.95			
9	Suction				-3.12	-4.5			
	Blowing				-3.28	-7.04			
10	Suction					-4.29	-4.26		
	Blowing					-6.35	-2.93		
11	Suction					-2.22	-7.47		
	Blowing					-2.61	-9.96		
12	Suction						-6.65	-3.68	
	Blowing						-5.12	-3.29	
13	Suction							-7.98	
	Blowing							-6.36	
14	Suction							-4.18	
	Blowing							-5.36	
15	Suction								-4.99
	Blowing								-5.26

Table C.5: Influence coefficient matrices for suction and blowing from normal velocity distribution at level 1 in the presence of a nonlifting model at $M = 0.5$, $[\Delta V]/[\Delta P] = [(m/s)/psi]$.

Plenum Com. → / Control Points ↓		PL 2	PL3	PL4	PL5	PL6	PL7	PL8	PL9
1	Suction	-6.46							
	Blowing	-15.79							
2	Suction	-5.38	-2.6						
	Blowing	-7.91	-11.09						
3	Suction		-5.03						
	Blowing		-14.31						
4	Suction		-3.25	-2.98					
	Blowing		-7.8	-9.76					
5	Suction			-6.23					
	Blowing			-12.1					
6	Suction			-5.14	-3.65				
	Blowing			-6.4	-7.95				
7	Suction				-5.17	-2.72			
	Blowing				-8.44	-6.26			
8	Suction				-4.02	-5.2			
	Blowing				-7.08	-11.05			
9	Suction				-3.27	-7.			
	Blowing				-3.54	-13.55			
10	Suction					-6.48	-7.16		
	Blowing					-11.51	-5.08		
11	Suction					-1.91	-12.06		
	Blowing					-1.71	-13.64		
12	Suction						-8.76	-5.68	
	Blowing						-7.68	-5.14	
13	Suction							-9.88	
	Blowing							-10.35	
14	Suction							-6.38	
	Blowing							-7.24	
15	Suction								-7.68
	Blowing								-6.30

Table C.6: Influence coefficient matrices for suction and blowing from normal velocity distribution at level 2 in the presence of a nonlifting model at $M = 0.5$, $[\Delta V]/[\Delta P] = [(m/s)/psi]$.

Bibliography

[1] Garner, H., Rogers, E., Acum, W., and Maskell, E., " Subsonic Wind Tunnel Wall Corrections, " AGARDograph 109, Oct. 1966.

[2] *AGARD Conference Proceedings*, " Wall Interference in Wind Tunnels, " AGARD-CP-335, Sep. 1982.

[3] Murman, E. M., " Computation of Wall Effects in Ventilated Transonic Wind Tunnels, ", AIAA Paper 72-1007, Sept. 1972, 10 pp.

[4] Murman, E. M., " A Correction Method for Transonic Wind Tunnel Wall Interference, " *AIAA 12th Fluid and Plasma Dynamics Conference*, AIAA Paper 79-1533, Williamsburg, Virginia, July 24-26, 1976.

[5] Goethert, B., *Transonic Wind Tunnel Testing*, Pergamon Press, 1961.

[6] Kemp, W. B., "Transonic Assessment of Two-Dimensional Wind Tunnel Wall Interference Using Measured Wall Pressures, Part II, " NASA CP-2045, 1979, pp. 473-486.

[7] Mokry, M., Chan, Y. Y. and Jones, D. J., " Two-Dimensional Wind Tunnel Wall Interference, " AGARD-AG-281, Nov. 1983.

[8] Vidal, R. J., Erickson, J. C. and Catlin, P. A., " Experiments with a Self-Correcting Wind Tunnel, " AGARD CP-174, No. 11, Oct. 1975, 13 pp.

[9] Satyanarayana B., Schairer, E. T. and Davis, S. S., " Adaptive-Wall Wind-Tunnel Development for Transonic Testing, " *Journal of Aircraft*, Vol.18, No.4, Apr. 1981, pp. 273-279.

[10] Kraft, E. M. and Parker, Jr., R. L. " Experiments for the Reduction of Wind Tunnel Wall Interference by Adaptive-Wall Technology, " AEDC-TR-79-51, Oct. 1979, 40 pp.

[11] Goodyear, M. J., " The Self Streamlining Wind Tunnel, " NASA TM X-72699, Aug. 1975.

[12] Tuttle, M. H. and Mineck, R. E. , " Adaptive Wall Wind Tunnels ; A Selected, Annotated Bibliography, " NASA TM 87639,1986.

[13] Lock, C. N., and Beavan, J. A., " Tunnel Interference at Compressibility Speeds Using the Flexible Walls of the Rectangular High-Speed Tunnel ," British ARC R&M No. 2005, Sept. 1944, 37 pp.

[14] Ferri, A. and Boronti, P., " A Method for Transonic Wind Tunnel Corrections, " *AIAA Journal*, Vol.11, Jan. 1973, pp.63-66.

[15] Sears, W. R., " Self Correcting Wind Tunnels, " *Aeronautical Journal*, Vol.78, Feb.- Mar. 1974, pp. 80-89.

[16] Erickson, J. C. and Nenni, J. P., " A Numerical Demonstration of the Establishment of Unconfined-Flow Conditions in a Self-Correcting Wind Tunnel, " CALSPAN-RK-5070-A-1, Nov. 1973, 38 pp.

[17] Erickson, J. C. and Homicz, G. F., " Numerical Simulations of a Segmented-Plenum Perforated, Adaptive-Wall Wind Tunnel, " *AIAA Journal*, Vol. 20, No. 5, May 1982, pp. 612-623.

[18] Sears, W. R., Vidal, R. J., Erickson Jr., J. C., and Ritter A., " Interference-Free Wind- Tunnel Flows by Adaptive Wall Technology, " *Journal of Aircraft*, Vol.14, No.11, Nov. 1977, pp. 1042-1050.

[19] Sears, W. R., "Adaptive Wind Tunnels with Imperfect Control," *Journal of Aircraft*, Vol. 16, May 1979, pp.344-348.

[20] Goodyear, M. J. and Wolf, S. W. D., " Development of a Self-Streamlining Flexible Walled Transonic Test Section, " *AIAA Journal*, Vol. 20, No. 2, Feb. 1982, pp. 227-234.

[21] Ganzer, U., " Advances in Adaptive-Wall Wind Tunnel Technique, " *An International Symposium on Recent Advances in Aeronautics and Aeroacoustics*, Stanford University, California, Aug. 22-26, 1983.

[22] Wolf, S. W. D., Cook, I. D. and Goodyear, M. J., " The Status of Two- and Three-Dimensional Testing in the University of Southampton Transonic Self-Streamlining Wind Tunnel, " AGARD-CP-335, No. 15, Sept. 1982.

[23] Chevallier, J.P., " Survey of the ONERA Activities on the Adaptive Wall Applications and Computation of Residual Corrections, " *Wind Tunnel Wall Interference Assessment/Correction Workshop*, NASA Langley Research Center, Jan. 25-26, 1983.

[24] Lo, C. F., and Kraft, E. M., " Convergence of the Adaptive-Wall Wind Tunnel," *AIAA Journal*, Vol. 16, No. 1, Jan. 1978, pp. 67-72.

[25] Dowell, E. H., " Control Laws for Adaptive Wind Tunnels, " *AIAA Journal*, Vol. 19, No. 11, Nov. 1981, pp. 1486-1488.

[26] Davis, S. S., " A Compatibility Assessment Method for Adaptive-Wall Wind Tunnels, " *AIAA Journal* , Vol. 19, No. 9, Sept. 1981, pp. 1169-1173.

[27] Schairer, E. T., and Mendoza, J. P., " Adaptive-Wall Tunnel Research at Ames Research Center, " AGARD-CP-335, No. 16, Sept. 1982.

[28] Erickson, J. C., " Application of the Adaptive-Wall Concept to Three-Dimensional Low Speed Wind Tunnels, " NASA CR-137, 1976.

[29] Schairer, E. T., " Experiments in a Three-Dimensional Adaptive-Wall Wind Tunnel, " NASA TP-2210, Sept. 1983.

[30] Ganzer, U., " On the Use of Adaptive Walls for Transonic Wind Tunnel, " AGARD-CP-335, No. 13, Sept. 1982 Aug. 22-26, 1983.

[31] Parker, R. L. and Erickson, J. C., " Status of 3-D Adaptive Wall Test Section Development at AEDC, " AIAA Paper 84-0624, 10 pp.

[32] Sears, W. R., " Adaptable Wind Tunnel for Testing V/STOL Configurations at High Lift, " *Journal of Aircraft*, Vol. 20, No. 11, Nov. 1983, pp. 968-974.

[33] Lee, D. C. L. and Sears W. R., " Experiments with an Adaptable-Wall Wind Tunnel for Large Lift, " *Journal of Aircraft*, Vol. 24, No. 6, Jun. 1987, pp. 371-376.

[34] Bodapati S. and Çelik, Z. Z., " Optimization Studies for the Development of Adaptive Wall Wind Tunnel, " *Proceeding of International Congress on Instrumentation in Aerospace Simulation Facilities* , Stanford University, Aug. 26-28, 1985.

[35] Çelik, Z. Z. and Bodapati, S., " Evaluation of Influence Coefficient Matrices for an Adaptive-Wall Wind Tunnel and Applications to One-Step Convergence Scheme, " *AIAA 19th Fluid Dynamics, Plasma Dynamics and Lasers Conference*, AIAA Paper 87-1433, Honolulu, Hawaii, June 8-10,1987.

[36] Çelik, Z. Z. and Bodapati, S., " Investigation of the Various Convergence Schemes for the Development of an Adaptive-Wall Wind Tunnel, " *AIAA 5th Applied Aerodynamics Conference*, AIAA Paper 87-2609, Monterey, California, Aug. 17-19, 1987.

[37] Davis, S. S., " The Evolution of Adaptive-Wall Wind Tunnels, " NASA TM 84404, Sept. 1983, 33 pp.

[38] Lawson, C. L. and Hanson, R. J., *Solving Least Squares Problems*, Prentice-Hall, Englewood Cliffs, New Jersey, 1974.

[39] Spiegel, M. R., *Complex Variables*, Schaum's Outline Series in Mathematics, McGraw-Hill Book Company, 1964.

[40] Everhart, J. L., " A Method for Modifying Two-Dimensional Adaptive Wind-Tunnel Walls Including Analytical and Experimental Verification, " NASA TP-2081, Feb. 1983.

[41] Reinsch, C. H., " Smoothing by Spline Functions, " Numerische Mathematik, Vol 10, No. 3,1967, pp. 177-183.

[42] Durst, F., *Principles and Practices of Laser-Doppler Anemometry*, 2nd Edition, Academic Press, 1981.

[43] *Owners Manual: Laser Velocimeter-Series 2000 Electronic Processor*, Macro-Dyne Inc., Sept. 1976.

[44] Seegmiller, H. L. and et. al. , " Development of a New Laser Doppler Velocimeter for the Ames High Reynolds Channel No. II, " NASA TM 86772, July 1985.

[45] Vidal, R. J., Catlin, P. A. and Chudyk, D. W., " Two-Dimensional Subsonic Experiments with an NACA 0012 Airfoil, " Calspan Report, No. RK-5070-A-3, Dec. 1973.

[46] *AGARD Advisory Report*, " Experimental Data Base for Computer Program Assessment, " AGARD-AR-138, May 1979.

[47] Dougherty, F. C., Holst, T. L., Gundy, K. L. and Thomas, S. D.," TAIR - a Transonic Airfoil Analysis Code, " NASA TM 81296, May 1981.

[48] Lock, R. C., " Test Cases for Numerical Methods in Two-Dimensional Transonic Flows, " AGARD Report No. 575, Nov. 1970.

[49] Harris, C. D., " Two-Dimensional Aerodynamic Characteristics of the NACA 0012 Airfoil in the Langley 8-Foot Transonic Pressure Tunnel, " NASA TM 81927, April 1981.

[50] McCroskey, W. J., " A Critical Assessment of Wind Tunnel Results for the NACA 0012 Airfoil, " AGARD Fluid Dynamics Panel Symposium on Aerodynamic Data Accuracy and Quality: Requirements and Capabilities in Wind Tunnel Testing," Naples, Italy, Sept. 28-Oct. 2, 1987.

[51] Unpublished data from NASA Langley 0.3 m. Cryogenic Transonic Adaptive-Wall Wind Tunnel, 1987.